IMPLEMENTATION AND COMPARISON OF RECONSTRUCTION ALGORITHMS FOR MAGNETIC RESONANCE – ELECTRIC IMPEDANCE TOMOGRAPHY (MR-EIT)

A THESIS SUBMITTED TO
THE GRADUATE SCHOOL OF NATURAL AND APPLIED SCIENCES
OF
MIDDLE EAST TECHNICAL UNIVERSITY

BY

DARÍO MARTÍN LORCA

IN PARTIAL FULFILLMENT OF THE REQUIREMENTS
FOR
THE DEGREE OF MASTER OF SCIENCE
IN
ELECTRICAL AND ELECTRONICS ENGINEERING

FEBRUARY 2007

Approval of the Graduate School of Natural and Applied Sciences.

____
Prof. Dr. Canan ÖZGEN
Director

I certify that this thesis satisfies all the requirements as a thesis of the degree of Master of Science.

____
Prof. Dr. Ismet ERKMEN
Head of Department

This is to certify that we have read this thesis and that in our opinion it is fully adequate, in scope and quality, as a thesis for the degree of Master of Science.

____
Prof. Dr. B. Murat EYÜBOGLU
Supervisor

Examining Committee Members

Prof. Dr. Nevzat Güneri GENÇER (METU, EEE) ____________

Prof. Dr. Murat EYÜBOGLU (METU, EEE) ____________

Prof. Dr. Adnan KÖKSAL (Hacettepe Üniv., EEE) ____________

Assoc. Prof. Dr. Tolga ÇILOGLU (METU, EEE) ____________

Assist. Prof. Dr. Yesim SERINAGAOGLU (METU, EEE) ____________

I hereby declare that all information in this document has been obtained and presented in accordance with academic rules and ethical conduct. I also declare that, as required by these rules and conduct, I have fully cited and referenced all material and results that are not original to this work.

Name, Last name: Darío MARTÍN LORCA

Signature:

ABSTRACT

IMPLEMENTATION AND COMPARISON OF RECONSTRUCTION ALGORITHMS FOR MAGNETIC RESONANCE – ELECTRIC IMPEDANCE TOMOGRAPHY (MR-EIT)

Martín Lorca, Darío

MSc., Department of Electrical and Electronics Engineering

Supervisor: Prof. Dr. B. Murat Eyüboglu

February 2007, 122 pages

In magnetic resonance electrical impedance tomography (MR-EIT), cross-sectional images of a conductivity distribution are reconstructed. When current is injected to a conductor, it generates a magnetic field, which can be measured by a magnetic resonance imaging (MRI) scanner. MR-EIT reconstruction algorithms can be grouped into two: current density based reconstruction algorithms (*Type*-I) and magnetic flux density based reconstruction algorithms (*Type*-II). The aim of this study is to implement a series of reconstruction algorithms for MR-EIT, proposed by several research groups, and compare their performance under the same circumstances. Five direct and one iterative *Type*-I algorithms, and an iterative *Type*-II algorithm are investigated. Reconstruction errors and spatial resolution are quantified and compared. Noise levels corresponding to system SNR 60, 30 and 20 are considered. Iterative algorithms provide the lowest errors for the noise-free case. For the noisy cases, the iterative *Type*-I algorithm yields a lower error than the *Type*-II, although it can diverge for

SNR lower than 20. Both of them suffer significant blurring effects, especially at SNR 20. Another two algorithms make use of integration in the reconstruction, producing intermediate errors, but with high blurring effects. Equipotential lines are calculated for two reconstruction algorithms. These lines may not be found accurately when SNR is lower than 20. Another disadvantage is that some pixels may not be covered and, therefore, cannot be reconstructed. Finally, the algorithm involving the solution of a linear system provides the less blurred images with intermediate error values. It is also very robust against noise.

Keywords: electrical impedance tomography, magnetic resonance imaging, current density imaging

ÖZ

MANYETIK REZONANS – ELEKTRIKSEL EMPEDANS TOMOGRAFISI IÇIN GERIÇATIM ALGORITMALARININ GERÇEKLENMESI VE KARSILASTIRILMASI

Martín Lorca, Darío

Yüksek Lisans, Elektrik ve Elektronik Mühendisligi Bölümü

Tez Yöneticisi: Prof. Dr. B. Murat Eyüboglu

Subat 2007, 122 sayfa

Manyetik rezonans elektrik empedans tomografisinde (MR-EIT), bir iletkenlik dagiliminin kesit görüntüleri olusturulmaktadir. Bir iletkene akim uygulandiginda, manyetik rezonans görüntüleme (MRI) tarayicisiyla ölçülebilen bir manyetik alan olusmaktadir. MR-EIT geri çatim algoritmalari iki grupta toplanmaktadir: akim yogunlugu temelli geri çatim algoritmalari (Tip 1) ve manyetik aki yogunlugu temelli geri çatim algoritmalari (Tip 2). Bu çalismanin amaci, birçok arastirma grubu tarafindan önerilmis olan bir dizi MR-EIT geri çatim algoritmasini gerçeklemek ve ayni sartlar altinda performanslarini karsilastirmaktir. Bu çalismada, bes direkt ve bir iteratif Tip 1 algoritma ve bir iteratif Tip 2 algoritma incelenmistir. Geri çatim hatalari, uzamsal çözünürlük gürültü performaslari incelenmis ve karsilastirilmistir. Gürültü analizinde sistem sinyal-gürültü orani (SNR) 60, 30 ve 20'ye karsilik gelen gürültü seviyeleri göz önüne alinmistir. Gerçeklenen algoritmalar içinde iteratif algoritmalar, gürültüsüz durumlar için en düsük hatayi vermistir. Gürültülü durumlar için, iteratif Tip 1 algoritma, SNR’in 20’den düsük degerleri için iraksayabilmesine ragmen, Tip 2’den daha düsük hata vermektedir. Her iki iteratif algoritmada da, özellikle SNR 20’de elde edilen görüntülerde kayda deger bir bulaniklik olusmaktadir. Geri çatimda integral almayi kullanan iki Tip 1 algoritma, digerleri ile karsilastirildiginda yüksek bulanikliga ragmen orta seviyede hatalar vermektedirler. Es potansiyel çizgileri kullanan iki geriçatim algoritmasinda, çizgiler SNR 20’den düsük oldugu durumlarda dogru olarak bulunamamaktadir. Bu iki algoritmanin bir baska dezavantaji da bazi piksellerin kapsanamamasi ve dolayisiyla iletkenliklerinin hesaplanamamasidir. Son olarak, bir lineer sistemin çözümünü içeren geriçatim algoritmasi, digerlerine göre daha düsük hatali ve daha az bulanik görüntüler vermistir. Ayrica bu yöntemin gürültüye karsi da dirençli oldugu görülmüstür.

Anahtar Kelimeler: elektriksel empedans görüntüleme, manyetik rezonans görüntüleme, akim yogunlugu görüntüleme

ACKNOWLEDGEMENTS

Firstly, I would like to thank my family for having given me this great opportunity. This adventure has brought the biggest and most important changes to my life. I sincerely thank you for all your support, understanding, patience and love.

I would also like to express my gratitude to my supervisor Prof. Dr. Murat Eyüboglu for his guidance throughout the study.

Thanks to all my Spanish students: Ayhan, Deniz, Suat, Murat, Yunus, Aziz, Orhan, Ilgin, and many, many more! I hope you enjoyed as much as me. Thanks for letting me feel comfortable and useful. For sure, one part of this is because of you.

I would also like to thank all my lab mates and around: Ayhan, Hüseyin, Emre, Evren, Sedat, Doga, for your long chats, advice, guidance and support. Take much care of METU. Keep it so unique.

I would like to thank very much my true friends Jose and Jorge for always listening and, very especially, for having traveled so far for such special moments… and survived it!

Finally, I gratefully acknowledge the support, comfort and caring of my new family, Mine. Thank you for bringing me here and help me overcome this. And a last small mention to small Ates.

TABLE OF CONTENTS

LIST OF TABLES

LIST OF FIGURES

CHAPTER 1

INTRODUCTION

The electrical resistivity of biological tissues differs among various tissue types and also with its physiological and pathological state [4]. Therefore, the knowledge of the *in vivo* resistivity distribution of a body would yield diagnostically valuable information about anatomy, physiological processes and pathology. Some resistivity values are given in Table 1.1.

Electrical impedance tomography (EIT) is a non-invasive medical imaging modality that reconstructs electrical conductivity distribution inside a conductor volume [4]. It was proposed in 1978 by Henderson and Webster [14], but the first practical realization of a medical EIT was due to Barber and Brown [1]. EIT is technically based on generating a current distribution inside the body, either by injecting currents with surface electrodes (injected-EIT) [26], or inducing these currents by coils placed around the body (induced-EIT) [11], [12]. Simultaneously to these injections, electrical or magnetic measurements that reflect the internal conductivity distribution are measured [4]. Typically, peripheral voltage measurements are acquired via electrodes attached to the surface of the conductor object. The process is repeated for several different configurations of applied current. From these measurements, the conductivity distribution can be extracted by suitable reconstruction algorithms. For both approaches to generate the currents inside the subject, the sensitivity of peripheral voltage measurements to conductivity perturbations is position-dependent and degrades as the distance to the surface increases [18], [7], being very poor for the most inner regions. The spatial resolution of the conductivity image is related to conductivity accuracy, noise, contrast and number of electrodes (or independent measurements) used in the EIT system [29]. Then, since the sensitivity is small to inner regions, reconstructed conductivity images yield low and space dependent spatial resolution. In static EIT imaging, usually thirty two or more electrodes are used to achieve 5% spatial resolution at most [20].

Table 1.1: Resistivity typical values for different biological tissues.

Tissue	Resistivity $(\Omega\cdot\text{cm})$	Species
Blood[1]	150	Human
Plasma[1]	50-60	Mammal
Cerebrospinal fluid[1]	65	Human
Bile[1]	60	Cow, pig
Urine[1]	30	Cow, pig
Cardiac muscle[1]	400	Dog
Lungs[1]	1500	Mammal
Lungs[2]	122 – 202	Human
Kidney[1]	370	Mammal
Liver[2]	296 – 396	Human
Heart[2]	133 – 231	Human
Brain[1]	580	Mammal
Fat[1]	2500	Mammal
Bone[1]	15000	Mammal
Bone[2]	$91 \times 10^6 - 169 \times 10^6$	Human
Sodium Chloride[1]	14.9	-

A solution for the position dependency problem of EIT is using data directly obtained from inside the subject. But, since there is no non-invasive technique to make voltage measurements inside an object, another approach is necessary. By using conventional *Magnetic Resonance Imaging* (MRI), together with appropriate phase encoding sequences, it is possible to measure the magnetic flux density distribution throughout the imaging region. This idea was firstly proposed for determining the field inhomogeneity in an MRI system [21]. In

[1] Reproduced from [32].

[2] Resistivity 95% confidence interval for the tissue. Reproduced from [9].

early 90s, a new imaging modality which reconstructs current density images due to injected currents, using magnetic flux density measurements, was proposed by Scott *et al* [27]. This technique is called *Magnetic Resonance – Current Density Imaging* (MR-CDI), or shortly, *Current Density Imaging* (CDI). These measurements, carried out with MRI scanners, can be made with very high spatial sampling and high sensitivity to the inner conductivity perturbations.

In 1992, Zhang [35] proposed the use of electrical current density distribution, measured using MR-CDI, together with conventional EIT voltage measurements to obtain the conductivity distribution inside an object. This technique is named as *Magnetic Resonance – Electrical Impedance Tomography* (MR-EIT). By knowing this magnetic flux density and current density distribution, both the spatial resolution and accuracy of the reconstructed resistivity images using conventional EIT are improved. The inner current density distribution is also dependent on the size, shape and position of the surface electrodes, besides their own conductivity properties. In MR-EIT, current injection needs at least four surface electrodes, which is much less than the number of electrodes needed in EIT. Also, the boundary shape of the subject is easily known, through the MR images. This eliminates the problem related with modeling error. In this study, two oppositely placed electrodes are used as an electrode set. Each different electrode set and the amount of applied current is called a *current injection profile*.

Summarizing, when a current is injected into a subject via surface electrodes, it creates a voltage and a current density distribution $\vec{J}$. The injection current on lead wires and $\vec{J}$ inside the subject generate a magnetic flux density distribution $\vec{B}$, which is measured by MR-CDI technique using a MRI system. Afterwards, it is possible to compute $\vec{J}$ from $\vec{J} = \nabla \times \vec{B} / m_0$. Then, MR-EIT reconstruction algorithms utilize either $\vec{J}$ or $\vec{B}$, in addition to measured boundary voltages, to obtain high resolution cross-sectional conductivity (or resistivity) images of a subject.

1.1 Objectives of the Thesis

Several MR-EIT reconstruction algorithms have been proposed by different research groups since 1992. These algorithms use different conductivity models, injected current, electrode configuration, noise models and levels, etc, making very difficult to compare them and see the advantages and disadvantages of each method. The objectives of this thesis are:

- To classify some of the recent reconstruction algorithms, depending if they use as input data current density or magnetic flux density distribution.
- To implement some current density based algorithms proposed previously by other studies.
- To develop and implement a novel current density based reconstruction algorithm.
- To implement a magnetic flux density based algorithm, suggested previously by other researchers.
- To define a common conductivity model and a set of conditions in order to compare them objectively.

Three of the current density based algorithms which have been studied were proposed by Ider *et al* in 2003 [15]. Another one, called J-substitution algorithm was published by Kwon *et al* in 2002 [20]. Finally, the equipotential – projection reconstruction algorithm, proposed in 1999 by Eyüboglu US patent [8] and applied to real data by Özdemir [25], has been extended for the case where no voltage measurements are needed in order to get a relative conductivity distribution. As a magnetic flux density based reconstruction method, the harmonic B_z algorithm, proposed by Oh *et al* [22] in 2003 has been studied.

1.2 Organization of the Thesis

In Chapter 2, the forward and inverse problems in MR-EIT are defined and formulated. The extraction of the induced magnetic flux density from MRI images is also explained. Besides, a classification of several reconstructed algorithms is given. In Chapter 2, five previously proposed reconstruction algorithms, based on current density, are explained. In Chapter 4, one magnetic flux density based reconstruction algorithm is explained. In Chapter 5, two conductivity models are introduced. One is simulated data, while the other is experimental data, collected by the 0.15T METU-EE MRI system by previous researchers [2], [24]. Then, the reconstruction of both models is performed by using all of the studied algorithms, and a comparison is carried out. The thesis concludes with Chapter 6, where a summary is given, final conclusions are drawn and future work is proposed.

CHAPTER 2

THEORY

2.1 Introduction

In this chapter, firstly, the forward problem in MR-EIT is formulated. The governing differential equation is a Poisson's relation with Neumann boundary conditions. Analytical solution to this problem does not exist for complex conductivity distributions. Then, numerical methods must be used instead. The finite element method (FEM) and Cell-Centered Finite Difference Method (CCFD) are utilized. Once the potential distribution is known, the magnetic field density distribution can be calculated by Biot-Savart law. But, in practice, the magnetic flux density distribution induced by injected currents is the only thing that can be measured using a MRI system. The procedure to extract the magnetic flux density is explained later in this section. Finally, the inverse problem is defined and formulated and a classification of reconstruction algorithms is given.

2.2 The Forward Problem of MR-EIT

2.2.1 Definition

In MR-EIT, current is injected to the object with surface electrodes. This current is distributed inside, as a function of the inner conductivity distribution. If a non-alternating current flows on a conductive media, then static potential and magnetic flux density distributions appear. In the current MR systems, the only measurable field quantity inside the object is the magnetic flux density. From there, the conductivity distribution can be reached and calculated. But firstly, it is necessary to understand and formulate what is happening inside the object when a current is injected.

The *forward problem* in MR-EIT imaging is defined as the calculation of peripheral potential values and magnetic flux density distribution for a known inner conductivity distribution, and given boundary conditions [1].

The forward problem can be used for the generation of the simulated data and the formulation of the inverse problem. It can be also used in iterative reconstruction algorithms. There, the procedure starts with an initial conductivity guess, solves the forward problem and calculates the error between the computed and measured field quantities. In each iteration, the conductivity values are updated in some way, and the forward problem is solved again, until the calculated error is smaller than a given tolerance value.

2.2.2 Formulation

The injection of a current *I* into an isotropic nonmagnetic and conductive object, occupying a volume Ω with a boundary $\partial\Omega$, generates a current density distribution inside the object, related to the conductivity distribution s in its interior. This current injection is applied by surface electrodes attached to the boundary $\partial\Omega$ during a finite time, short enough to assume that the conductivity distribution is time independent during the pulses [23]. See Figure 2.1.

The nonlinear relation between conductivity s and potential distribution f is given by the boundary value problem (*BVP*) defined by Poisson's relation as:

$$\nabla\cdot\left(s\nabla f\right)=0 \qquad \text{in}\,\Omega. \tag{2.1}$$

The electrical current on the boundary of the imaging region is specified for MR-EIT problem by imposing the following Neumann boundary condition:

$$-s\,\frac{\partial f}{\partial \hat{n}}=\begin{cases} J & \text{on positive current electrode} \\ -J & \text{on negative current electrode} \\ 0 & \text{elsewhere,} \end{cases} \tag{2.2}$$

where $\hat{n}$ denotes the unit outward normal vector at the boundary $\partial\Omega$, and J is the current density at $\partial\Omega$.

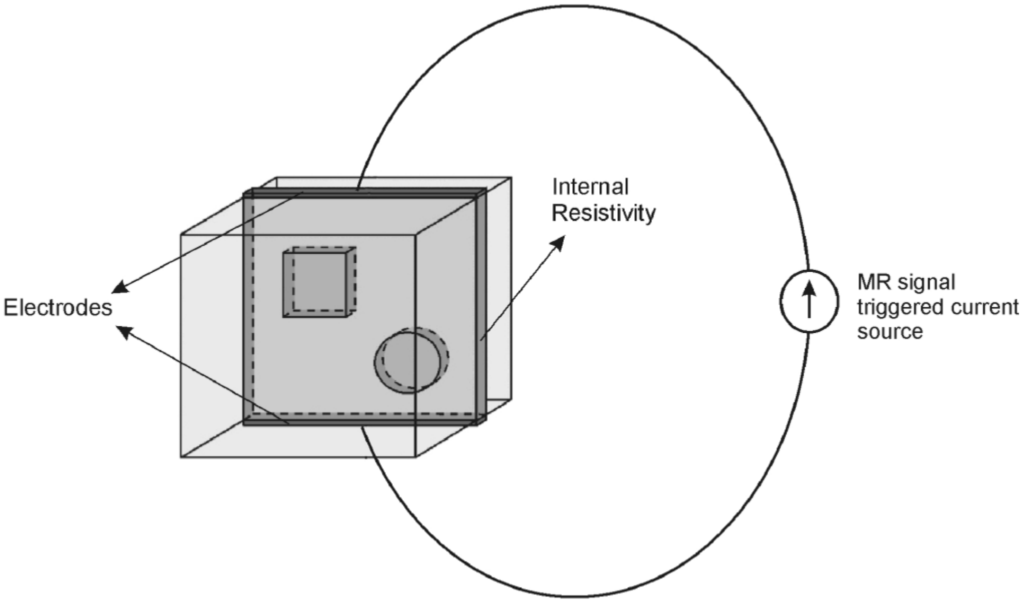

Figure 2.1: A cubical object Ω with a two-dimensional internal resistivity distribution r is placed in a MRI system. In order to image that internal resistivity, the current is injected through two surface electrodes.

Once the potential field distribution is found, the electrical field distribution can be calculated as:

$$\vec{E} = -\nabla f \, . \tag{2.3}$$

Then, the corresponding current density distribution is obtained with Ohm's relationship:

$$\vec{J} = s\,\vec{E} \, . \tag{2.4}$$

The magnetic flux density generated by this current density distribution is given by Biot-Savart law:

$$\vec{B} = \frac{m_0}{4p} \int \frac{\vec{J} \times \hat{a}_R}{R^2} dv , \tag{2.5}$$

where m_0 is the permeability of the free space, R is the distance between the source (x',y',z') and field (x,y,z) points, $\hat{a}_R$ is the unit vector from the source point to the field points, and dv is the differential unit of volume. The source points are elements of the imaging slice Ω_S, but the field points can be off-slice.

Finite element method (FEM) or finite difference method are commonly used to solve the forward problem given in (2.1) and (2.2).

2.2.3 Cell-Centered Finite Difference Method Implementation

Cell-Centered finite differences (CCFD) is one of the most popular methods for numerical solutions of second-order elliptic boundary value problems [19]. In this thesis, it is used to solve the forward problem in iterative algorithms.

Firstly, let the square target imaging region $\Omega_S :(-L,L)\times(-L,L)$ be uniformly divided into $N\times N$ sub squares Ω_{i+jN}, containing the resistivity values of the image at their center point (x_i, y_j), where $i=0,\ldots,N-1$ and $j=0,\ldots,N-1$.

The voltage at the center point (x_i, y_j) of every cell Ω_{i+jN} can be approximated by:

$$v_{i+jN} := V_r\left(x_i, y_j\right). \tag{2.6}$$

In this cell-centered finite difference method, the resistivity r is assumed to be constant on each sub square Ω_k, denoted by r_k, where $k=1,\ldots,N^2$. There are three types of sub squares: interior cells, boundary cells and corner cells, which will correspond with nine different cases (Figure 2.2(b)) in the implementation of the algorithm.

Firstly, one fixed element Ω_k which lies in the interior of Ω will be studied and its expression derived. Later, the resulting equations for the rest are directly given.

Then, considering an inner element Ω_k, where

$$k = i + jN + 1 \quad \text{for} \quad 1 \le i, \quad j \le N - 2 .$$

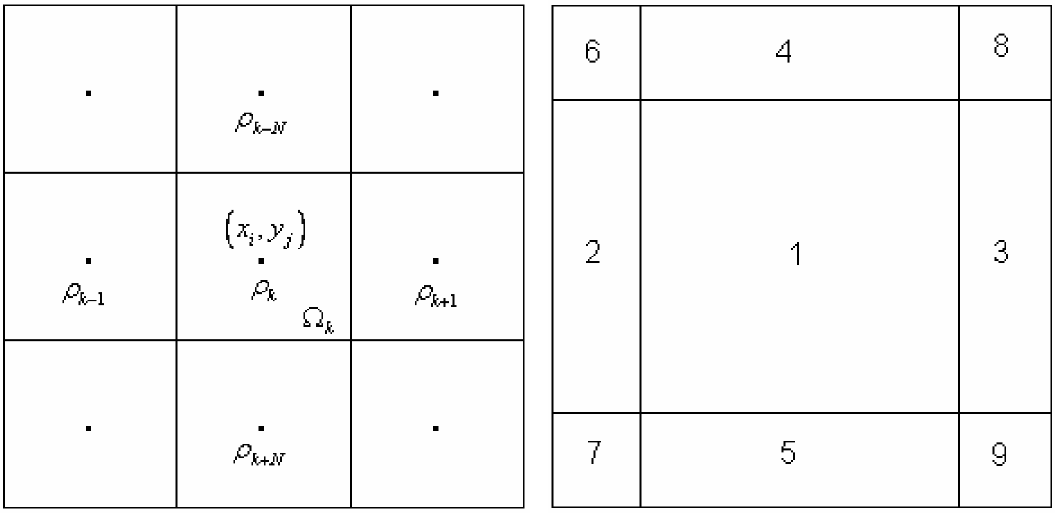

(a) (b)

Figure 2.2: Cell-Centered Finite Difference Method. (a) Resistivity r_k at every element Ω_k and surrounding elements. (b) In the implementation, nine different types of elements are considered.

Since $\nabla \cdot \left((1/r_k) \nabla V_r \right) = 0$ yields on each element, integrating by parts, the following results:

$$0 = \frac{1}{r_k} \int_{\Omega_k} \nabla \cdot \left(\nabla V_r \right) d\vec{r} = \frac{1}{r_k} \int_{\partial \Omega_k} \frac{\partial V_r}{\partial n} ds . \tag{2.7}$$

On the other hand, using the simplest quadrature rule, the following approximation can be obtained:

$$\begin{aligned} \frac{1}{r_k} \int_{\partial \Omega_k} \frac{\partial V_r}{\partial n} ds \approx \frac{h}{r_k} \Bigg[& \partial_x V_r \left(\frac{x_i + x_{i+1}}{2}, y_j \right) - \partial_x V_r \left(\frac{x_i + x_{i-1}}{2}, y_j \right) \\ & + \partial_y V_r \left(x_i, \frac{y_j + y_{j+1}}{2} \right) - \partial_y V_r \left(x_i, \frac{y_j + y_{j-1}}{2} \right) \Bigg], \end{aligned} \tag{2.8}$$

where h denotes the side length of each subsquare Ω_k.

The four terms in (2.8) are the values of the normal derivative of V_r at the midpoints of the four sides of the element Ω_k. Since all of them can be calculated similarly, only the expression for the third term is derived. The interface condition between two adjacent elements Ω_k and Ω_{k+N} can be approximated as:

$$\frac{V_r\left(x_i,\dfrac{y_j+y_{j+1}}{2}\right)-v_k}{r_k} \approx \frac{v_{k-N}-V_r\left(x_i,\dfrac{y_j+y_{j+1}}{2}\right)}{r_{k+N}}, \tag{2.9}$$

which produces:

$$V_r\left(x_i,\frac{y_j+y_{j+1}}{2}\right)=\frac{s_{k+N}v_{k+N}+s_k v_k}{s_{k+N}+s_k}. \tag{2.10}$$

Defining

$$a_{k,k\pm N}=\frac{s_k s_{k\pm N}}{s_k+s_{k\pm N}} \quad \text{and} \quad a_{k,k\pm 1}=\frac{s_k s_{k\pm 1}}{s_k+s_{k\pm 1}}, \tag{2.11}$$

then, the third term in (2.8) can be approximated as

$$hs_k\partial_y V_r\left(x_i,\frac{y_j+y_{j+1}}{2}\right)\approx 2a_{k,k+N}\left(v_{k+N}-v_k\right). \tag{2.12}$$

Similar procedures for the other three terms in (2.8), produces the expression of the inner points of Ω:

$$\begin{aligned} 0 &= a_{k,k+N}v_{k,k+N}+a_{k,k-N}v_{k,k-N} \\ &\quad +a_{k,k+1}v_{k,k+1}+a_{k,k-1}v_{k,k-1}-a_{k,k}v_k, \end{aligned} \tag{2.13}$$

where,

$$a_{k,k}=\left\{a_{k,k+N}+a_{k,k-N}+a_{k,k+1}+a_{k,k-1}\right\}. \tag{2.14}$$

Similarly, the expression for the elements Ω_k on the left boundary $\partial\Omega$, that is,

$$k = i + jN + 1 \quad \text{for} \quad i = 0 \text{ and } 1 \leq j \leq N - 2,$$

can be obtained as explained above, resulting:

$$\begin{aligned} I(-L, y_k) = {} & a_{k,k+N} v_{k,k+N} + a_{k,k-N} v_{k,k-N} \\ & + a_{k,k+1} v_{k,k+1} - a_{k,k} y_k, \end{aligned} \tag{2.15}$$

where,

$$a_{k,k} = \{ a_{k,k+N} + a_{k,k-N} + a_{k,k+1} \} \tag{2.16}$$

and

$$I(-L, y_k) = \int_{\partial\Omega_k \cap \partial\Omega} j_{I^q} \, ds. \tag{2.17}$$

The expression for the elements Ω_k on the right boundary $\partial\Omega$, that is,

$$k = i + jN + 1 \quad \text{for} \quad i = N - 1 \text{ and } 1 \leq j \leq N - 2,$$

results:

$$\begin{aligned} I(L, y_k) = {} & a_{k,k+N} v_{k,k+N} + a_{k,k-N} v_{k,k-N} \\ & + a_{k,k-1} v_{k,k-1} - a_{k,k} v_k, \end{aligned} \tag{2.18}$$

where,

$$a_{k,k} = \{ a_{k,k+N} + a_{k,k-N} + a_{k,k-1} \} \tag{2.19}$$

and

$$I(L, y_k) = \int_{\partial\Omega_k \cap \partial\Omega} j_{I^q} \, ds. \tag{2.20}$$

The expression for the elements Ω_k on the upper boundary $\partial\Omega$, i.e. ,

$$k = i + jN + 1 \quad \text{for} \quad 1 \leq i \leq N - 2 \text{ and } j = 0,$$

results:

$$\begin{aligned} I(x_k, L) = {} & a_{k,k+1} v_{k,k+1} + a_{k,k-1} v_{k,k-1} \\ & + a_{k,k+N} v_{k,k+N} - a_{k,k} v_k, \end{aligned} \tag{2.21}$$

where,

$$a_{k,k} = \left\{ a_{k,k+1} + a_{k,k-1} + a_{k,\, k+N} \right\} \tag{2.22}$$

and

$$I\left(x_k, L\right) = \int_{\partial\Omega_k \cap \partial\Omega} j_{I^q} ds\,. \tag{2.23}$$

The expression for the elements Ω_k on the lower boundary $\partial\Omega$,

$$k = i + jN + 1 \quad \text{for} \quad 1 \le i \le N-2 \text{ and } j = N-1,$$

results:

$$\begin{aligned} I\left(x_k, -L\right) = a_{k,k+1}v_{k,k+1} + a_{k,k-1}v_{k,k-1} \\ +a_{k,\, k-N}v_{k,k-N} - a_{k,\, k}v_k, \end{aligned} \tag{2.24}$$

where,

$$a_{k,k} = \left\{ a_{k,k+1} + a_{k,k-1} + a_{k,\, k-N} \right\} \tag{2.25}$$

and

$$I\left(x_k, -L\right) = \int_{\partial\Omega_k \cap \partial\Omega} j_{I^q} ds\,. \tag{2.26}$$

Finally, similar arguments can be used to obtain the expressions for the four corner elements Ω_k,

$$k = i + jN + 1 \quad \text{for} \quad i, j = 0 \text{ or } N-1.$$

The expression for the left upper corner element, where $k = 1$, comes to be:

$$I\left(-L, y_1\right) + I\left(x_1, L\right) = a_{k,\, k+N}v_{k,\, k+N} + a_{k,k+1}v_{k,k+1} - a_{k,k}v_k, \tag{2.27}$$

where,

$$a_{k,k} = \left\{ a_{k,\, k+N} + a_{k,k+1} \right\} \tag{2.28}$$

and

$$I\left(-L, y_1\right) + I\left(x_1, L\right) = \int_{\partial\Omega_k \cap \partial\Omega} j_{I^q} ds \, . \tag{2.29}$$

Considering the left lower corner element, with $k = N(N-1)+1$, it results:

$$I\left(-L, y_{N(N-1)+1}\right) + I\left(x_{N(N-1)+1}, -L\right) = a_{k,\, k-N} v_{k\,, k-N} + a_{k\,,k+1} v_{k,k+1} - a_{k,\, k} v_k \, , \tag{2.30}$$

where,

$$a_{k\,,k} = \left\{ a_{k,\, k-N} + a_{k\,,k+1} \right\} \tag{2.31}$$

and

$$I\left(-L, y_{N(N-1)+1}\right) + I\left(x_{N(N-1)+1}, -L\right) = \int_{\partial\Omega_k \cap \partial\Omega} j_{I^q} ds \, . \tag{2.32}$$

The expression for the right upper corner element, where $k = N$, comes to be:

$$I\left(-L, y_N\right) + I\left(x_N, L\right) = a_{k,\, k+N} v_{k\,, k+N} + a_{k,k+1} v_{k,k+1} - a_{k,k} v_k \, , \tag{2.33}$$

where,

$$a_{k\,,k} = \left\{ a_{k,\, k+N} + a_{k\,,k+1} \right\} \tag{2.34}$$

and

$$I\left(-L, y_N\right) + I\left(x_N, L\right) = \int_{\partial\Omega_k \cap \partial\Omega} j_{I^q} ds \, . \tag{2.35}$$

Considering the right lower corner element, where $k = N^2$, it results:

$$I\left(-L, y_{N^2}\right) + I\left(x_{N^2}, -L\right) = a_{k,\, k-N} v_{k\,, k-N} + a_{k\,,k-1} v_{k,k-1} - a_{k,\, k} v_k \, , \tag{2.36}$$

where,

$$a_{k\,,k} = \left\{ a_{k,\, k-N} + a_{k\,,k-1} \right\} \tag{2.37}$$

and

$$I\left(-L, y_{N^2}\right) + I\left(x_{N^2}, -L\right) = \int_{\partial\Omega_k \cap \partial\Omega} j_{I^q} ds \, . \tag{2.38}$$

Now, with the set of equations from (2.13) to (2.36), it is possible to build a linear equation system as follows:

$$A\mathbf{x} = \mathbf{b}, \tag{2.39}$$

where A is a $N^2 \times N^2$ matrix, $\mathbf{x}$ is a vector containing the unknown voltages at the center of every Ω_k element $\mathbf{x} = \left(v_1, v_2, \ldots, v_{N^2}\right)$, and $\mathbf{b}$ is the injection current vector associated with I^q.

However, this A matrix is very ill-conditioned, with condition number 10^{16} and rank $N^2 - 1$. Then, the linear system (2.39) has been solved by using the preconjugate gradient method. This iterative solving method produces a sequence of iteration vectors $x^{(k)}, k = 1,2,\ldots$, that converge to the desired solution, provided a tolerance and a maximum number of iterations. This method needs a symmetric and positive definite coefficient matrix. Therefore, A must be multiplied by its transpose, so that the actual linear system to be solved becomes:

$$A^T A\mathbf{x} = A^T\mathbf{b}, \tag{2.40}$$

where A^T is the transpose of A.

The preconjugate gradient method has been preferred to an explicit decomposition of A, since the A matrix is very large and this iterative method converges much faster and using much less memory.

2.2.4 Discretization of Biot-Savart law

In this section, a matrix equation between the magnetic flux density and current density is derived [1]. The Biot-Savart law can be rewritten as:

$$d\vec{B} = \frac{m_0 I}{4p}\frac{d\vec{l}' \times \vec{R}}{R^3}, \tag{2.41}$$

for a differential current element $Id\vec{l}'$, where I is the current in one finite element and $d\vec{l}'$ is the direction of the current. The current density vector calculated previously is placed at the center of each element and weighted by the area A of the corresponding element. The differential current element can be rewritten as:

$$Id\vec{l}' = A\left(\hat{a}_x J_x + \hat{a}_y J_y + \hat{a}_z J_z\right). \qquad (2.42)$$

Similarly, the vector $\vec{R}$, between the source and field points can be explicitly written as:

$$\vec{R} = (x-x')\hat{a}_x + (y-y')\hat{a}_y + (z-z')\hat{a}_z . \qquad (2.43)$$

Therefore, the total magnetic flux density can be found integrating Equation (2.41) as follows:

$$\vec{B}(\vec{r}) = \frac{m_0}{4p}\int_{\Omega_S} \frac{\vec{J}(\vec{r}\,')\times\vec{R}}{R^3}dv' \qquad (2.44)$$

Evaluating the cross product in Equation (2.44), neglecting the effect of each current element on itself, and considering the two-dimensional case, where J_z is zero, the Equation (2.44) can be written in a matrix format as follows:

$$\left[\begin{array}{c} \mathbf{b}_x \\ \hline \mathbf{b}_y \\ \hline \mathbf{b}_z \end{array}\right] = \left[\begin{array}{cc} \mathbf{0} & \mathbf{D_z} \\ \hline -\mathbf{D_z} & \mathbf{0} \\ \hline \mathbf{D_y} & -\mathbf{D_x} \end{array}\right] \left[\begin{array}{c} \mathbf{j}_x \\ \hline \mathbf{j}_y \end{array}\right], \qquad (2.45)$$

where $\mathbf{j}_x$ and $\mathbf{j}_y$ are the column vectors of J_x, J_y values for the elements in the subject, respectively, and $\mathbf{b}_x$, $\mathbf{b}_y$ and $\mathbf{b}_z$ are the column vectors of B_x, B_y and B_z at the field points, respectively.

The matrices $\mathbf{D_x}$, $\mathbf{D_y}$ and $\mathbf{D_z}$ contain the components of the cross product:

$$\frac{m_0}{4p}\frac{dS\times\hat{a}_R}{R^2}. \qquad (2.46)$$

Their values only depend on the magnitude and direction of the $\vec{R}$ and $\hat{a}_R = \vec{R}/\left\|\vec{R}\right\|$ vectors, between the field and source points. Therefore, since they are constant for a fixed mesh structure, they can be computed once and reused if necessary.

2.3 Extraction of Magnetic Flux Density from MR Images

The magnetic flux density generated by the conductivity currents inside a conductive object can be obtained by using an MRI scanner and calculating the phase shifts between the image with the injected current and the one without. In this section, the derivation of this statement is given next [1].

The magnetization when no current is injected can be expressed as:

$$M_C\left(x,y\right)=M\left(x,y\right)e^{\{jgBt+jf_C\}}. \tag{2.47}$$

When a current is applied for a duration T_C, the magnetization accumulates a phase in the component of the magnetic flux density parallel to the main MR magnet:

$$M_{cj}\left(x,y\right)=M\left(x,y\right)e^{\left\{jg\left[Bt+B_{J,z}(x,y)T_C\right]+jf_C\right\}}. \tag{2.48}$$

Taking the ratio between (2.48) and (2.47), the effects of the phase inhomogeneities and other image artifacts are eliminated:

$$\frac{M_{cj}\left(x,y\right)}{M_C\left(x,y\right)}=e^{jg\,B_{J,z}(x,y)T_C}=e^{jgq_{JN}(x,y)}, \tag{2.49}$$

where $q_{JN}\left(x,y\right)$ is called the normalized phase image. Finally, $B_{J,z}\left(x,y\right)$can be extracted, being equal to:

$$B_{J,z}\left(x,y\right)=\frac{q_{JN}\left(x,y\right)}{gT_C}, \tag{2.50}$$

where g is the gyromagnetic ratio and T_C is the effective current application time per excitation.

Therefore, using this procedure, only the component of the magnetic flux density parallel to the main magnet of the MR device can be measured at a time.

In order to obtain the three components of the magnetic flux density, consequently, the object needs to be rotated appropriately and the pulse sequence repeated for the three different orientations. This disadvantage may not be a problem with small objects, but it is not possible to rotate a human body in existing MRI systems. The placement of the object into the MRI scanner in order to measure the three components is shown in Figure 2.3.

The coordinate system for the object is (x, y, z), while (x', y', z') is for the MR system. Since, the MR main magnet is in z'-direction, in order to image a cross-section of the object in one desired axis, this must be aligned with the z'-direction.

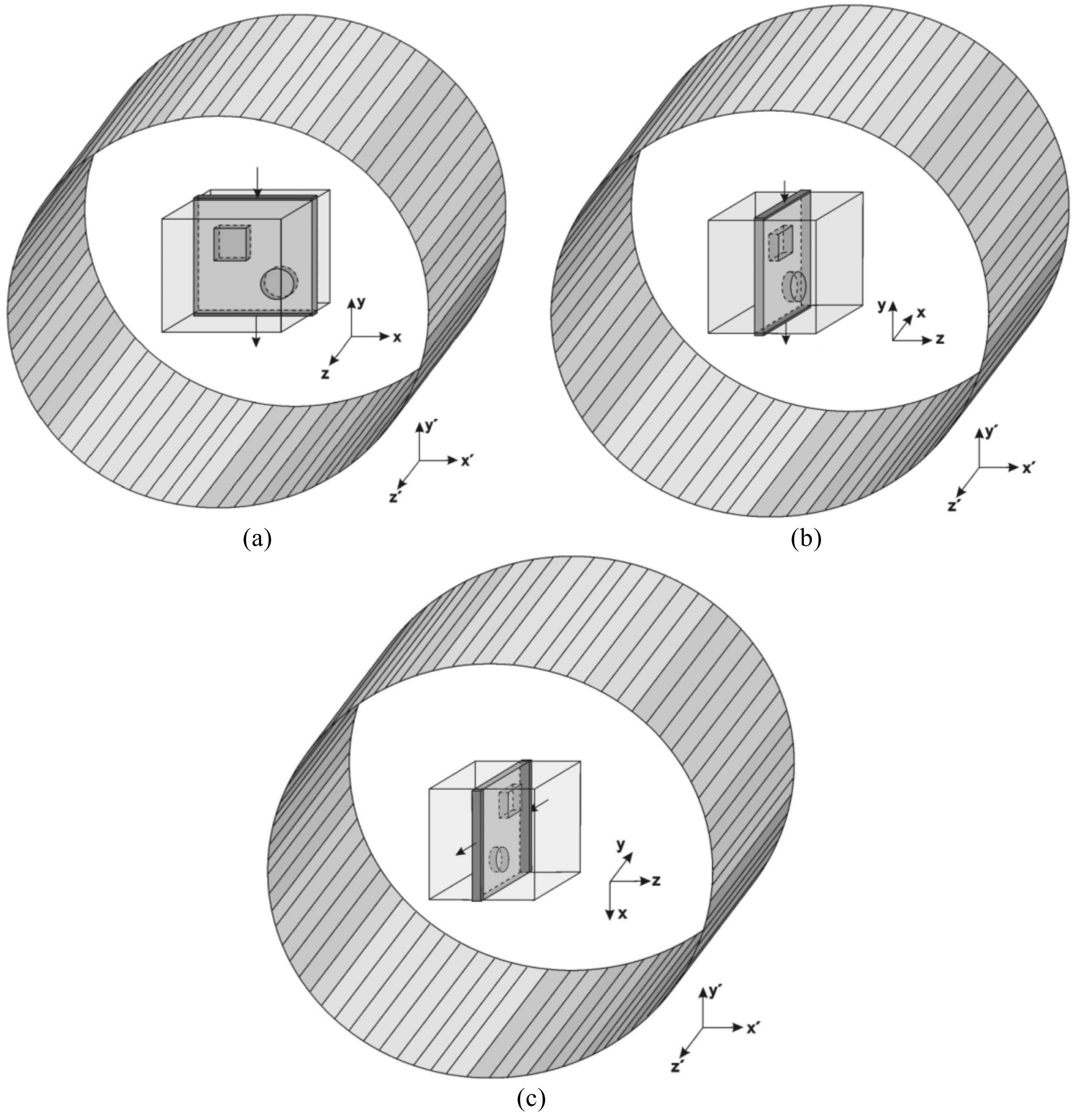

(a) (b)

(c)

Figure 2.3: Orientation of an object inside the MRI system for measuring all three components of the induced magnetic flux density. The electrodes and current injections are shown for each case. (a) Object placement for measuring B_z, (b) for measuring B_x, (c) for measuring B_y.

2.4 The Inverse Problem of MR-EIT

2.4.1 Definition

The goal of MR-EIT is to reconstruct an unknown cross-sectional resistivity distribution inside a three dimensional object. The *image reconstruction* or the solution of the *inverse problem* includes the formulation and solution methods, in order to determine the unknown inner conductivity distribution using measured internal magnetic flux density, peripheral voltage measurements, and the object boundary information [1].

Equations which describe the Inverse Problem show inherently severe ill-posed characteristics. The analytical solutions can not be found, so numerical techniques are used, instead.

2.4.2 Formulation

Let Ω be the object described in the Forward Problem, Section 2.2.2, under the same conditions and assumptions [23]. Then, the electric field is:

$$\nabla\times\vec{E}=0\,. \tag{2.51}$$

By using Ohm's law $\vec{E} = r\vec{J}$ in (2.51), it becomes:

$$\nabla\times r\vec{J}=0\,. \tag{2.52}$$

By using the following vector identity [5]:

$$\nabla\times\left(y\,\vec{A}\right)=\nabla y\,\times\vec{A}+y\nabla\times\vec{A}\,, \tag{2.53}$$

where y is a scalar field and $\vec{A}$ a vector field, the equation (2.52) can be rewritten as:

$$\nabla r\,\times\vec{J}+\,r\nabla\times\vec{J}=0\,. \tag{2.54}$$

Dividing both sides by r and rearranging the terms, it yields to:

$$\frac{\nabla r}{r} \times \vec{J} = -\nabla \times \vec{J} \,. \tag{2.55}$$

For simplicity, calling $\Re = \ln r$, that is, the natural logarithm of the resistivity, it can be rewritten as:

$$\nabla \Re \times \vec{J} = -\nabla \times \vec{J} \,. \tag{2.56}$$

If $\vec{J}$ is known, this equation (2.56) contains all the information about the resistivity distribution in the gradient-of-$\Re$ term. But, in practice, only the magnetic flux density can be directly measured by MRI. The needed $\vec{J}$ could be found by Ampere's law:

$$\vec{J} = \nabla \times \vec{B} / m_0 \,. \tag{2.57}$$

Instead of using this approach, if Ampere's law is substituted in (2.56):

$$\nabla \Re \times \vec{J} = -\nabla \times \left(\nabla \times \vec{B} / m_0 \right), \tag{2.58}$$

and using the vector identity [5]:

$$\nabla \times \left(\nabla \times \vec{A} \right) = \nabla \left(\nabla \cdot \vec{A} \right) - \nabla^2 \vec{A} \,, \tag{2.59}$$

where $\vec{A}$ is a vector field, it gives:

$$\nabla \Re \times \vec{J} = -\nabla \left(\nabla \cdot \vec{B} / m_0 \right) + \nabla^2 \, \vec{B} / m_0 \,. \tag{2.60}$$

Knowing that the divergence of the magnetic flux density is zero, since it is a solenoidal field, the final expression turns to be:

$$\nabla \Re \times \vec{J} = \nabla^2 \, \vec{B} / m_0 \,. \tag{2.61}$$

The Equation (2.61) can be expressed in terms of conductivity, instead. Then, similar derivation beginning from (2.51) can be carried out. Knowing that $\vec{E} = \vec{J} / s$, using the identity (2.53) and that $\nabla \left(1/s \right) = -\nabla s / s^2$, it yields:

$$\frac{\nabla s}{s} \times \vec{J} = -\nabla \times \vec{J} \,. \tag{2.62}$$

Using now Ampere's law, the identity (2.59) and that the divergence of $\vec{B}$ is zero, Equation (2.62) becomes:

$$\frac{\nabla s}{s}\times\vec{J} = -\nabla^{2}\vec{B}/m_{0} \, . \tag{2.63}$$

Finally, knowing that $\vec{E} = -\nabla f$, where f is the potential distribution inside the object, results [27]:

$$\nabla^{2}\,\vec{B}/m_{0} = -\nabla f \times \nabla s \; . \tag{2.64}$$

But, this equation still needs to know the current density distribution $\vec{J}$. Moreover, the Laplacian of the magnetic field density involves second order derivatives of $\vec{B}$, which will decrease the quality of the reconstructed resistivity and make it more vulnerable to noise, due to the blurring effect of this operator. But, if $\vec{J}$ is calculated by Ampere's law and Equation (2.56) is used, the reconstruction has a better quality.

In the computation of $\vec{J}$ inside the object by Ampere's law, solving the curl operation implies measuring the three components of the magnetic flux density $\vec{B}(x,y,z)$. But, as it was stated before, only the parallel component of the magnetic flux density to the main magnet of the MR system can be obtained, so the object must be rotated to obtain the three components.

In order to overcome this difficulty, reconstruction algorithms which only use one component of $\vec{B}$ and cancel the other two are needed. Then, this kind of algorithms, based on (2.61) or (2.64), would have practical advantages.

2.4.3 Classification of the Reconstruction Algorithms

A reconstruction algorithm is a systematic way to find the resistivity by solving the equations which define the inverse problem. Algorithms proposed for this purpose can be grouped into two.

The first group is called *Current Density based* algorithms, since they use the current density distribution, calculated from the magnetic flux density measurements. They try to solve the problems described in Equation (2.56).

The second group is known as *Magnetic Flux based* algorithms, because they utilize magnetic flux density measurements directly. They try to solve Equation (2.61) or (2.64).

Both types have iterative or non-iterative versions.

The current density based algorithms studied in the thesis, except the J-substitution algorithm, are non-iterative. The magnetic flux density based algorithm implemented in the thesis is also iterative. It requires only the *z*-component of $\vec{B}$, that is, B_z, but needs some iterations to obtain the true conductivity distribution.

CHAPTER 3

CURRENT DENSITY BASED RECONSTRUCTION ALGORITHMS

3.1 Derivation of Reconstruction Algorithms

In Section 2.4, in the formulation of the inverse problem, Equation (2.56) related the resistivity distribution inside the object to the current density distribution as follows:

$$\nabla\Re\times\vec{J}=-\nabla\times\vec{J}\,. \tag{3.1}$$

Performing the curl operator in both sides, and rearranging terms, Equation (3.1) can be expressed as the following matrix equation:

$$\begin{bmatrix} 0 & J_z & -J_y \\ -J_z & 0 & J_x \\ J_y & -J_x & 0 \end{bmatrix}\begin{bmatrix} \dfrac{\partial\Re}{\partial x} \\ \dfrac{\partial\Re}{\partial y} \\ \dfrac{\partial\Re}{\partial z} \end{bmatrix}=-\begin{bmatrix} \dfrac{\partial J_z}{\partial y}-\dfrac{\partial J_y}{\partial z} \\ \dfrac{\partial J_x}{\partial z}-\dfrac{\partial J_z}{\partial x} \\ \dfrac{\partial J_y}{\partial x}-\dfrac{\partial J_x}{\partial y} \end{bmatrix} \tag{3.2}$$

The following four reconstruction algorithms: reconstruction by integration along equipotential lines, reconstruction by integration along Cartesian grid lines, reconstruction by solution of a linear system of equations using finite differences, and reconstruction with equipotential-projection algorithm deal in different ways with the matrix equation (3.2), in order to solve the logarithmic resistivity $\Re$, and from there, obtain the resistivity r or conductivity s distribution. The J-substitution algorithm, however, tries to solve the forward problem iteratively, updating the resistivity distribution in every iteration.

3.2 Reconstruction by Integration along Equipotential Lines

Ider *et al* [15] show that each row of the system in (3.2) is a first-order linear hyperbolic partial differential equation, and that the characteristic surfaces of the hyperbolic system (3.2) are, in fact, equipotential surfaces.

This algorithm calculates $\Re$ on a whole equipotential surface, provided that $\Re$ is known at a single point on it. The logarithmic resistivity $\Re$ can be found at any point in the equipotential surface by integrating along any path in the surface, starting from the specified point [15].

This theory can be applied to the third row in the equation system (3.2):

$$\frac{\partial \Re}{\partial x} J_y - \frac{\partial \Re}{\partial y} J_x = -\left(\frac{\partial J_y}{\partial x} - \frac{\partial J_x}{\partial y} \right) \tag{3.3}$$

Since the third entry of the third row is zero, this Equation (3.3) has characteristic curves which stay in the same $z = k$ plane as their starting points, where k is a constant.

Consider now a $z = k$ plane. Let Ω_{xy}^{k} be the intersection of this plane with Ω. In Ω_{xy}^{k}, the $\begin{bmatrix} \frac{\partial \Re}{\partial x} & \frac{\partial \Re}{\partial y} \end{bmatrix}^T$ term in (3.3) corresponds to the projection of ∇R onto Ω_{xy}^{k}. Then, the left-hand side of Equation (3.3) can be interpreted as the projection of this two-dimensional gradient onto the $\begin{bmatrix} J_y & -J_x \end{bmatrix}^T$ direction, which is perpendicular to the current density direction $\begin{bmatrix} J_x & J_y \end{bmatrix}^T$. Thus, the characteristic curves are perpendicular to the current streamlines and are, in fact, equipotential lines. Consequently, by integrating along the equipotential lines in Ω_{xy}^{k}, the logarithmic resistivity $\Re$ can be calculated, provided that $\Re$ is known on at least one point in each equipotential line.

Assume now that two different current injection patterns are used and two internal current density distributions $\mathbf{J}^1$ and $\mathbf{J}^2$ are measured. Let $\mathbf{J}^1_{xy}$ and $\mathbf{J}^2_{xy}$ be the projections of $\mathbf{J}^1$ and $\mathbf{J}^2$ in Ω^c_{xy} onto Ω^c_{xy}. If the condition $\mathbf{J}^1_{xy} \times \mathbf{J}^2_{xy} \neq 0$ holds for at least one point on each equipotential line of one injection pattern, then, $\Re$ needs to be specified only at a single point in Ω^c_{xy} [15].

Similarly, it is possible to obtain slice images for Ω^c_{yz} and Ω^c_{xz} using the first and second rows of Equation (3.2).

3.2.1 Implementation

3.2.1.1 Obtaining the Equipotential Lines

In the simulations, the current density data for each injection pattern is given. Since the equipotential lines are always perpendicular to the direction of the currents, they can be calculated in each pixel.

The procedure is the following. Starting from the four edges of the phantom, several equipotential lines per pixel are initiated. The direction perpendicular to the current density vector in each pixel is used to calculate the outgoing coordinates of the equipotential line from the incoming coordinates.

In Figure 3.1, an example with four pixels and two equipotential lines per pixel, starting from the left edge is shown.

An equipotential line can cross a pixel in twenty different ways, as shown in Figure 3.2. All these cases are considered in order to obtain the path that an equipotential line runs throughout the imaging region, from its starting point, at an edge, till it leaves the slice.

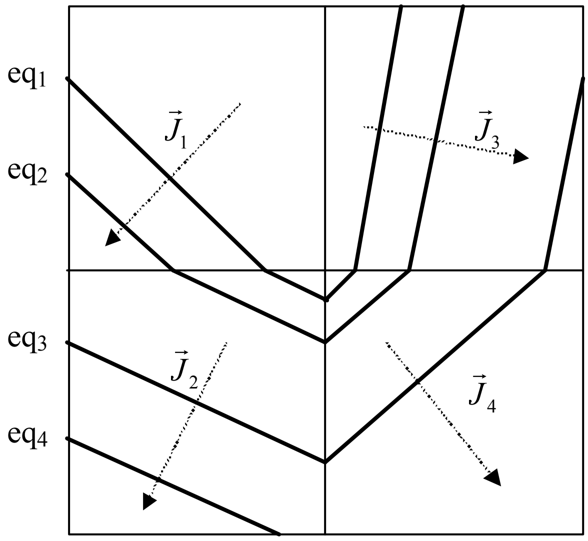

Figure 3.1: Two equipotential lines are started from each pixel at the left boundary. They are perpendicular to the current density vector in every pixel within the image.

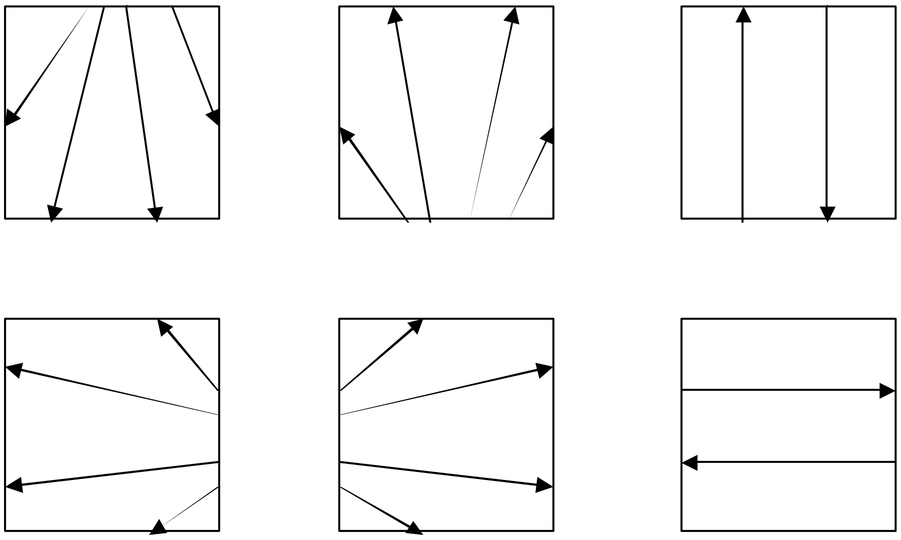

Figure 3.2: An equipotential line can pass through a pixel in twenty different ways.

3.2.1.2 Integration Methods

Once the equipotential lines have been obtained, the logarithmic resistivity on any point on an equipotential line can be calculated by integrating the gradient of $\Re$ along these paths. This is possible if one $\Re$ value is known on at least one point in each equipotential line. In the current implementation, $\Re$ is known at the edge from where the equipotential lines begin.

For example, it is possible to obtain approximately $\Re$ at the point s of the path l if the value of $\Re$ at point $s = s_1$ is known, as shown in Figure 3.3.

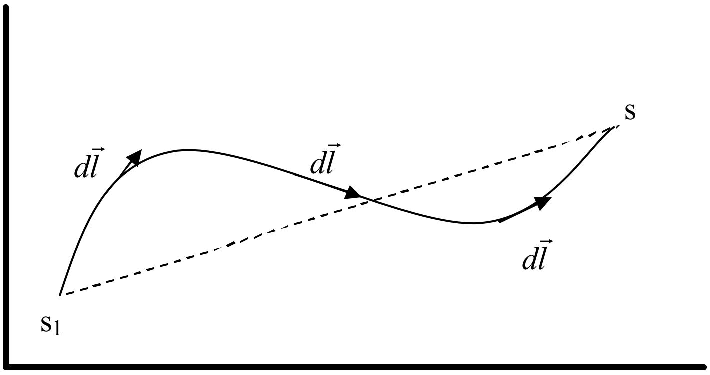

Figure 3.3: Integration path from s1 to s

Then,

$$R(s) = R(s_1) + \int_{s_1}^{s} -\left(\frac{\partial J_y}{\partial x} - \frac{\partial J_x}{\partial y}\right) d\vec{l} \,, \tag{3.4}$$

where $d\vec{l}$ is a differential line increment. In Cartesian coordinates, this is equal to:

$$d\vec{l} = (dx, dy) \,. \tag{3.5}$$

In order to perform the integration described in Equation (3.4), two integration techniques are provided and compared: the Trapezoidal method and Taylor Expansion integration method.

The Trapezoidal Rule is based on the Newton-Cotes Formula [34], which states that if the integrand can be approximated by an nth order polynomial

$$I = \int_a^b f(x)dx, \tag{3.6}$$

where $f(x) \approx f_n(x)$ and $f_n(x) = a_0 + a_1 x + \ldots + a_{n-1}x^{n-1} + a_n x^n$ then, the integral of that function is approximated by the integral of that nth order polynomial.

$$\int_a^b f(x) \approx \int_a^b f_n(x). \tag{3.7}$$

The Trapezoidal Rule assumes that $n = 1$. Then, the integral can be approximated by the area under the linear polynomial, as indicated in Equation (3.8)

$$\int_a^b f(x)dx \approx (b-a)\left[\frac{f(a)+f(b)}{2}\right]. \tag{3.8}$$

The first-order Taylor Expansion around $x = x_0$ can be also used as another integration method. The expression is given in Equation (3.9):

$$f(x) = f(x_0) + \left.\frac{\partial f(x)}{\partial x}\right|_{x_0} (x - x_0). \tag{3.9}$$

3.2.1.3 Integrating along the Equipotential Lines

Once the integration paths, i.e., equipotential lines, have been calculated, knowing that $\vec{dl} = (dx, dy)$, the Equation (3.4) can be rewritten as follows:

$$\Re(s) = \Re(s_1) - \int_{s_1}^{s} \frac{\partial J_y}{\partial x} dx + \int_{s_1}^{s} \frac{\partial J_x}{\partial y} dy. \tag{3.10}$$

Applying the trapezoidal method of integration to it yields:

$$\begin{aligned}\Re(s)=\Re(s_1)&-\left[\frac{\partial J_y(s_1)}{\partial x}+\frac{\partial J_y(s)}{\partial x}\right]\frac{(s_x-s_{1x})}{2}\\&+\left[\frac{\partial J_x(s_1)}{\partial y}+\frac{\partial J_x(s)}{\partial y}\right]\frac{(s_y-s_{1y})}{2}.\end{aligned}\tag{3.11}$$

Calling $\Delta x=(s_x-s_{1x})$ and $\Delta y=(s_y-s_{1y})$, the final equation is:

$$\Re(s)=\Re(s_1)-\left(\frac{\partial J_y(s_1)}{\partial x}+\frac{\partial J_y(s)}{\partial x}\right)\frac{\Delta x}{2}+\left(\frac{\partial J_x(s_1)}{\partial y}+\frac{\partial J_x(s)}{\partial y}\right)\frac{\Delta y}{2}.\tag{3.12}$$

In case one single equipotential line crosses each pixel, as shown in Figure 3.4, the Equation (3.12) becomes Equation (3.13).

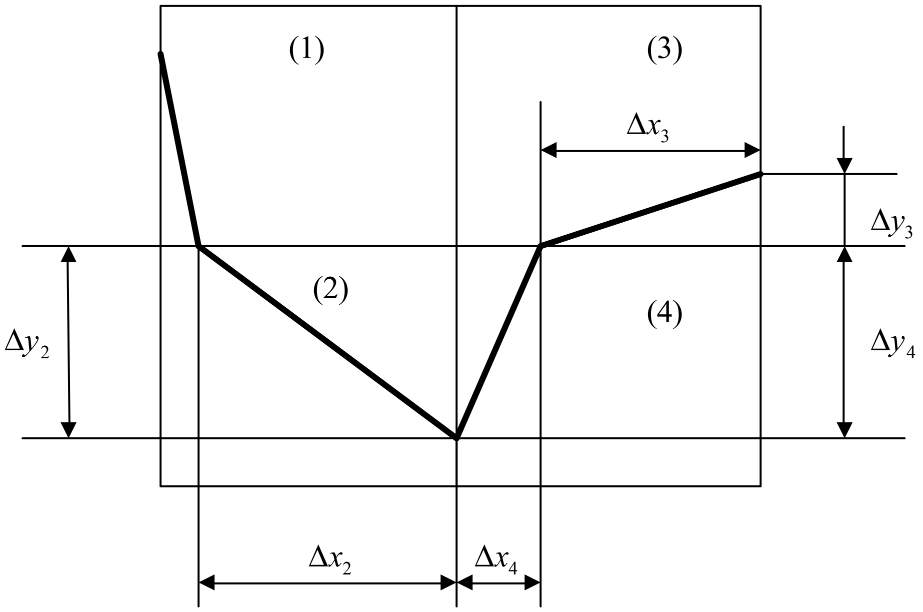

Figure 3.4: Integration case if one single equipotential line passes through each pixel.

$$\Re(2)=\Re(1)-\left[\frac{\partial J_y(1)}{\partial x}+\frac{\partial J_y(2)}{\partial x}\right]\frac{\Delta x_2}{2}+\left[\frac{\partial J_x(1)}{\partial y}+\frac{\partial J_x(2)}{\partial y}\right]\frac{\Delta y_2}{2}.\tag{3.13}$$

If more than one equipotential line crosses each pixel, an averaging is needed. For example, in Figure 3.5, two equipotential lines pass through pixel (3), and Equation (3.12) becomes Equation (3.14).

$$\begin{aligned}\Re(3)=&\frac{1}{2}\left[\Re(1)-\left(\frac{\partial J_y(1)}{\partial x}+\frac{\partial J_y(3)}{\partial x}\right)\frac{\Delta x_{31}}{2}+\left(\frac{\partial J_x(1)}{\partial y}+\frac{\partial J_x(3)}{\partial y}\right)\frac{\Delta y_{31}}{2}\right]+\\&+\frac{1}{2}\left[\Re(4)-\left(\frac{\partial J_y(4)}{\partial x}+\frac{\partial J_y(3)}{\partial x}\right)\frac{\Delta x_{34}}{2}+\left(\frac{\partial J_x(4)}{\partial y}+\frac{\partial J_x(3)}{\partial y}\right)\frac{\Delta y_{34}}{2}\right].\end{aligned}\tag{3.14}$$

In general, if in the pixel p_0 there are $n_{eqLines}$ equipotential lines, coming each one from a previous pixel p_i, the Equation (3.12) could be written as:

$$\begin{aligned}\Re(p_0)=\frac{1}{n_{eqLines}}\sum_{i=1}^{n_{eqLines}}&\left[\Re(p_i)-\left(\frac{\partial J_y(p_i)}{\partial x}+\frac{\partial J_y(p_0)}{\partial x}\right)\frac{\Delta x_{0i}}{2}\right.\\&\left.+\left(\frac{\partial J_x(p_i)}{\partial y}+\frac{\partial J_x(p_0)}{\partial y}\right)\frac{\Delta y_{0i}}{2}\right].\end{aligned}$$

(15)^

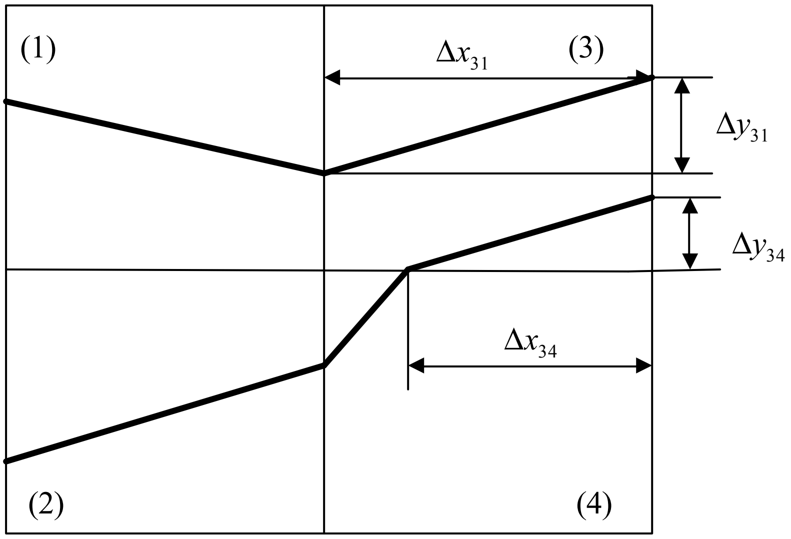

Figure 3.5: Integration case when more than one equipotential line passes per one pixel.

Notice that, in order to calculate the value of $\Re$ in one pixel, it is necessary to know $\Re$ in the previous pixel, from where the equipotential line is coming. For example, in Figure 3.5, in order to calculate $\Re$ (3), $\Re$ (1) and $\Re$ (4) are needed. But to calculate $\Re$ (4), $\Re$ (2) is also needed. Therefore, a recursive algorithm is required.

This recursive algorithm takes an equipotential line and begins from its very end pixel. For each equipotential line in that pixel, it checks if the pixel from where it comes is already processed or not. If so, the $\Re$ in that previous pixel is currently known. If not, it processes it, recursively. When all involved $\Re$'s are known, the integration is then performed, and the $\Re$ in the pixel can be calculated.

The stopping criterion for this recursive algorithm is that the $\Re$ values of all pixels at the edge from where the equipotential lines start are calculated.

Finally, in order to compute the current density derivatives involved in the equations, the Sobel Operator has been applied, as described in [27]:

$$\frac{\partial J_y}{\partial x} = \frac{1}{8\Delta x}\begin{bmatrix} -1 & 0 & 1 \\ -2 & 0 & 2 \\ -1 & 0 & 1 \end{bmatrix} ** J_y \tag{3.16}$$

and

$$\frac{\partial J_x}{\partial y} = \frac{1}{8\Delta y}\begin{bmatrix} 1 & 2 & 1 \\ 0 & 0 & 0 \\ -1 & -2 & -1 \end{bmatrix} ** J_x . \tag{3.17}$$

3.3 Reconstruction by Integration along Cartesian Grid Lines

In order to simplify the previous algorithm, the integration along a Cartesian grid may be preferred.

Ider *et al* [15] claim that, f the gradient of the logarithmic resistivity $\Re$ is known within the subject Ω, then $\Re$ can be found by integrating its gradient along Cartesian grid lines, except for an additive constant. This is equivalent to specifying the potential function at a single point in Ω.

The gradient of $\Re$ cannot be found for a single injected current profile, since the determinant of the coefficient matrix in Equation (3.2) is zero. Let $\vec{J}_1$ and $\vec{J}_2$ be the current density measurements, corresponding to two different applied injection patterns. Then, within the imaging slice in *xy* plane, the third row of Equation (3.2) can be written twice to obtain:

$$\begin{bmatrix} J_y^1 & -J_x^1 \\ J_y^2 & -J_x^2 \end{bmatrix} \begin{bmatrix} \dfrac{\partial \Re}{\partial x} \\ \dfrac{\partial \Re}{\partial y} \end{bmatrix} = \begin{bmatrix} \dfrac{\partial J_x^1}{\partial y} - \dfrac{\partial J_y^1}{\partial x} \\ \dfrac{\partial J_x^2}{\partial y} - \dfrac{\partial J_y^2}{\partial x} \end{bmatrix}. \tag{3.18}$$

From this new set of equations, it is possible to calculate the gradient of $\Re$ $\begin{bmatrix} \dfrac{\partial \Re}{\partial x} & \dfrac{\partial \Re}{\partial y} \end{bmatrix}^T$ at any point, provided that for that point the determinant $-J_y^1 J_x^2 + J_y^2 J_x^1$ is not zero, or equivalently:

$$\vec{J}_{xy}^1 \times \vec{J}_{xy}^2 \neq 0, \tag{3.19}$$

where $\vec{J}_{xy}^1$ and $\vec{J}_{xy}^2$ are the projections of $\vec{J}_1$ and $\vec{J}_2$, respectively, on the *xy* plane.

After finding the gradient of $\Re$, using the first or second row of Equation (3.2), it is possible to obtain $\partial\Re/\partial z$ if at least one of the conditions ($J_y^1 \neq 0$ or $J_y^2 \neq 0$)

or ($J_x^1 \neq 0$ or $J_x^2 \neq 0$) is satisfied, respectively. Since the condition in Equation (3.19) is already required, one of those two conditions will hold anyway.

Handling the rows of Equation (3.2) in different orders, it can be seen that to find the gradient of $\Re$ at any point, it is also sufficient to have $\left(J_{xz}^1 \times J_{xz}^2\right) \neq 0$ or $\left(J_{yz}^1 \times J_{yz}^2\right) \neq 0$ at that point.

In general, if

$$J^1 \times J^2 = J_{yz}^1 \times J_{yz}^2 + J_{xz}^1 \times J_{xz}^2 + J_{xy}^1 \times J_{xy}^2 \neq 0 \tag{3.20}$$

at a certain point, then the gradient at that point can be calculated, because at least one of the terms in Equation (3.20) will not vanish [15]. In practice, it may be needed to employ more than two injection patterns, because the condition in (3.20) may not be satisfied at all points by a single pair of injection patterns.

Note that by finding $\begin{bmatrix} \frac{\partial \Re}{\partial x} & \frac{\partial \Re}{\partial y} \end{bmatrix}^T$ for only one xy plane, $\Re$ can only be reconstructed at that plane, i.e. slice, apart from an additive constant, without being concerned about finding the gradient at other xy slices. Similarly, this occurs for xz and yz slices.

3.3.1 Implementation

In order to obtain the gradient of $\Re$ from the Equation (3.18), it is necessary to calculate firstly:

$$\begin{bmatrix} J_y^1 & -J_x^1 \\ J_y^2 & -J_x^2 \end{bmatrix} \tag{3.21}$$

and

$$\begin{bmatrix} \frac{\partial J_x^1}{\partial y} - \frac{\partial J_y^1}{\partial x} \\ \frac{\partial J_x^2}{\partial y} - \frac{\partial J_y^2}{\partial x} \end{bmatrix}. \tag{3.22}$$

The derivatives of Equation (3.22) have been found by applying the Sobel Operator [27] given in Equation (3.16) and Equation (3.17).

After obtaining the gradient of $\Re$, the actual distribution of $\Re$ in every pixel can be obtained by integration, using the methods explained previously in Section 3.2.1.2.

3.4 Reconstruction by Solution of a Linear Equation System using Finite Differences

Ider *et al* [15] state that any row of Equation (3.2) can be discretized by using finite differences on a rectangular mesh. For example, for a slice placed on the *xy* plane, the third row of Equation (3.2) is chosen. This discretization is done for each node within the slice and for every current injection pattern. A matrix equation can be built by combining all the equations involved in the discretization. Then, the logarithmic resistivity $\Re$ can be found with a matrix inversion.

3.4.1 Algorithm

Let the slice image be on the *xy* plane. Then, the third row of Equation (3.2), which was:

$$\frac{\partial \Re}{\partial x} J_y - \frac{\partial \Re}{\partial y} J_x = -\left(\frac{\partial J_y}{\partial x} - \frac{\partial J_x}{\partial y} \right) \tag{3.23}$$

can be discretized on a $N \times N$ Cartesian grid, by using finite differences [33]. Each pixel in the image holds the logarithmic resistivity $\Re$ at their center point. There are three types of subsqueres: interior pixels, boundary pixels and corner pixels, which correspond with nine different cases. In the next Section 3.4.2, expressions for all of them will be given.

For example, for the inner points, central differences can be applied to Equation (3.23) in order to approximate the derivatives in x and y direction. The result is:

$$\begin{aligned}&\frac{\Re_{(i+1,j)}-\Re_{(i-1,j)}}{2\Delta x}J_{y(i,j)}-\frac{\Re_{(i,j+1)}-\Re_{(i,j-1)}}{2\Delta y}J_{x(i,j)}\\&=-\left(\frac{J_{y(i+1,j)}-J_{y(i-1,j)}}{2\Delta x}-\frac{J_{x(i,j+1)}-J_{x(i,j-1)}}{2\Delta y}\right),\end{aligned}\tag{3.24}$$

where Δx and Δy are the discretization steps in x and y directions, respectively, and i and j are the indices of the center of the pixels in x and y directions, respectively. For the rest of cases, backward, forward or central differences are applied.

Once all the pixel elements are discretized, rearranging the set of finite difference equations, the following linear system is obtained:

$$\mathbf{CR}=\mathbf{B},\tag{3.25}$$

where $\mathbf{C}$ is a $N^2\times N^2$ matrix containing the coefficient of $\Re$ in the left-hand side part of Equation (3.24), $\mathbf{R}=\begin{bmatrix}\Re_0 & \Re_2 & \cdots & \Re_{N^2-1}\end{bmatrix}^T$ is the logarithmic resistivity distribution of the slice in vector form, and $\mathbf{B}$ are the current density terms on the right-hand side of Equation (3.24).

If M different injected current patterns are carried out, the coefficient matrix $\mathbf{C}$ and the right-hand side vectors $\mathbf{B}$ can be concatenated in order to obtain the following set of equations:

$$\begin{bmatrix}\underline{\mathbf{C}_1}\\ \underline{\mathbf{C}_2}\\ \underline{\vdots}\\ \mathbf{C}_M\end{bmatrix}\mathbf{R}=\begin{bmatrix}\underline{\mathbf{B}_1}\\ \underline{\mathbf{B}_2}\\ \underline{\vdots}\\ \mathbf{B}_M\end{bmatrix}.\tag{3.26}$$

At least two injection patterns must be performed in order to satisfy the condition given previously in Equation (3.20).

3.4.2 Implementation

Let the square target imaging region $\Omega_S:(-L,L)\times(-L,L)$ be uniformly divided into $N\times N$ axis-parallel sub squares Ω_{i+jN}, containing the logarithmic resistivity

$\Re$ values of the image at their center point (x_i, y_j), where $i = 0,\ldots,N-1$ and $j = 0,\ldots,N-1$. The logarithmic resistivity $\Re$ is assumed to be constant on each subsquare Ω_k, denoted by $\Re_k$, where $k = 1,\ldots,N^2$. As it was stated before, there are three types of subsquares: in the interior, on the boundaries, and the corners. The nine different cases can be shown in Figure 5.12(b). Expressions for each of these cases are given below.

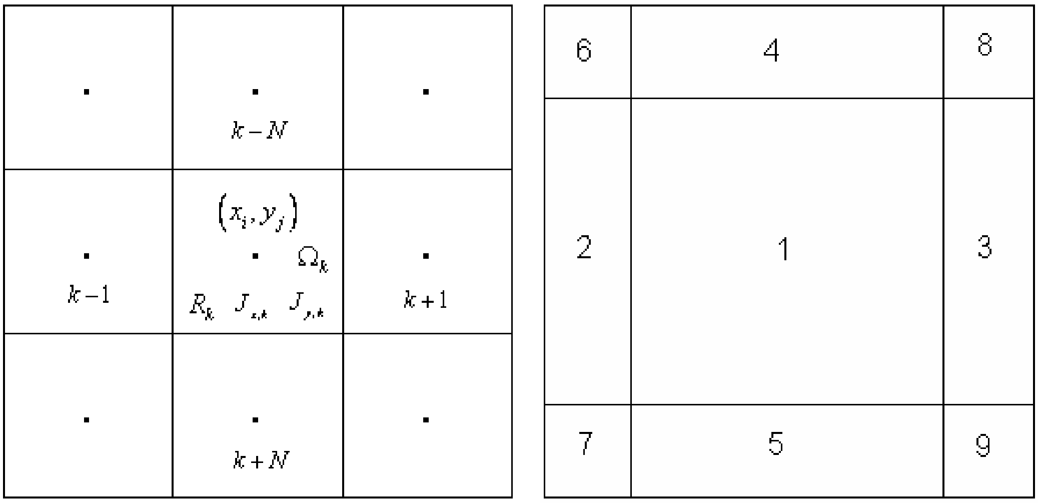

(a) (b)

Figure 3.6: Reconstruction by solution of a linear equation system. (a) $\Re_k$, $J_{x,k}$ and $J_{y,k}$ at every element Ω_k and surrounding elements. (b) In the implementation, nine different types of elements are considered.

Firstly, considering an inner element Ω_k.

$$k = i + jN + 1 \quad \text{for} \quad 1 \le i, \quad j \le N-2,$$

Equation (3.23) can be discretized using central differences in x and y direction. It becomes:

$$\begin{aligned} &\frac{J_{x,k}}{2\Delta y}\Re_{k+N} - \frac{J_{x,k}}{2\Delta y}\Re_{k-N} + \frac{J_{y,k}}{2\Delta x}\Re_{k+1} - \frac{J_{y,k}}{2\Delta x}\Re_{k-1} \\ &= \frac{J_{x,k-N} - J_{x,k+N}}{2\Delta y} + \frac{J_{y,k-1} - J_{y,k+1}}{2\Delta x}, \end{aligned} \tag{3.27}$$

where $J_{x,k}$ represents the conductivity density in x direction in the pixel k, and Δx and Δy are the element length in x and y direction, respectively. In this case, $\Delta x = \Delta y = 2L / N$.

In order to obtain the expression for the upper boundary, i.e.:

$$k = i + jN + 1 \quad \text{for} \quad 1 \leq i \leq N-2 \text{ and } j = 0,$$

central differences are taken for x direction, while only forward differences in y direction. Then, the Equation (3.23) is approximated by:

$$\begin{aligned} &\frac{J_{x,k}}{\Delta y}\Re_{k+N} - \frac{J_{x,k}}{\Delta y}\Re_{k} + \frac{J_{y,k}}{2\Delta x}\Re_{k+1} - \frac{J_{y,k}}{2\Delta x}\Re_{k-1} \\ &= \frac{J_{x,k} - J_{x,k+N}}{\Delta y} + \frac{J_{y,k-1} - J_{y,k+1}}{2\Delta x}. \end{aligned} \tag{3.28}$$

Similarly, for the lower boundary of the image, i.e.:

$$k = i + jN + 1 \quad \text{for} \quad 1 \leq i \leq N-2 \text{ and } j = N-1,$$

central differences are taken for x direction, and backward differences in y direction. Then, the Equation (3.23) is approximated by:

$$\begin{aligned} &\frac{J_{x,k}}{\Delta y}\Re_{k} - \frac{J_{x,k}}{\Delta y}\Re_{k-N} + \frac{J_{y,k}}{2\Delta x}\Re_{k+1} - \frac{J_{y,k}}{2\Delta x}\Re_{k-1} \\ &= \frac{J_{x,k-N} - J_{x,k}}{\Delta y} + \frac{J_{y,k-1} - J_{y,k+1}}{2\Delta x}. \end{aligned} \tag{3.29}$$

Equivalent procedure can be used to obtain the left-hand side boundary:

$$k = i + jN + 1 \quad \text{for} \quad i = 0 \text{ and } 1 \leq j \leq N-2,$$

by using central differences in y direction and forward in x direction. Equation (3.23) becomes:

$$\begin{aligned} &\frac{J_{x,k}}{2\Delta y}\Re_{k+N} - \frac{J_{x,k}}{2\Delta y}\Re_{k-N} + \frac{J_{y,k}}{\Delta x}\Re_{k+1} - \frac{J_{y,k}}{\Delta x}\Re_{k} \\ &= \frac{J_{x,k-N} - J_{x,k+N}}{2\Delta y} + \frac{J_{y,k} - J_{y,k+1}}{\Delta x}. \end{aligned} \tag{3.30}$$

For the right-hand side boundary elements, such that,

$$k = i + jN + 1 \quad \text{for} \quad i = N-1 \text{ and } 1 \le j \le N-2,$$

Equation (3.23) is approximated by backward differences in x direction and central differences in y direction, resulting:

$$\begin{aligned} &\frac{J_{x,k}}{2\Delta y}\Re_{k+N} - \frac{J_{x,k}}{2\Delta y}\Re_{k-N} + \frac{J_{y,k}}{\Delta x}\Re_{k} - \frac{J_{y,k}}{\Delta x}\Re_{k-1} \\ &= \frac{J_{x,k-N} - J_{x,k+N}}{2\Delta y} + \frac{J_{y,k-1} - J_{y,k}}{\Delta x}. \end{aligned} \tag{3.31}$$

Finally, for the four corner elements, such that

$$k = i + jN + 1 \quad \text{for} \quad i, j = 0 \text{ or } N-1$$

forward or backward differences are used. The expression for the upper-left one, where $k = 1$, becomes:

$$\begin{aligned} &\frac{J_{x,k}}{\Delta y}\Re_{k+N} - \left(\frac{J_{x,k}}{\Delta y} + \frac{J_{y,k}}{\Delta x}\right)\Re_{k} + \frac{J_{y,k}}{\Delta x}\Re_{k+1} \\ &= \frac{J_{x,k} - J_{x,k+N}}{\Delta y} + \frac{J_{y,k} - J_{y,k+1}}{\Delta x}. \end{aligned} \tag{3.32}$$

In case of the upper-right corner, with $k = N$, it results:

$$\begin{aligned} &\frac{J_{x,k}}{\Delta y}\Re_{k+N} + \left(\frac{J_{y,k}}{\Delta x} - \frac{J_{x,k}}{\Delta y}\right)\Re_{k} - \frac{J_{y,k}}{\Delta x}\Re_{k-1} \\ &= \frac{J_{x,k} - J_{x,k+N}}{\Delta y} + \frac{J_{y,k-1} - J_{y,k}}{\Delta x}. \end{aligned} \tag{3.33}$$

For the lower-left corner, where $k = N(N-1)+1$, it yields:

$$\begin{aligned} &-\frac{J_{x,k}}{\Delta y}\Re_{k-N} + \left(\frac{J_{x,k}}{\Delta y} - \frac{J_{y,k}}{\Delta x}\right)\Re_{k} + \frac{J_{y,k}}{\Delta x}\Re_{k+1} \\ &= \frac{J_{x,k-N} - J_{x,k}}{\Delta y} + \frac{J_{y,k} - J_{y,k+1}}{\Delta x}. \end{aligned} \tag{3.34}$$

And, finally, the expression for the lower-right corner, where $k = N^2$, the Equation (3.23) is approximated by:

$$-\frac{J_{x,k}}{\Delta y}\Re_{k-N} + \left(\frac{J_{y,k}}{\Delta x} + \frac{J_{x,k}}{\Delta y}\right)\Re_k - \frac{J_{y,k}}{\Delta x}\Re_{k-1} = \frac{J_{x,\,k-N} - J_{x,k}}{\Delta y} + \frac{J_{y,k-1} - J_{y,k}}{\Delta x}. \tag{3.35}$$

As previously stated, rearranging the terms in Equations (3.27) to (3.35) and combining them, the matrix equation (3.25) can be formed. In the current implementation of this algorithm, two orthogonal injection patterns have been used. Therefore, this procedure has been repeated twice. Concatenating the **C** and **B** matrices for each injection profile, the following matrix equation results:

$$\left[\frac{\mathbf{C}_1}{\mathbf{C}_2}\right]\mathbf{R} = \left[\frac{\mathbf{B}_1}{\mathbf{B}_2}\right] \tag{3.36}$$

The rank of the combined **C** matrix is $N^2 - 1$, as expected, since a function can be reconstructed from its gradient, except for an additional constant [15]. It is necessary to set one of the $\Re$'s to its real value and then solve the equation system with full rank, in order to obtain the logarithmic resistivity $\Re$ in the slice. For example, in order to set $\Re_0$ to its true value $\Re_0^{real}$, then the first row of **C₁** must be changed, such that its element $c_{0,0} = 1$, while the rest $c_{0,k} = 0$ for all $k = 1,\ldots,N^2 - 1$. Also, the element b_0 of **B₁** must be set to $b_0 = \Re_0^{real}$. Now, the matrix is full rank and the system can be solved in order to get the true $\Re$.

The linear system (3.36) has been solved by using the preconjugate gradient method. This requires that the coefficient matrix **C** must be symmetric and positive definite. In order to do that, **C** is multiplied by its transpose. Hence, the actual linear system to be solved becomes:

$$\left[\mathbf{C}_1^T \middle| \mathbf{C}_2^T\right]\left[\frac{\mathbf{C}_1}{\mathbf{C}_2}\right]\mathbf{R} = \left[\mathbf{C}_1^T \middle| \mathbf{C}_2^T\right]\left[\frac{\mathbf{B}_1}{\mathbf{B}_2}\right], \tag{3.37}$$

where $\mathbf{C}_1^T$ and $\mathbf{C}_2^T$ are the transposes of $\mathbf{C}_1$ and $\mathbf{C}_2$, respectively.

This method has been preferred to an SVD decomposition of **C**, due to the dimension of **C** matrix, and its faster convergence and less demand of memory.

3.5 Reconstruction with Equipotential – Projection Algorithm

In this section, the algorithm proposed in 1999 by Eyüboglu US patent [8] and applied to real data by Özdemir [25], is extended. In this case, it can reconstruct a relative conductivity distribution in a two dimensional slice without any potential measurement. In order to obtain the true distribution, the potential at one element on the boundary must be known.

3.5.1 Algorithm

The current density distribution $\vec{J}$ is obtained using MRI from the magnetic flux density distribution, as described in Section 2.4, while current is injected to the subject through electrodes attached to its boundary. Equipotential lines inside the subject can be determined by calculating the orthogonal lines to the current density $\vec{J}$ paths.

At this point, assuming that the conductivity is uniform and known for a column of the FOV, it is possible to calculate by Ohm's law the gradient of the potential for every element in that column.

$$\nabla f = -\frac{\vec{J}}{s} \tag{3.38}$$

The potential distribution f in the column is obtained by integration of this gradient ∇f. If a voltage measurement is performed on this boundary column, the potential values will be true and, therefore, the final conductivity distribution will be absolute. If no voltage is measured, on the contrary, a relative conductivity distribution will result.

Once the potential is calculated in the column, it is projected throughout the FOV by using the equipotential lines. Then, the gradient of the potential distribution

∇f in the whole FOV is calculated. Finally, using again Ohm's law, Equation (3.38), the conductivity distribution is found.

Note that if the conductivity of the column is known, the reconstructed conductivity values will be true conductivities.

3.5.2 Implementation

In this section, some aspects about the implementation of the algorithm are explained.

The gradients are calculated by the Sobel operators, given in Equation (3.16) and Equation (3.17).

The equipotential lines are found by using the procedure described previously in Section 3.2.1.1. Once they are obtained, the potential values at the boundary are projected inside of the domain following these paths. Thus, the potential assigned to each pixel is a weighted average of all the potential values that the crossing equipotential lines carry and their length within the pixel. In a more formal manner, the potential for the i^{th} pixel, f_i, crossed by N_{eqL} equipotential lines is calculated as:

$$f_i = \frac{\sum_{j=1}^{N_{eqL}} l_j f_{eqL_j}}{\sum_{j=1}^{N_{eqL}} l_j}, \tag{3.39}$$

where f_{eqL_j} is the potential which the j^{th} equipotential line inside the pixel carries, and l_j is its length within the pixel.

3.6 Reconstruction with J-substitution Algorithm

Kwon *et al* [20] proposed a new static resistivity image reconstruction algorithm, called J-substitution, and presented simulation results in 2002. They declared the image reconstruction as a constructive map $\{I, J, V\} \to r$ inside a region Ω within the subject, where I is the injected current, J is the magnitude of the current density and V is the peripheral voltage measurements. They assumed that the magnitude of the internal current density distribution is available from an MRI system, including the supplementary current injections added to the subject.

3.6.1 Problem Definition

Let Ω denote a two-dimensional cross section of an electrically conducting body, with resistivity distribution, denoted by r^*. The resistivity distribution r^* in the region Ω and the voltage V_{r^*} are unknown, but the magnitude of the current density, $\left|\vec{J}^*\right|$, is known by using MRI. Injection currents I through electrodes attached on the boundary $\partial\Omega$ are also included in the given current density image. These injected currents I generate current densities on the boundary $\partial\Omega$, whose inward pointing normal components, denoted by j_I, satisfy the compatibility condition:

$$\int_{\partial\Omega} j_I ds = 0.$$

The inverse problem, then, is to reconstruct the resistivity distribution r^* from the known $\left(I, J^*\right)$ pair data, using the physical laws of electromagnetics.

The nonlinear relation between the resistivity distribution r, and the corresponding potential field V_r is given by the boundary value problem (*BVP*) defined by the following Poisson's relation, together with Neumann boundary conditions:

$$\begin{cases} \nabla\cdot\left(\dfrac{1}{r}\nabla V_r\right)=0 & \text{in}\,\Omega \\ \dfrac{1}{r}\dfrac{\partial V_r}{\partial n}=j_I & \text{on}\,\partial\Omega, \end{cases} \tag{3.40}$$

where j_I is the current density at the boundary $\partial\Omega$ and n denotes the unit outward normal vector at the boundary $\partial\Omega$. The term ∇V_r can be uniquely determined by the resistivity r and the boundary current density j_I, induced by I [13]. Here, I is identical to the injection current used for measuring J^*.

When the resistivity distribution is equal to the reconstructed one, i.e. $r = r^*$, the inverse problem can be reduced to the nonlinear Neumann boundary value problem shown in (3.41).

$$\begin{cases} \nabla\cdot\left(\dfrac{J^*}{\left|\nabla V_{r^*}\right|}\nabla V_{r^*}\right)=0 & \text{in}\,\Omega \\ \dfrac{J^*}{\left|\nabla V_{r^*}\right|}\dfrac{dV_{r^*}}{dn}=j_I & \text{on}\,\partial\Omega, \end{cases} \tag{3.41}$$

where the term $1/r^*$ in (3.40) has been substituted by $\vec{J}^*/\left|\nabla V_{r^*}\right|$, since

$$\vec{J}^* = -\frac{1}{r^*}\nabla V_{r^*}. \tag{3.42}$$

Obtaining an image of r^* implies to find a constructive map $\left\{I, J^*\right\} \rightarrow r^*$ from the nonlinear equation (3.41). In order to solve this problem and find a correct solution for r^*, Kwon *et al* developed the following iterative scheme.

3.6.2 Algorithm

In their iterative algorithm, they minimize the cost function $\Phi(r)$, such that:

$$\Phi(r) := \int_{\Omega} \left| J^{*}(\vec{r}) - \frac{1}{r(\vec{r})} E_{r}(\vec{r}) \right|^{2} d\vec{r}\,, \tag{3.43}$$

where $J^{*}(\vec{r})$ is the magnitude of the observed interior current density and $E_{r}(\vec{r}) := \left|\nabla V_{r}(\vec{r})\right|$ is the magnitude of the calculated electric field intensity obtained by solving (3.41) for a given r.

They also established that if at least two currents, I^{1} and I^{2} satisfying the following condition:

$$\left|J^{1} \times J^{2}\right| \neq 0 \tag{3.44}$$

are applied, together with a single voltage measurement, the true conductivity image can be reconstructed.

In this thesis, two opposite orthogonal pairs of electrodes are used. Hence, two current patterns are applied.

Let I^{1} and I^{2} be the two currents injected via two pairs of electrodes. Then, two sets of current density data, $J^{1} = \left|\vec{J}^{1}\right|$ and $J^{2} = \left|\vec{J}^{2}\right|$, induced by I^{1} and I^{2}, respectively, are used to image the resistivity distribution. The position of the electrodes makes J^{1} and J^{2} satisfy the condition (3.44).

The J-substitution reconstruction algorithm solves the nonlinear problem described in (3.41), determining r^{*} from two pairs of data $\left(I^{q}, J^{q}\right)$, where $q = 1,2$ is the injection pattern number. The steps of this iterative algorithm are the following:

- Initial guess: For the initial guess, a homogeneous resistivity r^0 is chosen. For example, $r^0 = 1$.

- Forward solver: For a given resistivity r^{2p+q}, where $q = 1,2$ indicates the injection pattern and $p = 0,1,2,\ldots$ the iteration number, the forward problem is given by

$$\begin{cases} \nabla \cdot \left(\dfrac{1}{r^{2p+q}} \nabla V_p^q \right) = 0 \quad \text{in}\,\Omega \\ \dfrac{1}{r^{2p+q}} \dfrac{dV_p^q}{dn} = j_{I^q} \quad \text{on}\, \partial\Omega \text{ and } \displaystyle\int_{\partial\Omega} V_p^q ds = 0. \end{cases} \tag{3.45}$$

  In this implementation, the Cell-Centered Finite Difference Method [19] has been used, similarly as [20]. Implementation of this method was described in the Section 2.2.3.

- Update r^{2p+q+1}. Since r and ar, where a is a positive constant, will induce the same current density distribution J, but the corresponding voltages are actually scaled by a, the absolute resistivity value needs to be calculated by updating the resistivity using a voltage measurement, as follows:

$$r^{2p+q+1} := \frac{|\nabla V_p^q|}{J^q} \frac{f_{r^*}^q}{f_{r^{2p+q}}^q}, \tag{3.46}$$

  where $f_{r^*}^q$ is the measured voltage difference between two current injection electrodes for the injection current I^q, and $f_{r^{2p+q}}^q$ is the calculated voltage difference when the resistivity distribution is given by computed r^{2p+q}.

- If $\left| r^{2p+q+1} - r^{2p+q} \right| < e$, for a precision error e, stop. Otherwise, go back to Step 2) with $q = q+1$ when $q = 1$, or with $p = p+1$ and $q = 1$ if $q = 2$, where q is the injection pattern and p is the iteration number.

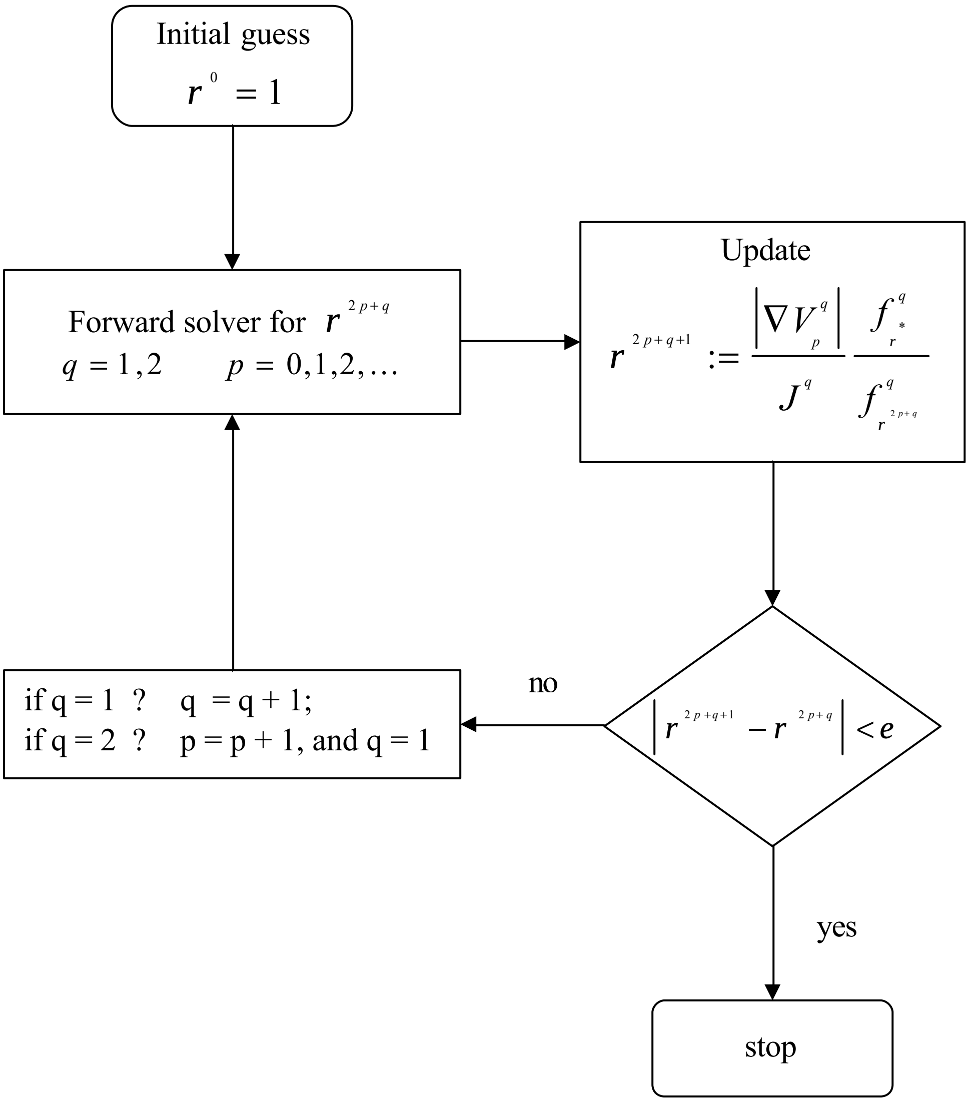
Initial guess
$r^0 = 1$
Forward solver for r^{2p+q}
$q = 1,2 \quad p = 0,1,2,\ldots$
Update
$r^{2p+q+1} := \frac{\left|\nabla V_p^q\right|}{J^q} \frac{f_{r^*}^q}{f_{r^{2p+q}}^q}$
$\left|r^{2p+q+1} - r^{2p+q}\right| < e$
no
if q = 1 ? q = q + 1;
if q = 2 ? p = p + 1, and q = 1
yes
stop

Figure 3.7: Flowchart for J-substitution algorithm

CHAPTER 4

MAGNETIC FLUX DENSITY BASED RECONSTRUCTION ALGORITHM

4.1 Introduction

The harmonic B_z reconstruction algorithm studied next belongs to the second family of algorithms described in the Section 2.4.3.

Seo *et al* [30] in 2003 proposed a new algorithm, where one single component of the induced magnetic flux density, B_z, is measured using an MRI scanner without rotating the object. It is based on the computation of $\nabla^2 B_z$ as shown previously in (2.64), so the noisy B_z is differentiated twice.

Oh *et al* [22], also in 2003, improves this technique with the harmonic B_z algorithm. Here, they use a layer potential technique [16] in two dimensions to recover s from ∇s, instead of line integrals, as Seo *et al* [30] suggested firstly, since they tend to accumulate errors.

4.2 Problem Definition

Oh *et al* [22] places a subject Ω into an MRI scanner, while z surface electrodes are attached on its boundary in order to inject current. Each current injection pattern can be performed by using two of those electrodes. Therefore, the possible number of different injection patterns using z electrodes is $N = z(z-1)/2$, [22]. Let the injection current between the j^{th} pair of electrodes be I^j for $j = 1,\ldots,N$. This current produces a current density $\vec{J}^j = \left(J_x^j, J_y^j, J_z^j\right)$ inside the subject. The presence of the internal current density $\vec{J}^j$ and the current I^j in the lead wires generate a magnetic flux density $\vec{B}^j = \left(B_x^j, B_y^j, B_z^j\right)$, so that $\nabla \times \vec{B}^j = m_0 \vec{J}^j$ holds inside the electrically conducting subject. This induced magnetic flux density causes an increment in the MR phase image, proportional to the *B* component in the direction parallel to the main magnetic field. If this is placed in *z*-direction, the B_z^j components, from $j = 1,\ldots,N$, are assumed to have been obtained from the corresponding MR phase images of the subject.

The subject has an isotropic conductivity distribution s , such that $0 < s < \infty$. Let u^j be the voltage due to the injection current I^j for $j = 1,\ldots,N$. Since s is approximately independent of injection currents, each u^j is a solution of the following Neumann boundary problem:

$$\begin{cases} \nabla \cdot \left(s \nabla u^j \right) = 0 & \text{in } \Omega \\ -s \nabla u^j \cdot \hat{n} = g^j & \text{on } \partial\Omega, \end{cases} \tag{4.1}$$

where $\hat{n}$ is the outward unit normal vector and g^j is the normal component of current density on the boundary $\partial\Omega$ for the injection current I^j . Across a current injection electrode z ,

$$\int_z g^j ds = \pm I^j ,$$

where the sign depends on the direction of current, and g^j is zero on the regions of the boundary which are not in contact with the current injection electrodes used for the j^{th} injection pattern.

If the conductivity distribution s , applied current I^j and electrode configuration are given, the boundary problem (4.1) can be solved for u^j by using numerical methods, such as the finite element method (FEM). But, for this algorithm, the cell-centered finite difference method, explained in the Section 2.2.3, is used.

From the z-component of the relation of $\nabla^2\vec{B} = -m_0\nabla u \times \nabla s$ observed by [27], and previously introduced in (2.64), the expression (4.2) can be obtained for each position inside the subject and each injection pattern $j = 1,\ldots,N$.

$$\frac{1}{m_0}\nabla^2 B_z^j = \left(\frac{\partial s}{\partial x},\frac{\partial s}{\partial y}\right)\left(\frac{\partial u^j}{\partial y},-\frac{\partial u^j}{\partial x}\right) \qquad j = 1,\ldots,N . \tag{4.2}$$

Using a matrix notation, (4.2) can be written as:

$$\mathbf{U}\,\mathbf{s} = \mathbf{b}, \tag{4.3}$$

where

$$\mathbf{U} = \begin{bmatrix} \frac{\partial u^1}{\partial y} & -\frac{\partial u^1}{\partial x} \\ \vdots & \vdots \\ \frac{\partial u^N}{\partial y} & -\frac{\partial u^N}{\partial x} \end{bmatrix} \qquad \mathbf{s} = \begin{bmatrix} \frac{\partial s}{\partial x} \\ \frac{\partial s}{\partial y} \end{bmatrix} \quad \text{and} \quad \mathbf{b} = \frac{1}{m_0}\begin{bmatrix} \nabla^2 B_z^1 \\ \vdots \\ \nabla^2 B_z^N \end{bmatrix}. \tag{4.4}$$

In this implementation, two injection currents are used ($N = 2$).

In order to solve (4.3), **U** must be invertible, that is, the determinant of **U** must be non-zero. The two current densities $\vec{J}^1$ and $\vec{J}^2$ must be chosen so that I^1 and I^2 satisfy:

$$J_x^1 J_y^2 - J_y^1 J_x^2 = 0 . \tag{4.5}$$

This implies that the two current densities are not collinear inside the subject [17], [15].

Using the weighted regularized least square method, **s** vector can be obtained as:

$$\mathbf{s} = \left(\tilde{\mathbf{U}}^T\tilde{\mathbf{U}} + l\,\mathbf{I}\right)^{-1}\tilde{\mathbf{U}}^T\tilde{\mathbf{b}}, \tag{4.6}$$

where:

- $\tilde{\mathbf{U}} = \mathbf{W}\mathbf{U}$,
- $\tilde{\mathbf{U}}^T$ is the transpose of $\tilde{\mathbf{U}}$,

- l is a positive regularization parameter. It is set to $l = \dfrac{1}{\left|\det\left(\tilde{\mathbf{U}}^T\tilde{\mathbf{U}}\right)\right|}$,
- $\mathbf{I}$ is the 2×2 identity matrix,
- $\tilde{\mathbf{b}} = \mathbf{W}\mathbf{b}$,
- $\mathbf{W} = \text{diag}(w_1,\dots,w_N)$ is a $N\times N$ diagonal weight matrix. The weighting factor w_j are set to

  $$w_j = \frac{SNR_j}{\sum_{j=1}^{N} SNR_j}, \tag{4.7}$$

  where SNR_j is the signal-to-noise-ratio (SNR) of the measured B_z^j. This SNR_j should be determined for each position of pixel, although it is difficult in practice to know it. The way to estimate this SNR_j is explained in Section 4.4.

Then, calculating (4.6) for each pixel, the distribution of $\mathbf{s} = \begin{bmatrix} \dfrac{\partial s}{\partial x} & \dfrac{\partial s}{\partial y} \end{bmatrix}^T$ inside the subject is obtained. The next step must be to recover the s distribution.

Now, the imaging slice S is assumed to be lying in the plane $\{z=0\}$ and the conductivity value is 1 at a fixed position $\vec{r}_0 = (x_0, y_0, 0)$ on its boundary ∂S. In order to simplify the following expressions, $\vec{r} = (x,y)$, $\vec{r}\,' = (x',y')$ and $s\,(x,y,0) = s\,(\vec{r})$. Oh *et al* [22] use a layer potential technique in two dimensions in order to compute the s distribution from $\nabla s = \left(\dfrac{\partial s}{\partial x}, \dfrac{\partial s}{\partial y}\right)$, instead of using line integral, as Seo *et al* [30] suggested, since this latter technique accumulates errors. Then,

$$\begin{aligned} s\,(\vec{r}) &= \int_S \nabla^2\Phi(\vec{r}-\vec{r}\,')s\,(\vec{r}\,')d\vec{r}\,' = \\ &= -\int_S \nabla_{\vec{r}\,'}\Phi(\vec{r}-\vec{r}\,')\cdot\nabla s\,(\vec{r}\,')d\vec{r}\,' + \int_{\partial S} \hat{n}_{\vec{r}\,'}\cdot\nabla_{\vec{r}\,'}\Phi(\vec{r}-\vec{r}\,')s\,(\vec{r}\,')dl_{\vec{r}\,'}, \end{aligned} \tag{4.8}$$

where

$$\Phi(\vec{r}-\vec{r}\,')=\frac{1}{2p}\log\left|\vec{r}-\vec{r}\,'\right| \quad \text{and} \quad \nabla_{\vec{r}\,'}\Phi(\vec{r}-\vec{r}\,')=-\frac{1}{2p}\frac{\vec{r}-\vec{r}\,'}{\left|\vec{r}-\vec{r}\,'\right|^{2}}.$$

The second integral in (4.8) can be approximated by [1] for points such that $\vec{r}\in\partial S$

$$\lim_{t\to 0^{+}}\int_{\partial S}\hat{n}_{\vec{r}\,'}\cdot\nabla_{\vec{r}\,'}\Phi(\vec{r}-t\hat{n}_{\vec{r}}-\vec{r}\,')s(\vec{r}\,')dl_{\vec{r}\,'}=\frac{s(\vec{r})}{2}+\int_{\partial S}\hat{n}_{\vec{r}\,'}\cdot\nabla_{\vec{r}\,'}\Phi(\vec{r}-\vec{r}\,')s(\vec{r}\,')dl_{\vec{r}\,'}.$$

Therefore, as $\vec{r}\in S$ approaches the boundary ∂S, the equation (4.8) becomes:

$$\frac{s_{\partial S}(\vec{r})}{2}+\frac{1}{2p}\int_{\partial S}\frac{(\vec{r}-\vec{r}\,')\cdot\hat{n}_{\vec{r}\,'}}{\left|\vec{r}-\vec{r}\,'\right|^{2}}s_{\partial S}(\vec{r}\,')dl_{\vec{r}\,'}=\frac{1}{2p}\int_{S}\frac{(\vec{r}-\vec{r}\,')\cdot\nabla s_{\partial S}(\vec{r}\,')}{\left|\vec{r}-\vec{r}\,'\right|^{2}}d\vec{r}\,', \quad (4.9)$$

where $s_{\partial S}$ denotes the conductivity restricted to the boundary ∂S. Since ∇s is known in S, the right-hand side of (4.9) is known. Then, by [1], the equation (4.9) is guaranteed to be solved and the $s_{\partial S}$ can be found. Now, this $s_{\partial S}$ can be substituted in (4.8), in order to obtain s in S as follows:

$$\begin{aligned} s(\vec{r}) &= -\int_{S}\nabla_{\vec{r}\,'}\Phi(\vec{r}-\vec{r}\,')\cdot\nabla s(\vec{r}\,')d\vec{r}\,'+\int_{\partial S}\hat{n}_{\vec{r}\,'}\cdot\nabla_{\vec{r}\,'}\Phi(\vec{r}-\vec{r}\,')s_{\partial S}(\vec{r}\,')dl_{\vec{r}\,'}= \\ &= \frac{1}{2p}\int_{S}\frac{(\vec{r}-\vec{r}\,')}{\left|\vec{r}-\vec{r}\,'\right|^{2}}\nabla s(\vec{r}\,')d\vec{r}\,'-\frac{1}{2p}\int_{\partial S}\hat{n}_{\vec{r}\,'}\cdot\frac{(\vec{r}-\vec{r}\,')}{\left|\vec{r}-\vec{r}\,'\right|^{2}}s_{\partial S}(\vec{r}\,')dl_{\vec{r}\,'}. \end{aligned} \quad (4.10)$$

This process of solving (4.6) for each pixel, and (4.9) and (4.10) for each imaging slice can be repeated for all imaging slices of interest within the subject, as long as the measured data B_z are available for the slices.

4.3 Algorithm

Since, in order to solve (4.1) the true conductivity distribution s is unknown and in order to obtain this s, the matrix $\mathbf{U}$ with ∇u in (4.3) is needed, as well. Therefore, an iterative algorithm is required.

The injection currents I^{j} are applied through a given pair of electrodes and the z-component of the induced magnetic flux density B_z^{j} is measured for each imaging slice. Also, the boundary voltages $u^j\big|_{\partial S}$ on the electrodes which are not injecting the current I^j are measured.

Then, the $\nabla^2 B_z$ iterative algorithm has the following steps:

Step 1. Let $m = 0$ and assume an initial conductivity distribution s_0.

Step 2. Calculate u^j_{m+1} by solving the following Neumann boundary problem for each $j = 1, \ldots, N$:

$$\begin{cases} \nabla \cdot \left(s_m \nabla u^j_{m+1} \right) = 0 & \text{in } \Omega \\ -s_m \nabla u^j_{m+1} \hat{n} = g^j & \text{on } \partial\Omega. \end{cases} \tag{4.11}$$

Step 3. Calculate s_{m+1} using (4.6), (4.9) and (4.10). Scale s_{m+1} using the measured boundary voltages $u^j\big|_{\partial S}$ and the calculated ones $u^j_{m+1}\big|_{\partial S}$.

Step 4. If $\dfrac{\left\| s_{m+1} - s_m \right\|}{\left\| s_{m+1} \right\|} < e$ for a given tolerance e, continue with Step 5). Otherwise, set $m = (m+1)$ and go back to Step 2).

Step 5. Calculate the current density image as $\vec{J}^j = -s_{m+1} \nabla u^j_M$, where u^j_M is a solution of the boundary value problem in (4.1), with s replaced by s_{m+1}.

4.4 Implementation

In order to compute the **b** matrix, in (4.4) the term $\nabla^2 B_z$ is needed for every pixel. The $\nabla^2 B_z$ at the i^{th} pixel can be calculated with the following three-point difference scheme:

$$\begin{aligned}\nabla^2 B_z(x_i, y_i, z_i) = & \frac{B_z(x_{i+1}, y_i, z_i) - 2B_z(x_i, y_i, z_i) + B_z(x_{i-1}, y_i, z_i)}{(\Delta x)^2} + \\ & + \frac{B_z(x_i, y_{i+1}, z_i) - 2B_z(x_i, y_i, z_i) + B_z(x_i, y_{i-1}, z_i)}{(\Delta y)^2} + \\ & + \frac{B_z(x_i, y_i, z_{i+1}) - 2B_z(x_i, y_i, z_i) + B_z(x_i, y_i, z_{i-1})}{(\Delta z)^2},\end{aligned} \tag{4.12}$$

where Δx, Δy and Δz are the distances between adjacent pixels in the x-, y- and z-directions, respectively.

Consequently, the induced B_z field is needed for every pixel within the slice to be imaged, and in an upper and lower imaginary planes, out of the slice. In the implementation of the algorithm, these two outer planes are placed at 0.83 mm from the real slice.

In this thesis, the forward solver actually provides current density as simulation data. Therefore, for each injection current I^j, the z-component of the induced magnetic flux density B_z^j for $j = 1, \ldots, N$ can be approximated as a matrix equation, by discretizing the Biot-Savart law. This procedure was explained in the Section 2.2.4.

Hence, by using the equation (2.45), B_z can be calculated as:

$$B_z = \mathbf{D_y} J_x - \mathbf{D_x} J_y \,. \tag{4.13}$$

Now, using (4.12), $\nabla^2 B_z$ is obtained for every element in the slice, so the **b** matrix can be calculated and (4.3) can be finally solved.

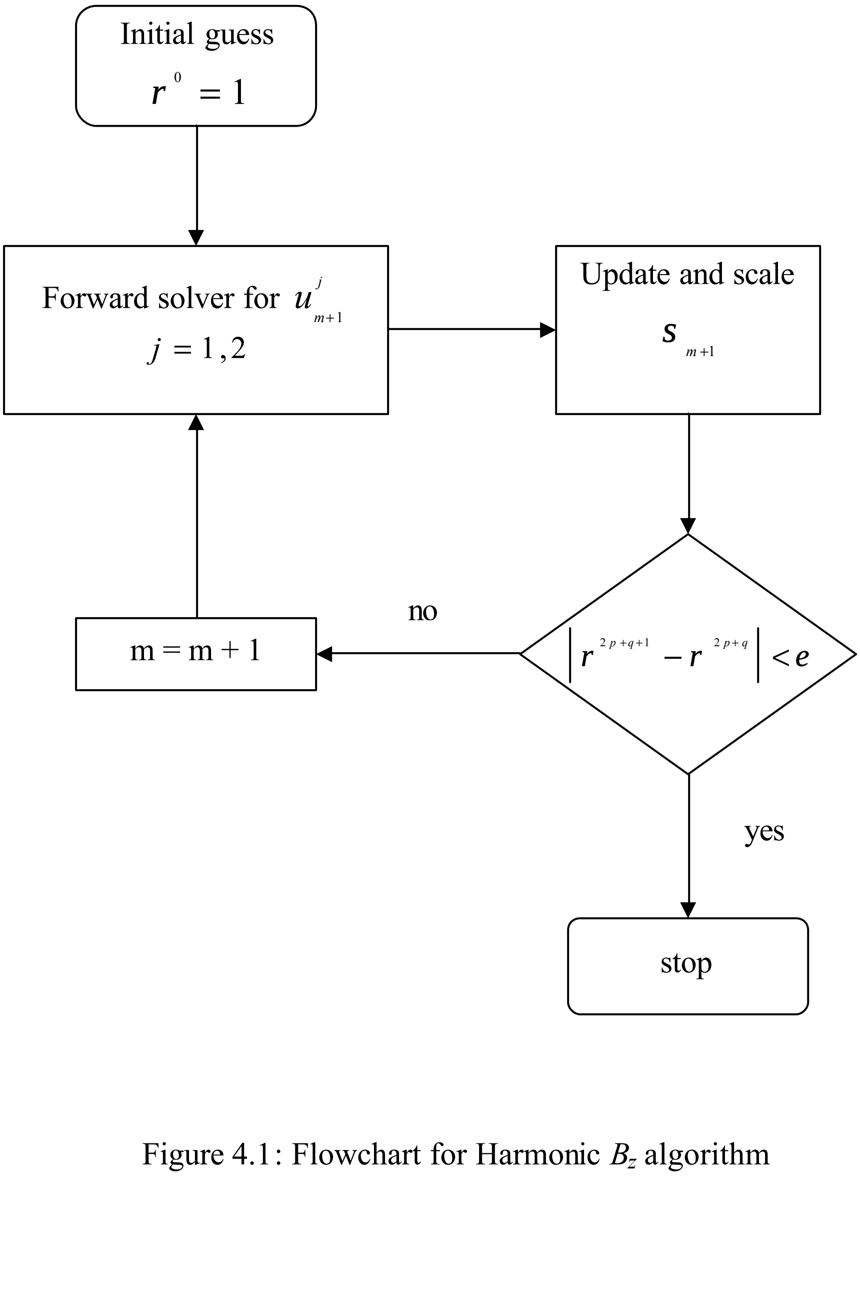

Figure 4.1: Flowchart for Harmonic B_z algorithm

CHAPTER 5

SIMULATION AND COMPARISON

5.1 Introduction

This chapter is reserved for the simulation results and comparison of the reconstruction algorithms described previously. This analysis covers different cases, with and without noise, different techniques for the same algorithm, or different stopping criteria for iterative algorithms.

5.2 Conductivity models

Two different two-dimensional conductivity models have been used to illustrate the performance of the reconstruction methods described in previous chapters. One of them was previously used to collect experimental data, while the other has been defined to provide simulated data to the reconstruction algorithms studied in this thesis.

In order to decide the dimensions of the simulated conductivity model and amount of injected current, several previous studies have been considered. It has been observed that reconstruction algorithms in noise-free cases are not affected by the amount of current applied. The absolute values of the simulated data change but, since the proportions between conductivity, current density and potential are kept, the reconstructed image remains the same. Ider *et al* [15] considered 100 mA for noisy cases and a phantom of $20\times 20\,\text{cm}$. Oh *et al* [22] used 26 mA for an object of $50\times 50\,\text{mm}$. Özbek [24] and Birgül [2] collected measured data in the 0.15 Tesla METU-EE MRI system, using 20 mA for an experimental phantom of 6×6 cm. In order to compare all the reconstruction algorithms under the same conditions and be consistent with the experimental data of [24] and [2], which has been also used as the experimental phantom, the size of the imaging slice has been finally chosen as 6×6 cm, and the total injected current has been established in 20 mA for each injection pattern.

5.2.1 Simulated phantom

Figure 5.1(a) shows the geometry of an electrically conducting phantom with an isotropic and piecewise constant conductivity distribution s. The dimensions of this numerical phantom is 6×6 cm, discretized into 50×50 square elements. Assigned conductivity values for the regions of the phantom are listed in Table 5.1. The background conductivity (3) has been chosen to be 2 S/m, which is close to the average body conductivity. There are two different conductivity perturbations in it: a rectangle (1) and a circle (2). The rectangle is more conductive than the background, with conductivity equal to 4 S/m, while the circle is more resistive, with conductivity set to 1 S/m.

The currents are injected using four constant-current electrodes, covering the whole sides, as shown in Figure 5.1(b). Therefore, two different and orthogonal injection patterns are possible for the two pairs of electrodes. A total injected current of 20 mA has been used for each injection pattern.

Table 5.1: Simulated conductivity model values

Region	Object	Conductivity value (S/m)
1	Rectangle	4
2	Circle	1
3	Background	2

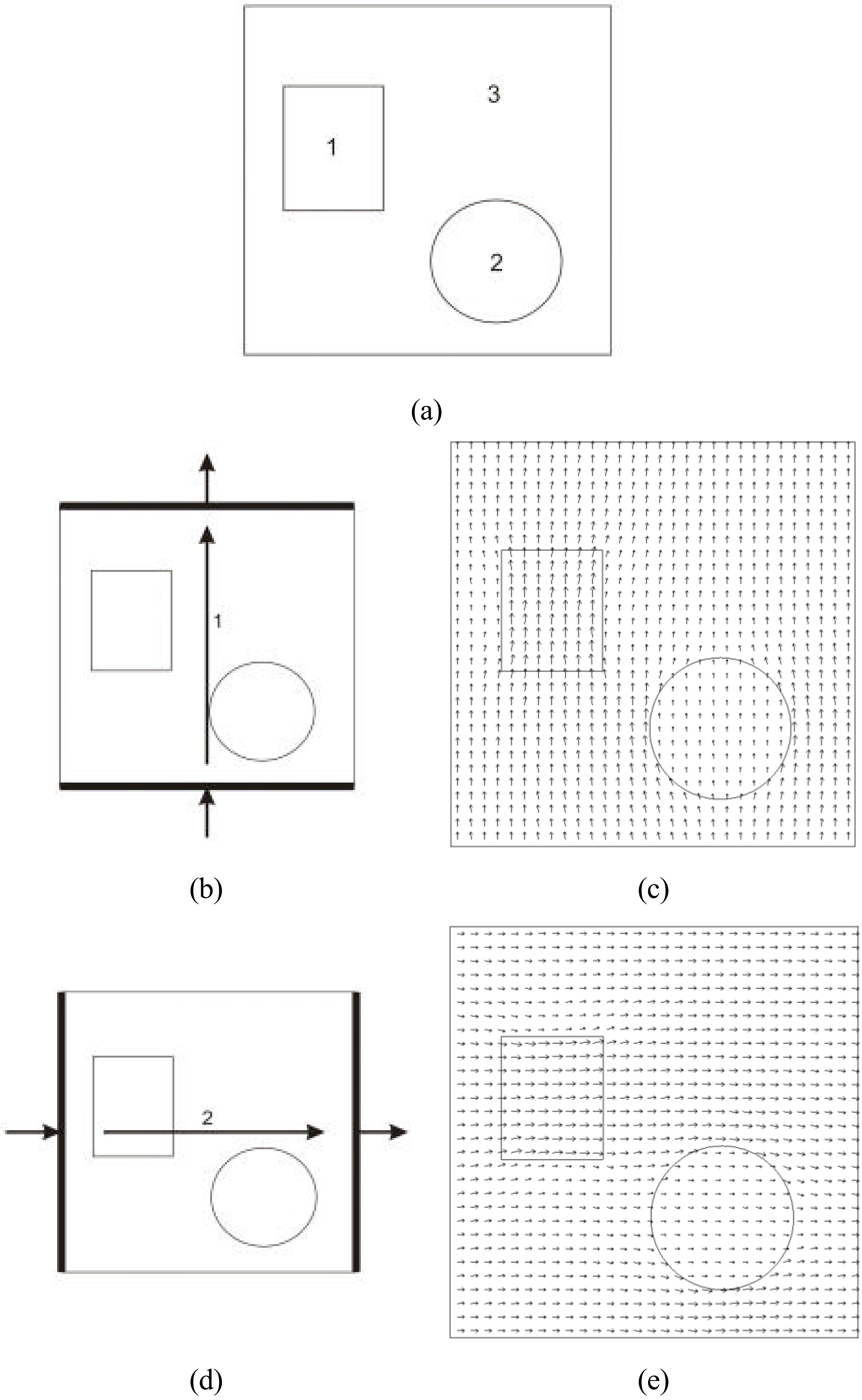

(a)

(b) (c)

(d) (e)

Figure 5.1: Definition for the simulated conductivity model. (a) Regions of different conductivity. The conductivity values are given in Table 5.1. Position of current electrodes for orthogonal injection patterns 1 (b) and 2 (d). Total current density distribution for injection pattern 1 (c) and 2 (e).

5.2.2 Experimental phantom

The geometry of the experimental phantom can be seen in Figure 5.2. This test phantom is $6\times6\times2$ cm, discretized into 30×30 square elements. It is filled with Agar gel, with conductivity 2 S/m. Since the third dimension is small enough compared with the other two dimensions, the applied current is assumed to flow only in the *x-y* plane and the problem can be simplified to a two-dimensional one. A conductor object of $2.5\times2.5\times2$ cm, with conductivity 9 S/m is placed in the center. The currents are injected using four small electrodes, opposite to each other. Thus, two orthogonal injection patters can be performed, with a total injected current of 20 mA for each case.

Table 5.2: Experimental conductivity model values

Region	Object	Conductivity value (S/m)
1	Square	9
2	Background	2

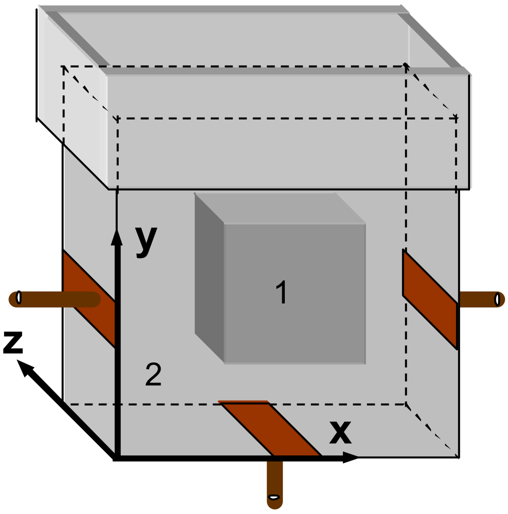

Figure 5.2: Definition for the experimental conductivity model. The regions of different conductivity and electrode positions are shown [24]. The conductivity values are given in Table 5.2.

5.3 Simulation of measurement noise

In order to compare the performance of the algorithms in presence of noise, the random Gaussian noise model explained by Scott *et al* [28], and reviewed in APPENDIX A is used. In their model, the noise is induced as a MR phase error, independent of the magnetic flux density and, therefore, of the injected current. Thus, if the amount of injected current is increased, the induced magnetic flux is increased, so the proportional noise in magnetic flux density is reduced. However, in [15], 10% of the magnitude of each current density component and injection is multiplied by a random number in the range of ±1 and added to the corresponding noise-free current density. But, the model of Scott *et al* [28] is more realistic; since the noise is independent of the direction of the current injection and independent of its magnitude. It only depends on the MRI system where the experiments are carried out. The reconstructed algorithms are tested using different noise levels, corresponding to SNR equal to 60, 30 and 20. For each level, the maximum noise included in the current density data with respect to the maximum value of the noise-free case, is given in Table 5.3.

Table 5.3: Maximum noise level in J_x and J_y with respect to the maximum currents densities for the different noise levels

	Injection pattern 1		Injection pattern 2	
	J_x	J_y	J_x	J_y
SNR 60	14.8%	5.2%	5.1%	19.7%
SNR 30	33.5%	11.5%	11.6%	43.1%
SNR 20	43.6%	16.5%	15.1%	61.9%

One noise experiment is performed for each SNR and the resulting noisy current densities are fed to the algorithms. This ensures that all algorithms run under the same conditions, since different experiments can affect different pixels and provoke different behaviors.

5.4 Error calculation and stopping criteria

In order to evaluate performance of the studied algorithms, error in the reconstructed conductivity is calculated. In practice, the real conductivity is not known *a priori*, but in this thesis, since the algorithms are fed with simulated data, the true conductivity distribution is actually known.

The total error committed at reconstructing the whole image $e_{s\,T}$ is calculated as:

$$e_{s\,T} = \frac{\left\| s_t - s_r \right\|}{\left\| s_t \right\|} \times 100\%, \tag{4.14}$$

where s_t and s_r are the true and reconstructed conductivity distributions, respectively, and $\left\| \cdot \right\|$ is the L_2 norm, defined as:

$$\left\| \vec{a} \right\| = \left(\sum_i a_i^2 \right)^{1/2}, \tag{4.15}$$

where a_i is the i^{th} element of $\vec{a}$.

The conductivity error of a reconstructed region in the image is calculated with Equation (4.14), but restricted to the desired zone, resulting:

$$e_{s\,,region} = \frac{\left\| s_{t,region} - s_{r,region} \right\|}{\left\| s_{t,region} \right\|} \times 100\%, \tag{4.16}$$

where, $s_{t,region}$ and $s_{r,region}$ are the true and reconstructed conductivity distributions for that conductivity region, respectively.

In order to end the iterative algorithms, different types of stopping criteria are defined. In real cases, the true conductivity distribution is unknown. Therefore, a stopping criterion based on the difference $e_{s\,,m}$ between the reconstructed conductivity of two successive iterations is used:

$$e_{s\,,m} = \frac{\left\| s_m - s_{m-1} \right\|}{\left\| s_m \right\|}, \tag{4.17}$$

where m is the iteration number and $\|\cdot\|$ is the L_2 norm previously defined in (4.15). As the iterations run, $e_{s,m}$ decreases monotonically for noise-free cases. Thus, if $e_{s,m} < e$, for a given tolerance e, the algorithm is said to have converged to the actual values of conductivity distribution.

In noisy cases, the convergence function can reach a minimum, but greater than the tolerance e, and increase again. Then, a maximum number of iterations is needed as stopping criteria. Then, the reconstructed conductivity distribution is chosen as the one where the difference between iterations $e_{s,m}$ is minimum.

In case of simulated data, the true distribution is known. Then, running a fixed number of iterations, the convergence function can be studied and the conductivity distribution with minimum total error e_{sT} with respect to the true distribution is chosen.

5.5 Spatial Resolution

Spatial resolution describes the minimum size an object must be to be seen in an image [31]. It also describes the degree of deblurring present in an image. It is often represented by: Point Spread Function (PSF), Line Spread Function (LSF) and edge response, Modulation Transfer Function (MTF) or System Transfer Function (STF).

The PSF contains complete information about the spatial resolution. To express the spatial resolution by a single number, it is possible to ignore the shape of the PSF and simply measure its width. The most common way to specify this is by the Full-Width-at-Half-Maximum (FWHM) value. Unfortunately, this method has two significant drawbacks. First, it does not match other measures of spatial resolution, including the subjective judgment of observers viewing the images. Second, it is usually very difficult to directly measure the PSF.

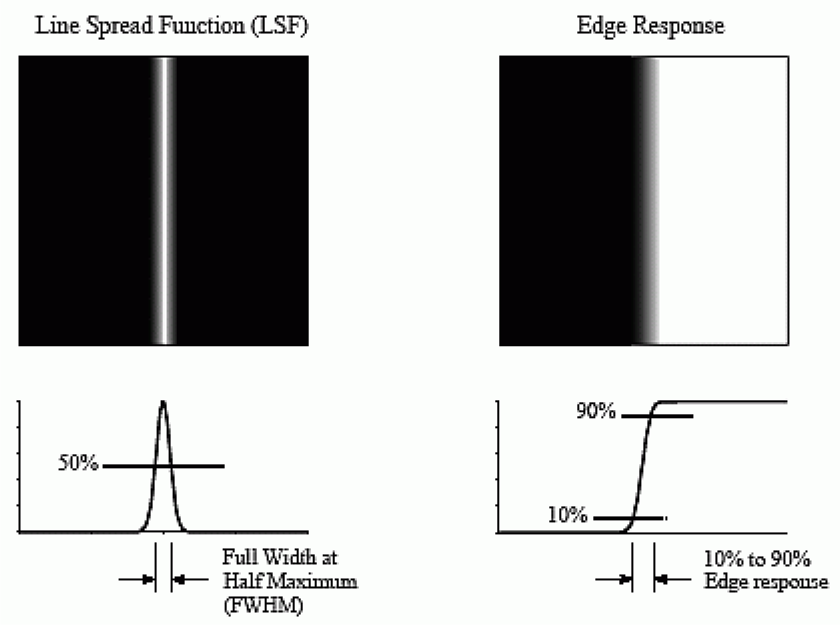

Figure 5.3: Line spread function (LSF) and edge response [31].

As it is shown in Figure 5.3, the LSF is the response of the system to a thin line across the image. Similarly, the edge response is how the system responds to a sharp straight discontinuity, an edge. Since a line is the derivative of an edge, the LSF is the derivative of the edge response. The width of the LSF is usually spread as the FWHM, while the width of the edge response is normally quoted by the 10% to 90% distance.

In this thesis, the Line Spread Function is used in order to quantify the blurring effect of the reconstruction algorithms and different methods of integration. The LSF is measured as the FWHM of the derivative of the edge response at the edges of the rectangle in the phantom.

5.6 Simulation Results for Current Density Based Algorithms

In the following sections, the results for the *Type*-I reconstruction algorithms, explained in chapter 3, and based on current density, are given and discussed.

5.6.1 Reconstruction by Integration along Equipotential Lines

In this section, the resulting conductivity images using the reconstruction method described in Section 3.2 are shown. The effects of the different integration methods described in Section 3.2.1.2 and different noise levels are also considered.

Firstly, the equipotential lines are calculated starting from the left edge of the phantom, using the algorithm explained previously in Section 3.2.1.1. For this purpose, the simulated current density, corresponding to the vertical injection pattern, labeled as (1) in Figure 5.1(d) is used. Figure 5.4(b), shows the calculated equipotential lines, when two of them begin from every pixel at the left boundary. It can be seen that the equipotential lines get closer to each other around the contours of the objects, while the upper and lower parts of the image result uncovered. At an interface between two regions of different conductivity, the currents tend to enter the more conductive one, but avoid the more isolator one. Then, since the equipotential lines are orthogonal to the current streamlines at every point, the equipotential lines bend, coming very close to each other, accumulating around the circle contour and at the upper and lower edge of the rectangle. Another side effect appears due to this reason. The current density is assumed to be constant within a pixel. But, the pixel size may be too large in those accumulation areas and contain, however, more than one current streamline. This provokes that, during the calculation of the equipotential lines, some paths cross others. This behavior is not valid, so the equipotential lines involved are detected and removed. In the noise-free simulations carried out with this phantom, around 2% of the total equipotential lines are invalid for this reason. They are not taken into consideration for the integration in the reconstruction, but provoke small errors, due to the information loss.

After the equipotential lines are found, current density derivatives are integrated along these paths. If more than one equipotential line crosses a pixel, the $\Re$ value assigned to the pixel is an average between the values calculated for each equipotential line. The resistivity of the left column is assumed to be known.

The reconstructed images for the noise-free case can be seen in Figure 5.4, while the errors committed at reconstructing each conductivity region and the total image can be seen in Table 5.4.

Table 5.4: Errors in reconstruction along equipotential lines

Reconstructed Conductivity	**Circle ($e_{s\ Circ}$) (%)**	**Rectangle ($e_{s\ Rect}$) (%)**	**Background ($e_{s\ Bkcg}$) (%)**	**Total error (%)**
Trapezoidal integration method				
Noise free				
3 equipot. lines	17.90	12.97	9.91	11.75
10 equipot. lines	17.69	12.15	9.74	11.36
Noisy cases. 10 equipot. lines				
SNR 60	18.38	14.92	10.14	12.59
SNR 30	28.50	17.36	19.09	20.18
SNR 20	25.23	25.65	20.12	23.30
Taylor Expansion method				
Noise free				
3 equipot. lines	20.90	13.25	10.38	12.28
10 equipot. lines	20.61	12.54	10.23	11.94
Noisy cases. 10 equipot. lines				
SNR 60	20.74	15.26	10.47	13.02
SNR 30	28.67	17.53	19.31	20.40
SNR 20	25.84	25.44	20.37	23.43

The blurring effect of the different integration methods is studied next. As it was explained previously in Section 5.5, the measurement of the spatial resolution by calculating the width of the LSF at FWHM at one edge inside the image can provide an idea of the degree of blurring of the reconstructed images. Figure 5.5 shows the horizontal profile and LSF images for a line crossing an edge of the rectangle. The LSF widths for both trapezoidal integration method and Taylor expansion method are given in Table 5.5.

Table 5.5: FWHM of LSF for reconstruction along equipotential lines

Reconstructed Conductivity	**Trapezoidal integration FWHM** (cm)	**Taylor Expansion FWHM** (cm)
Noise free 10 equipot. Lines	0.297	0.254
Noisy case. SNR 20 10 equipot. lines	0.200	0.230

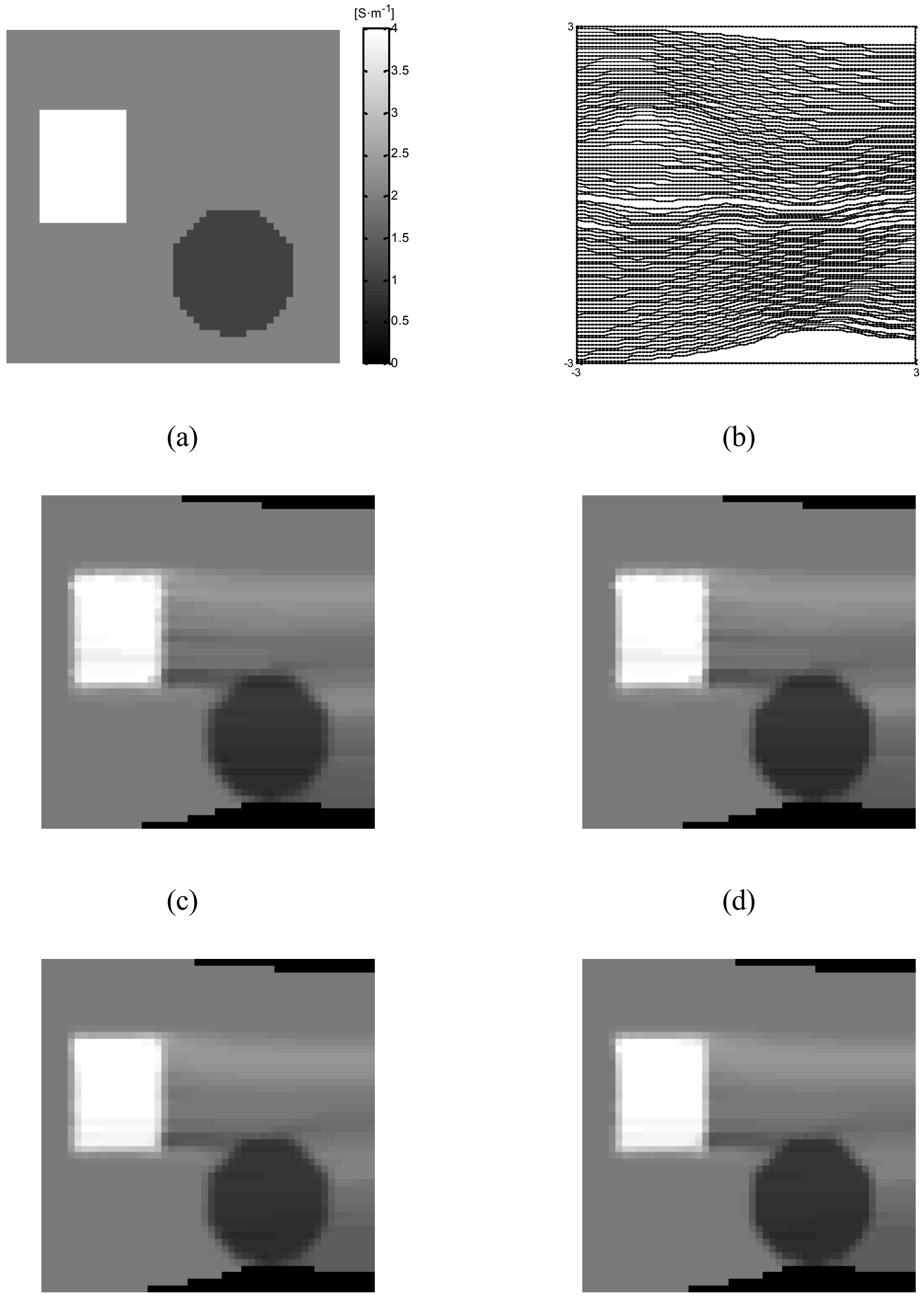

(a) (b)

(c) (d)

(e) (f)

Figure 5.4: Reconstruction by integration along equipotential lines. Noise-free cases. All the figures have the same gray scale. (a) True conductivity distribution. (b) Equipotential lines. 2 equipotential lines start for each pixel at the left edge. Reconstructed conductivity images, where 3 equipotential lines per pixel start from left boundary, using (c) Trapezoidal integration or (d) Taylor Expansion. Reconstructed conductivity images with 10 equipotential lines per pixel, using (e) Trapezoidal integration method or (f) Taylor Expansion.

As expected, the trapezoidal integration method produces wider LSF and, therefore, more blurred contours. This is because it takes into consideration the current density derivatives of the previous and current pixel. The Taylor expansion method produces sharper objects, since it only integrates the current density derivatives of the current pixel. As a disadvantage, the committed error in the latter case is slightly larger.

In the reconstructed images, some horizontal artifacts in the direction of integration, mainly horizontally, along the equipotential paths are due to the accumulation of errors, typical of the integration techniques. This effect is more important when less equipotential lines per pixel are started from the left boundary. The pixels which are not crossed by any equipotential lines are assigned to have zero conductivity and appear as the darkest regions. They are not considered for the error calculation. This effect could be minimized tracing equipotential lines from the right boundary, as well. But, even in those conditions, the circle is too far from the lower electrode, and a big area under it, with very little current, still remains. It would be necessary to include more injection patterns to fill with information those areas, like horizontal or diagonal ones.

Afterwards, different noise levels have been tested, equivalent to SNR equal to 60, 30 and 20. For the same noisy experiment, the image has been reconstructed by both integration methods and compared. The conductivity errors are given in Table 5.4, while the reconstructed images for trapezoidal integration method can be seen in Figure 5.7. In all cases, ten equipotential lines are started from the left column of the image. The blurring effects of the different integration methods are studied in Figure 5.6, where the horizontal profile and LSF images for a line crossing an edge of the rectangle are given, for case of SNR equal to 20.

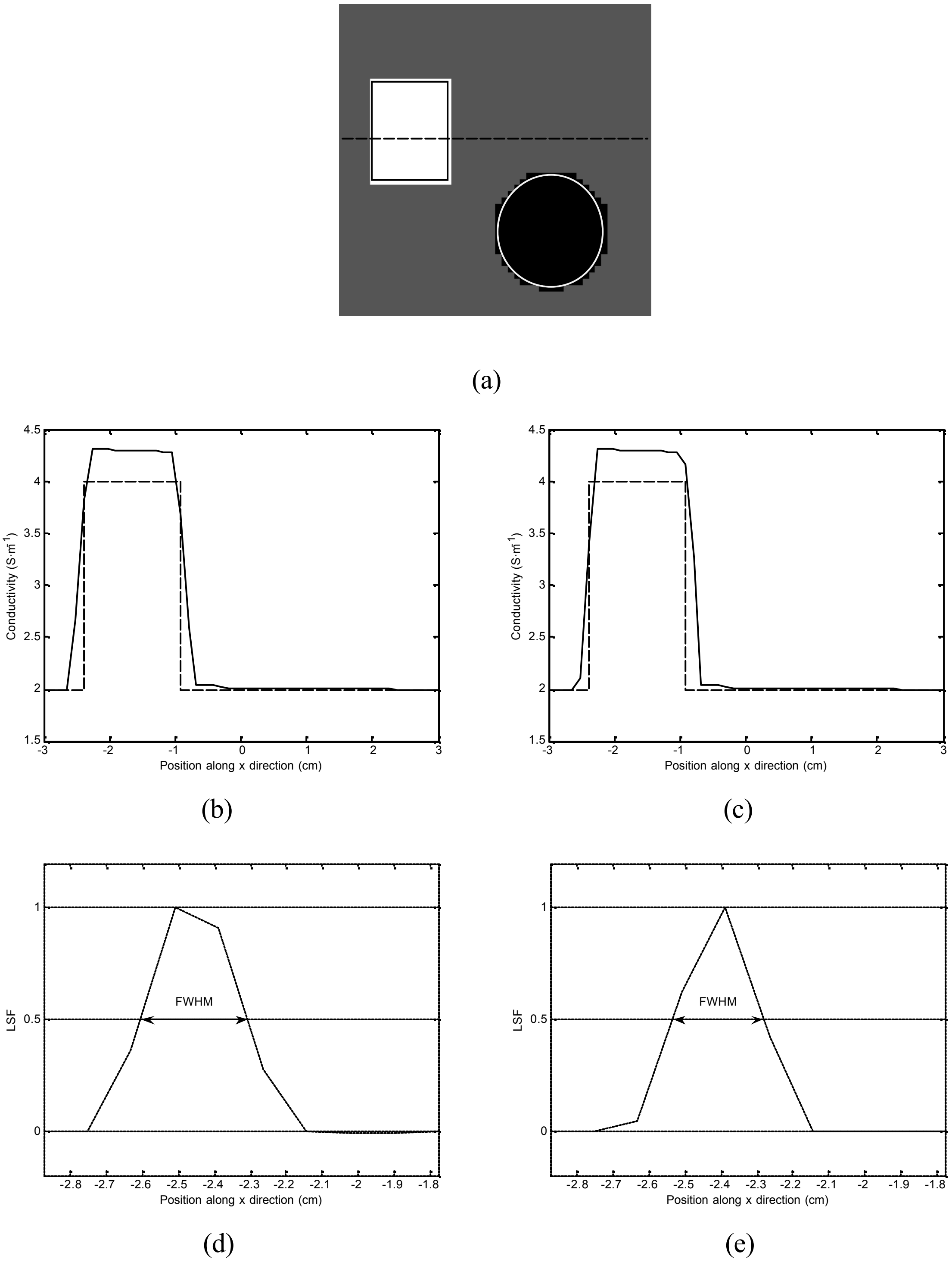

(a)

(b)

(c)

(d)

(e)

Figure 5.5: Profile and LSF images for reconstruction by integration along equipotential lines. Noise-free cases. 10 equipotential lines per pixel. (a) True distribution. The dashed line gives the definition of the profile images. (b) Profile image for trapezoidal integration. (c) Profile image for Taylor expansion method. (d) LSF for trapezoidal integration. (e) LSF for Taylor expansion.

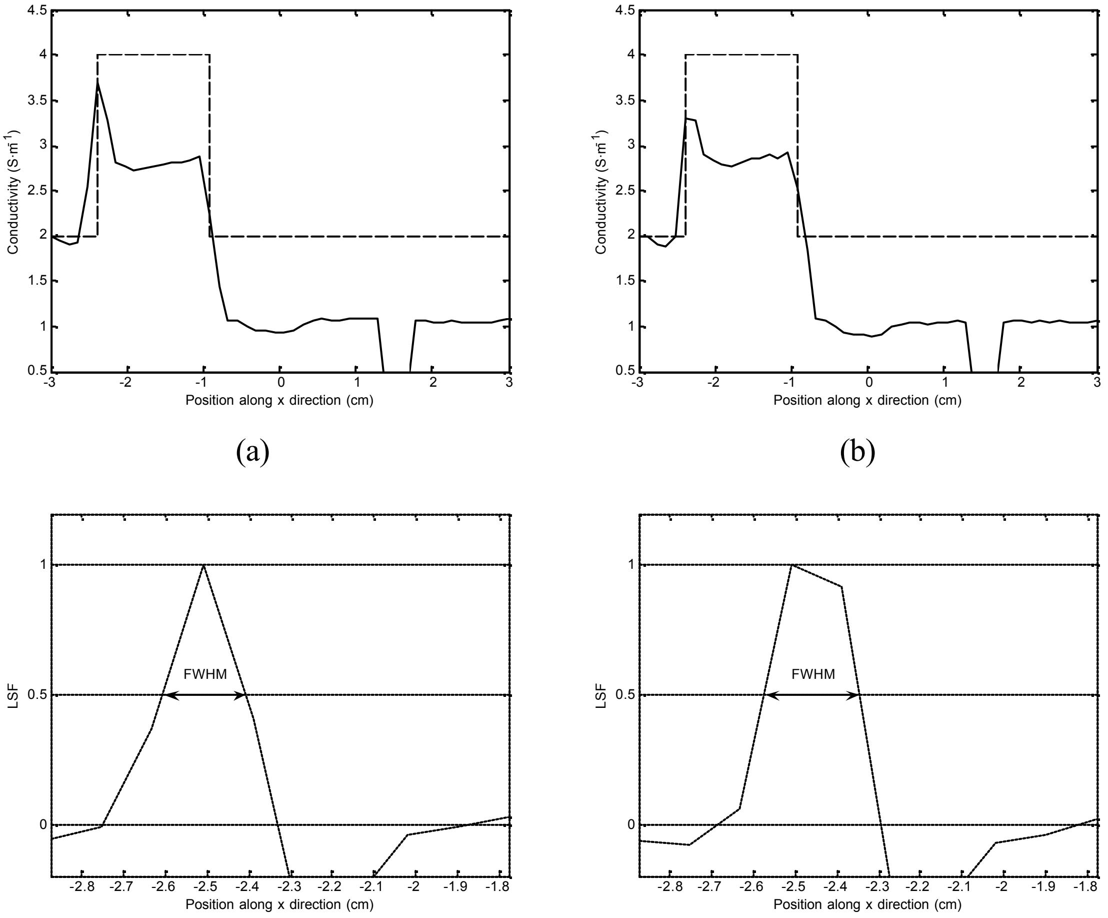

(a)

(b)

(c)

(d)

Figure 5.6: Profile and LSF images for reconstruction by integration along equipotential lines. SNR 20. 10 equipotential lines per pixel. The definition of the profile images is the same as in Figure 5.3(a). (a) Profile image for trapezoidal integration. (b) Profile image for Taylor expansion method. (c) LSF for trapezoidal integration. (e) LSF for Taylor expansion.

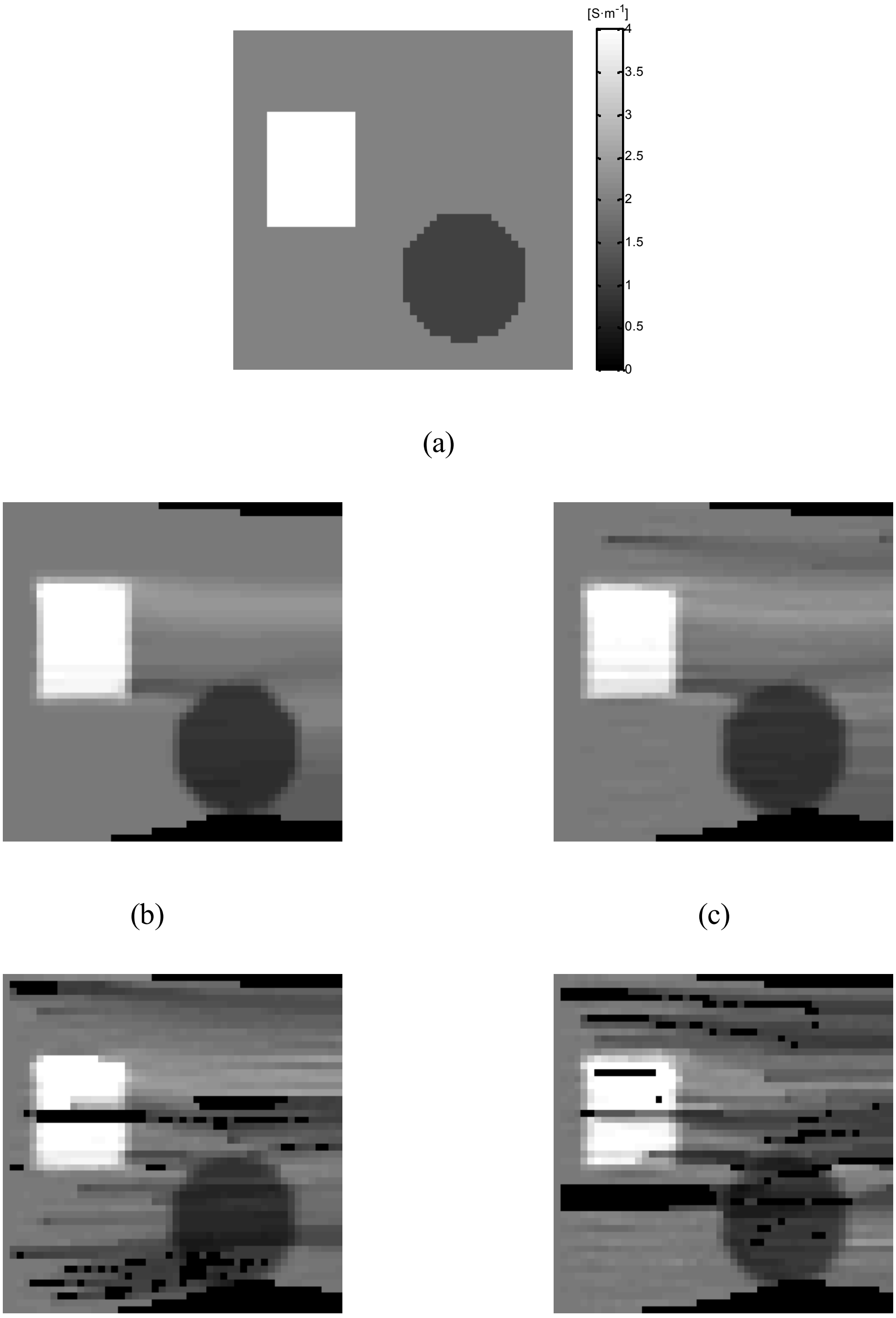

(a)

(b)

(c)

(d)

(e)

Figure 5.7: Reconstruction by integration along equipotential lines. Comparison between noise-free and noisy cases. 10 equipotential lines start from each pixel at left edge. All the figures have the same gray scale. (a) True conductivity distribution. Reconstructed conductivity images using trapezoidal integration for the (b) noise-free case. Same conditions and integration method for noisy cases, with (c) SNR 60 (d) SNR 30 and (e) SNR 20.

It is observed that at the lowest SNR, the reconstructed image becomes very affected by the noise, but still can be reconstructed. When the SNR is so low, an important number of equipotential lines become invalid, because of the reasons explained above. This lack of information can be seen as the darkest pixels, with conductivity set to zero. In some experiments, since the error is random, the blank areas may be very close to each other, making the reconstruction around quite inaccurate. And, since these inexact values are integrated along the equipotential paths, this inaccuracy is spread along the pixels which the equipotential line crosses. Since the procedure to trace the equipotential paths is so sensitive to noise, it has been necessary to repeat several times the noise experiment for the case of SNR equal to 20, until enough equipotential lines could cover the field of view (FOV) and produce an image. Then, this noisy current density is fed to the rest of algorithms to keep the same noisy conditions for SNR 20.

Note that the main reason for the small error values at low SNR is that the pixels which are not covered by the equipotential lines are actually not taken into consideration for this calculation. But, these dark pixels in the image distort its appearance and reduce its practical usage.

Summarizing, this reconstruction method can reconstruct the absolute values of conductivity if $\Re$ is known for at least one point on each equipotential line. The conductivity error is smaller if more equipotential lines are initiated from the edges. The Taylor expansion integration method reconstructs sharper objects, but with slightly larger error. Finally, this method can reconstruct images with a minimum SNR of 20.

5.6.2 Reconstruction by Integration along Cartesian Grid Lines

In this section, the algorithm explained in Section 3.3 is studied. The effect of the different integration methods described in Section 3.2.1.2 is considered, as well as the direction in which this integration is performed. In [15], only results for the integration along horizontal lines using the trapezoidal method are given.

First of all, the gradient of the logarithmic resistivity $\Re$, $[\partial\Re/\partial x \quad \partial\Re/\partial y]^T$, is calculated using Equation (3.18). Then, assuming that the value of R is known at the lower-left corner, the gradient $\partial\Re/\partial y$ is integrated upwards in order to obtain $\Re$ along the left boundary. Once this is known, from those pixels, integrating horizontally $\partial\Re/\partial x$ from left to right, the rest of the pixels of the image are calculated. The result can be seen in Figure 5.8(a), where the integration is done by the trapezoidal method, or (b) if it is performed by Taylor expansion. As it was stated previously, t is seen that, in the latter case, the edges of the objects look sharper, particularly the ones in the direction of integration. This is because by using Taylor, only the gradient of $\Re$ of the current pixel is involved. However, in the trapezoidal method, the average of the derivatives of $\Re$ of the current and former pixel is used. Moreover, some horizontal lines are noticeable in the direction of integration. This is because the integration technique accumulates errors, especially when an abrupt change in gradient occurs, for example at the object edges.

Similarly, in Figure 5.8(c) and (d), the integration of $\partial\Re/\partial y$ is done vertically, from up to down, while the whole first row is assumed to be known. Again, it is noticeable the blurred and smoother transitions at the object edges for the Trapezoidal method, and the vertical integration bias effect in both integration methods.

In order to try to minimize all these effects, an average between the horizontal and vertically integrated images has been done. The resulting images are displayed in Figure 5.8(e) and (f). As expected, many of the effects have been counteracted.

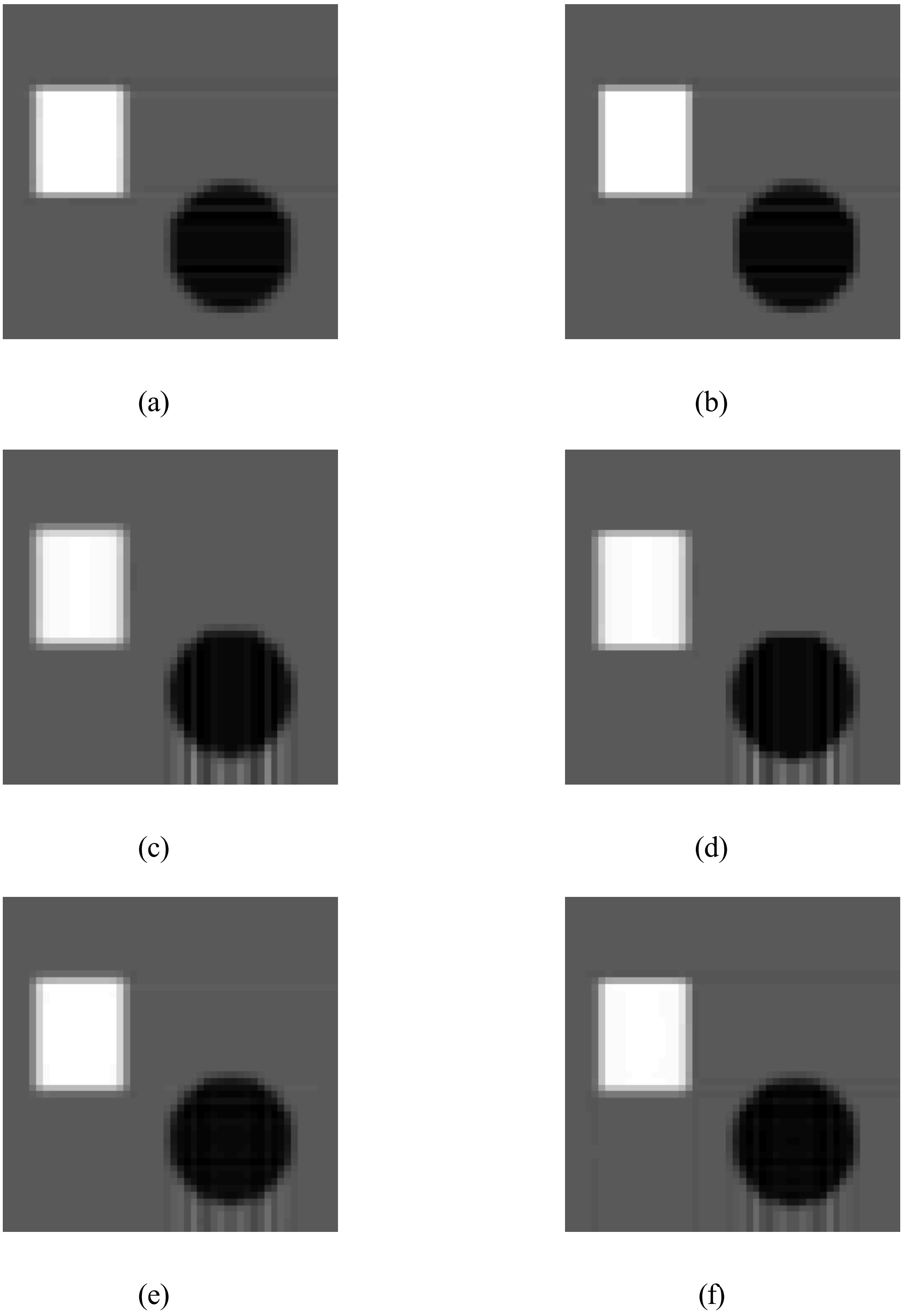

(a) (b) (c) (d) (e) (f)

Figure 5.8: Reconstruction along cartesian grid lines. Noise-free cases. Comparison of different integration methods. All the figures have the same gray scale. Reconstructed conductivity images using (a) trapezoidal integration method along horizontal lines; (b) Taylor expansion along horizontal lines; (c) trapezoidal integration along vertical lines; (d) Taylor expansion along vertical lines; (e) average of (a) and (c) cases; (f) average of (b) and (d) cases.

Table 5.6: Errors in reconstruction along cartesian grid lines

Reconstructed Conductivity	**Circle** ($e_{s\,Circ}$) **(%)**	**Rectangle** ($e_{s\,Rect}$) **(%)**	**Background** ($e_{s\,Bkcg}$) **(%)**	**Total error (%)**
	Trapezoidal integration method			
Noise free				
Horizontal	14.46	10.77	3.94	7.23
Vertical	15.01	6.50	5.60	6.60
Average	13.37	8.54	4.35	6.44
Noisy cases				
SNR 60 Average	13.67	8.83	5.48	7.23
SNR 30 Average	15.21	9.32	6.64	8.21
SNR 20 Average	15.61	11.95	7.53	9.74
SNR 10 Average	30.90	28.83	24.54	27.64
	Taylor Expansion method			
Noise free				
Horizontal	17.88	11.58	5.70	8.61
Vertical	17.45	7.41	6.54	7.65
Average	14.52	8.96	4.89	6.96
Noisy cases				
SNR 60 Average	14.55	9.39	5.80	7.67
SNR 30 Average	15.12	10.10	7.11	8.89
SNR 20 Average	17.14	12.81	7.87	10.33
SNR 10 Average	31.79	30.49	24.04	27.83

In Table 5.6 the error values for each case are shown. In Table 5.7, the widths corresponding to the LSF for noise-free and SNR equal to 20 are given. It is seen that the circle is reconstructed slightly better using the trapezoidal integration, due to the blurring effect of this method on its complex boundary. The rectangle is reconstructed better integrating along vertical lines, since for the horizontal case the starting point is the lowest left pixel, which is known. Then, at calculating the left column from that point, the integration accumulates errors, which are later propagated when the values of that column are integrated horizontally. The background minimizes its error using the trapezoidal integration. The larger blurring effect of this method approximates the object contours better, introducing fewer errors in the background pixels. The overall error is lower by averaging between the horizontally and vertically integrated images. As stated in the previous section, the trapezoidal integration method provides lower spatial resolution, since the LSF is wider.

Table 5.7: FWHM of LSF for reconstruction along cartesian grid lines

Reconstructed Conductivity	**Trapezoidal integration FWHM** (cm)	**Taylor Expansion FWHM** (cm)
Noise free. Average	0.309	0.273
SNR 20. Average	0.287	0.254

This algorithm has been tested with the three conventional noise levels: SNR equal to 60, 30, 20, plus an additional 10. For each one, the image has been reconstructed by both integration methods. The conductivity errors were also given in Table 5.6, while the reconstructed images, using trapezoidal integration method and averaging the horizontal and vertical integration cases are displayed in Figure 5.9.

This algorithm is more robust against noise than the previous one, since there are no equipotential lines to be obtained. The integration is simply along horizontal and vertical lines. The error is, in all cases, slightly lower for the trapezoidal integration method, due to its averaging effect. When the noise level is so high, as in the previous algorithm, the total error for the reconstruction depends significantly on the experiment.

Summarizing, only at one single point the logarithmic resistivity needs to be known in order to reconstruct absolute conductivity values. The conductivity error is smaller for trapezoidal integration method, although the contours of the structures look more blurred than with Taylor expansion method. Finally, this algorithm can reconstruct images with SNR equal to 10.

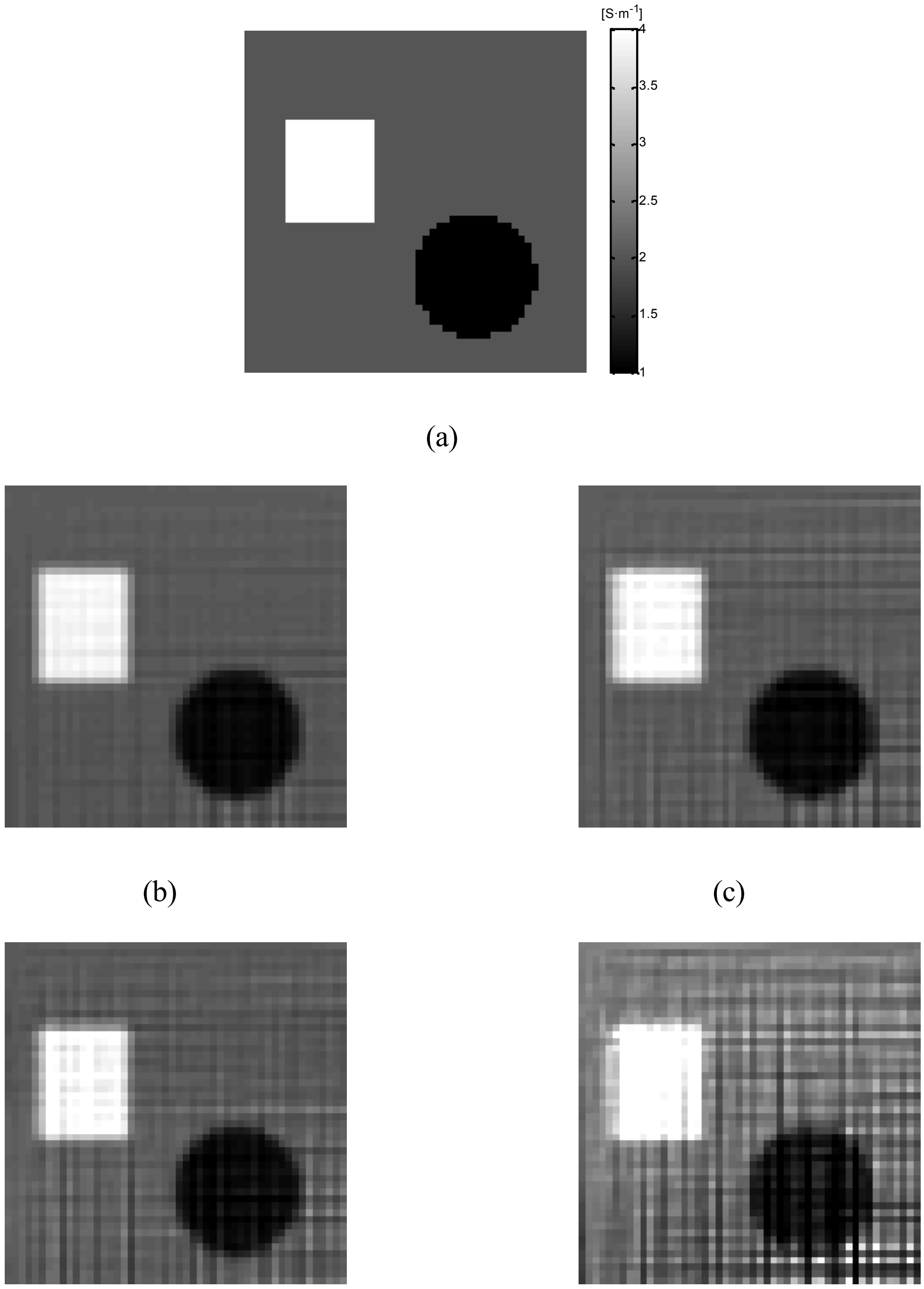

(a)

(b)

(c)

(d)

(e)

Figure 5.9: Reconstruction by integration along cartesian grid lines. All the figures have the same gray scale. (a) True conductivity distribution. Reconstructed conductivity images using trapezoidal integration and averaging between vertical and horizontal integration for (b) SNR 60, (c) SNR 30, (d) SNR 20, and (e) SNR 10.

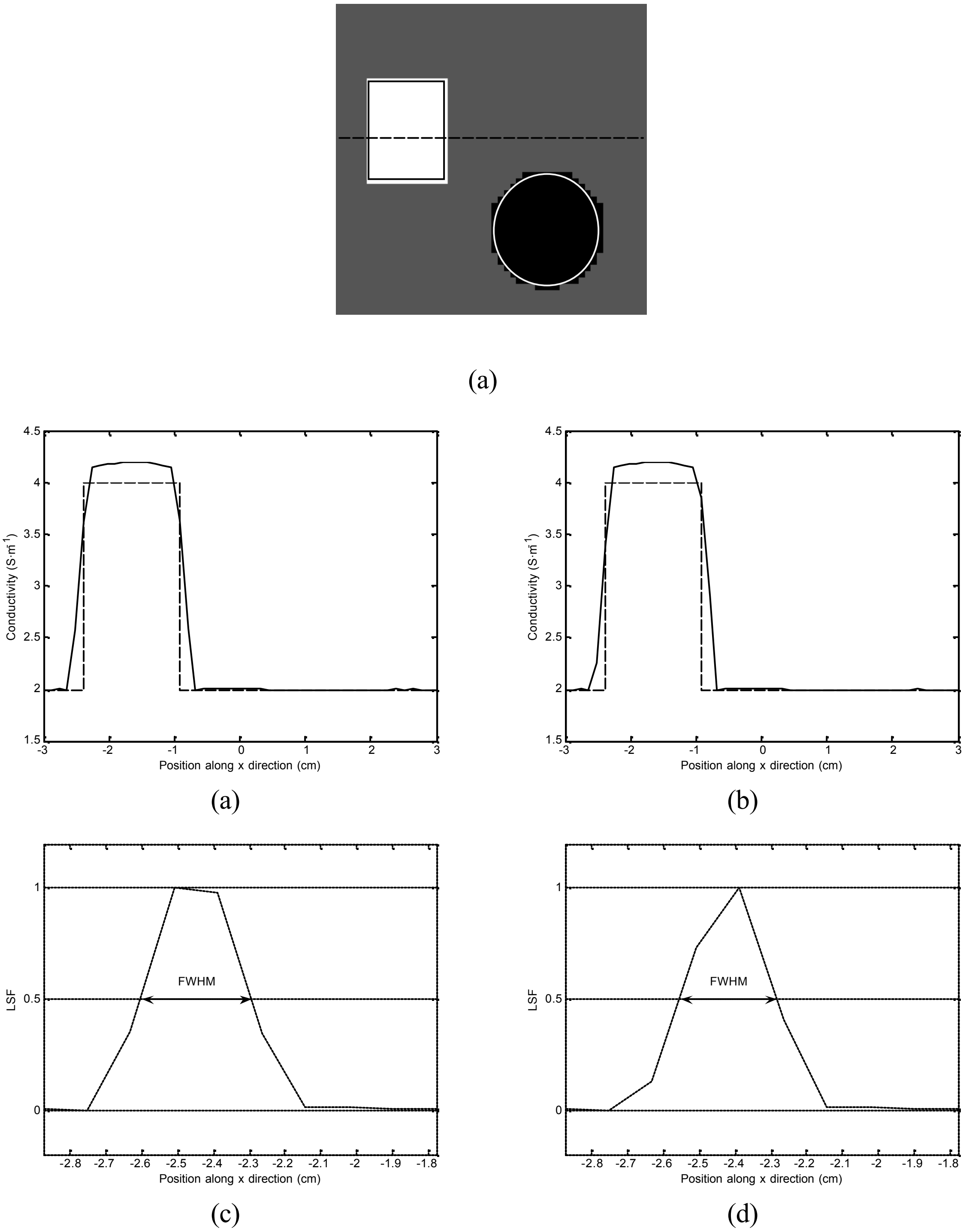

(a)

(a)

(b)

(c)

(d)

Figure 5.10: Profile and LSF images for reconstruction by integration along Cartesian grid lines. Noise-free case. Average between vertical and horizontal integrations. (a) True distribution. The dashed line gives the definition of the profile images. (b) Profile image for trapezoidal integration. (c) Profile image for Taylor expansion method. (d) LSF for trapezoidal integration. (e) LSF for Taylor expansion.

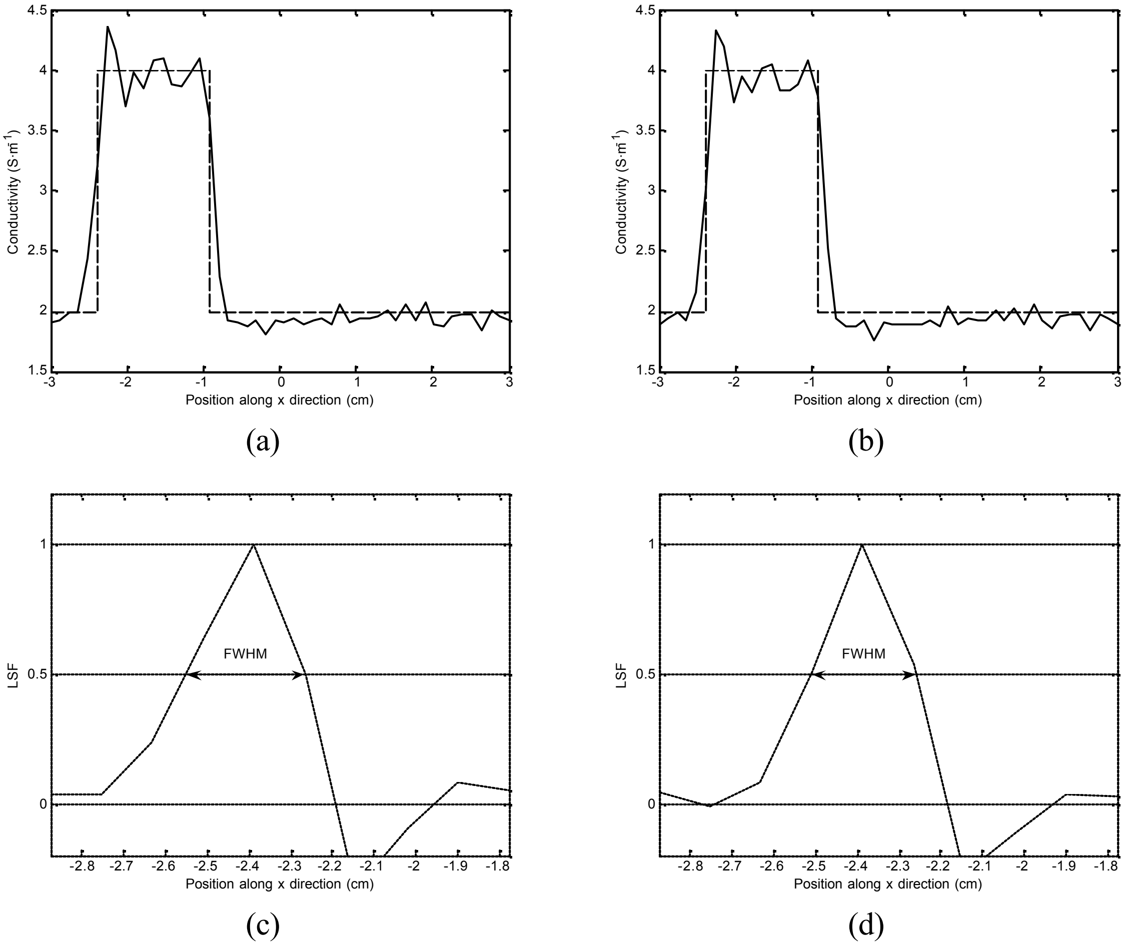

(a)

(b)

(c)

(d)

Figure 5.11: Profile and LSF images for reconstruction by integration along Cartesian grid lines. SNR 20. Average between vertical and horizontal integrations. (a) Profile image for trapezoidal integration. (b) Profile image for Taylor expansion method. (c) LSF for trapezoidal integration. (d) LSF for Taylor expansion.

5.6.3 Reconstruction by Solution of a Linear Equation System

In this section, the reconstructed images of the conductivity models using the finite difference set of equations algorithm, described in Section 3.4 are given. The effects of different noise levels are considered.

By setting one single point with the true resistivity (e.g. the left-upper corner), as explained previously, the absolute conductivity image can be obtained. The reconstructed conductivity image for the noise-free case can be seen in Figure 5.12(a). The finite difference method provokes artifacts in grid shape, since one pixel is related with the four around. Besides, the contours of the objects are very well defined.

For the noise cases, the performance of the algorithm have been tested with SNR equal to 60, 30, 20, 10 and 5. In Figure 5.12, the resulting conductivity images can be seen, from (b) to (f), respectively. The Table 5.8 shows the errors in the reconstruction. It can be seen that the algorithm is very robust against noise. Even in the case of SNR equal to 5, the objects can be inferred, although the committed errors are important.

Table 5.8: Errors in reconstruction by solution of a linear equation system

Reconstructed Conductivity	**Circle** ($e_{s\,Circ}$) **(%)**	**Rectangle** ($e_{s\,Rect}$) **(%)**	**Background** ($e_{s\,Bkcg}$) **(%)**	**Total error (%)**
Noise-free	10.69	13.84	4.32	8.67
SNR 60	11.12	13.85	5.20	9.07
SNR 30	13.68	13.57	7.11	10.38
SNR 20	13.25	13.41	8.15	10.61
SNR 10	26.73	20.74	20.14	21.85
SNR 5	69.45	37.65	52.88	53.15

Therefore, this algorithm needs to specify the resistivity at a single point in order to reconstruct true conductivity distribution. Moreover, it is very robust against noise, being able to reconstruct with SNR equal to 5.

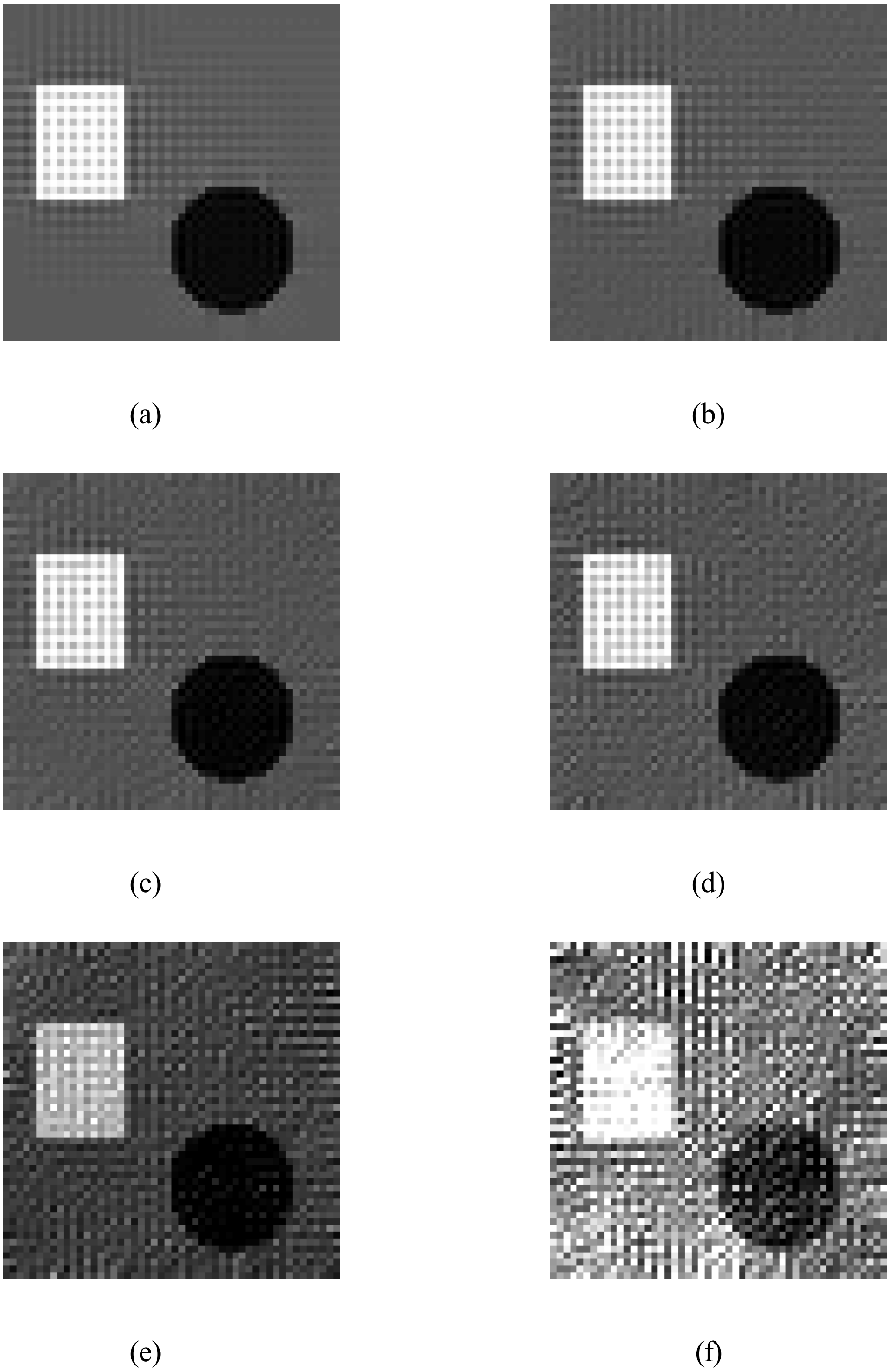

(a) (b)

(c) (d)

(e) (f)

Figure 5.12: Reconstruction by solution of a linear equation system. All the figures use the same gray scale. (a) Reconstructed conductivity image for the noise-free case. Reconstructed conductivity images for (b) SNR 60, (c) SNR 30, (d) SNR 20, (e) SNR 10, (f) SNR 5.

5.6.4 Reconstruction with Equipotential – Projection Algorithm

This section contains the results and discussion of the reconstructed conductivity images, using the method described in Section 3.5. The effects of different noise levels are studied. The true conductivity distribution can be reconstructed if at least at one point it is known. The result can be seen in Figure 5.13(a).

The equipotential paths are calculated by starting ten equipotential lines per pixel from the left edge of the phantom, in the same way as previously explained in Section 5.6.1. Similar problems to the reconstruction by integration along equipotential lines method have been observed.

In the noise-free reconstructed conductivity image, Figure 5.13 (b), the darkest pixels in the upper and lower regions are set to zero conductivity, due to the lack of equipotential lines crossing those pixels. In these regions, the potential cannot be set, but a zero value is assigned, instead. By imposing this, the calculated gradient of potential at the boundaries of these regions shows a big discontinuity and, therefore, the reconstructed conductivity values have large errors. These unset regions are not taken into consideration for error calculations, given in Table 5.9. However, as said before, the pixels just in the border with those regions make the error values increase very significantly. For example, just under the circle, these transition effects can be seen. As a result, the background error becomes more important than in previous reconstruction algorithms.

As the simulated noise level in the current density increases, the calculated equipotential lines are heavily affected and many must be discarded. Therefore, many pixels will not be crossed by any equipotential line and their values will remain unknown. Another consequence is that some pixels can be isolated between regions of unknown value and the integration can produce huge numbers, provoking very large errors. This effect is very noticeable for the case of SNR equal to 20.

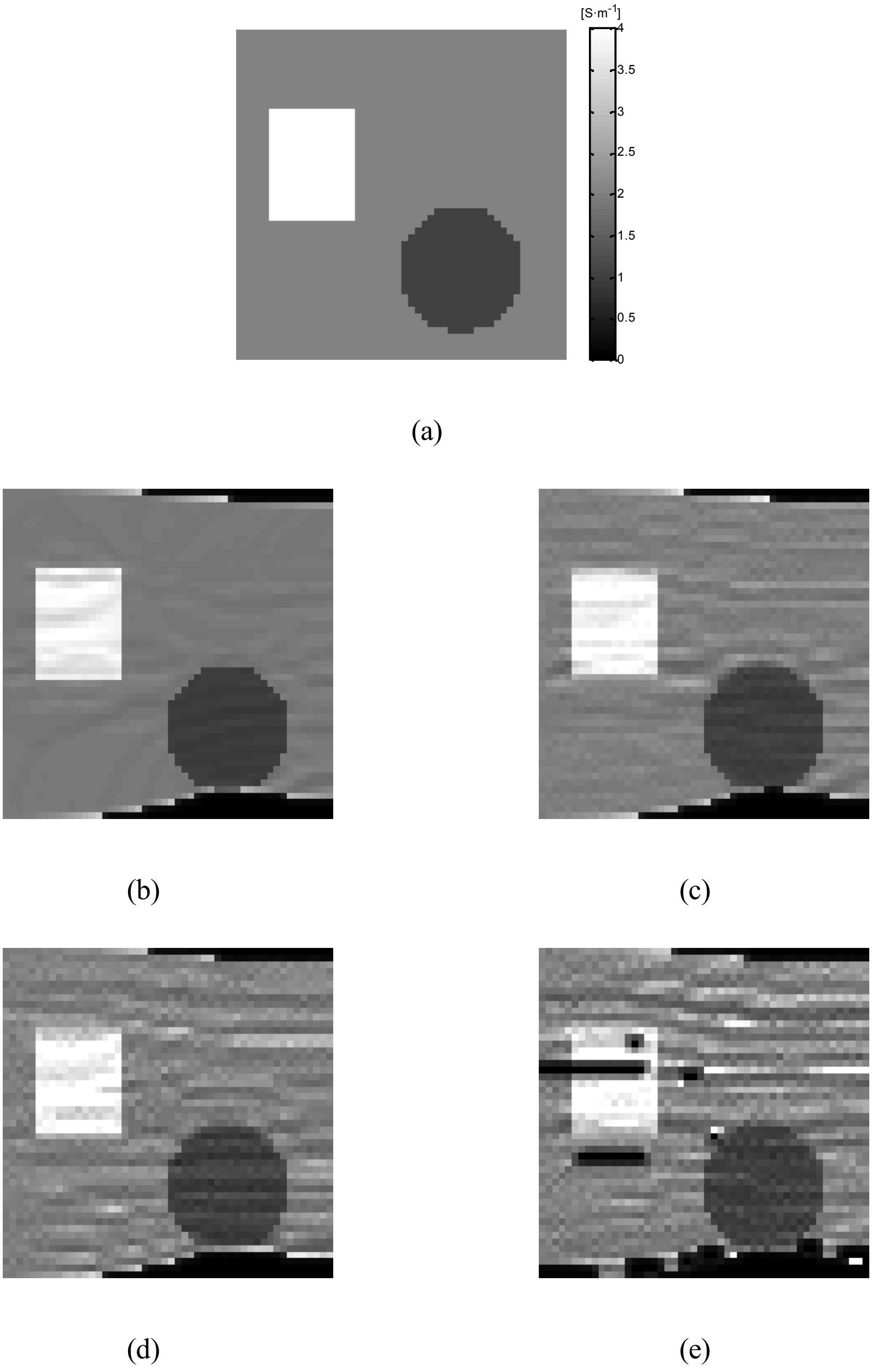

(a)

(b)

(c)

(d)

(e)

Figure 5.13: Reconstruction with equipotential – projection algorithm. Comparison between noise-free and noisy cases. 10 equipotential lines start from each pixel at left edge. All figures have the same gray scale. (a) True conductivity distribution. (b) Reconstructed conductivity distribution for noise-free case. Reconstructed conductivity images for (c) SNR 60, (d) SNR 30 and (e) SNR 20.

Table 5.9: Errors in reconstruction with equipotential – projection algorithm

Reconstructed Conductivity	**Circle ($e_{s\,Circ}$) (%)**	**Rectangle ($e_{s\,Rect}$) (%)**	**Background ($e_{s\,Bkcg}$) (%)**	**Total error (%)**
Noise-free	9.13	7.16	18.83	16.05
SNR 60	13.94	14.39	19.95	18.34
SNR 30	23.37	17.73	23.49	21.92
SNR 20	18.20	31.92	2 x 10^{15}	2 x 10^{15}

Therefore, this algorithm is also very sensitive to noise. The absence of equipotential lines provokes very important errors in the pixels nearby. As before, this method needs to know the resistivity for at least one point in order to reconstruct true conductivity images.

5.6.5 Reconstruction using J-substitution Algorithm

In this section, the conductivity images produced by this last current density based algorithm, described in Section 3.6, are given. The effects of different noise levels and electrode sizes are studied. The corresponding errors are given in Table 5.10.

This iterative reconstruction algorithm begins setting an initial uniform resistivity distribution $r^0 = 1$ to the whole image. Two orthogonal current profiles have been used, as defined previously in Figure 5.1. In each iteration, the forward problem defined in (3.45) is solved for one injection profile by cell-centered finite difference method. Thus, the solution of the linear system (2.39) yields a conductivity distribution, which is used as initial guess for the next iteration, where the other injection profile is utilized.

As it was stated previously in Section 5.4, two different stopping criteria can be used to terminate the iterations: if the difference in resistivity between two successive iterations is below a given threshold, or the error with respect to the true distribution, which is known in these simulation cases, is minimum.

Table 5.10: Errors in reconstruction using J-substitution algorithm

Reconstructed Conductivity	**Circle** ($e_{s\ Circ}$) **(%)**	**Rectangle** ($e_{s\ Rect}$) **(%)**	**Background** ($e_{s\ Bkcg}$) **(%)**	**Total error (%)**	$e_{s\ ,m}$
			Large electrodes		
Noise-free					
Iteration 5	6.14	11.30	3.39	6.96	0.0573
Iteration 26	4.47	7.79	2.90	5.05	0.0584
SNR 60					
Iteration 20	5.24	8.11	3.46	5.49	0.0647
Iteration 5	6.93	11.47	3.92	7.28	0.0638
SNR 30					
Iteration 20	7.26	8.45	5.05	6.59	0.0822
Iteration 5	9.02	11.59	5.17	8.00	0.0820
SNR 20					
Iteration 20	10.36	9.31	6.65	8.04	0.1012
Iteration 15	10.32	10.00	6.41	8.12	0.1012
			Small electrodes		
Noise-free					
Iteration 30	7.13	7.90	6.06	6.82	0.0538
Iteration 29	5.77	7.25	5.35	6.10	0.0544
SNR 60					
Iteration 11	12.71	9.03	12.50	12.14	0.1461
Iteration 20	14.92	9.66	13.87	13.41	0.1432
SNR 30					
Iteration 1	47.78	31.59	25.38	28.66	0.2937
Iteration 3	26.29	15.95	40.57	36.95	0.2491
Iteration 20	25.93	13.21	127.96	113.17	0.3071
SNR 20					
Iteration 1	59.16	32.73	33.65	35.33	0.3760
Iteration 5	34.90	19.98	64.25	57.87	0.3324
Iteration 20	37.07	18.37	178.67	158.02	0.2592

In order to determine which criteria is optimum, a total of thirty iterations have been carried out for the noise-free case. Figure 5.14(a) shows the percentage of error for the different conductivity regions, the background and the error for the whole image in each iteration. The fast convergence behavior of this algorithm is noticeable. The oscillations appear because, in each iteration, a different injection profile is used. The one which provides lowest errors is the vertical profile, labeled as "1" in Figure 5.1(b). In Figure 5.14(b) it is seen how the total error for noise-free cases decreases monotonically, but starts to increase again after the 26th iteration, so this one is chosen for obtaining the minimum total error.

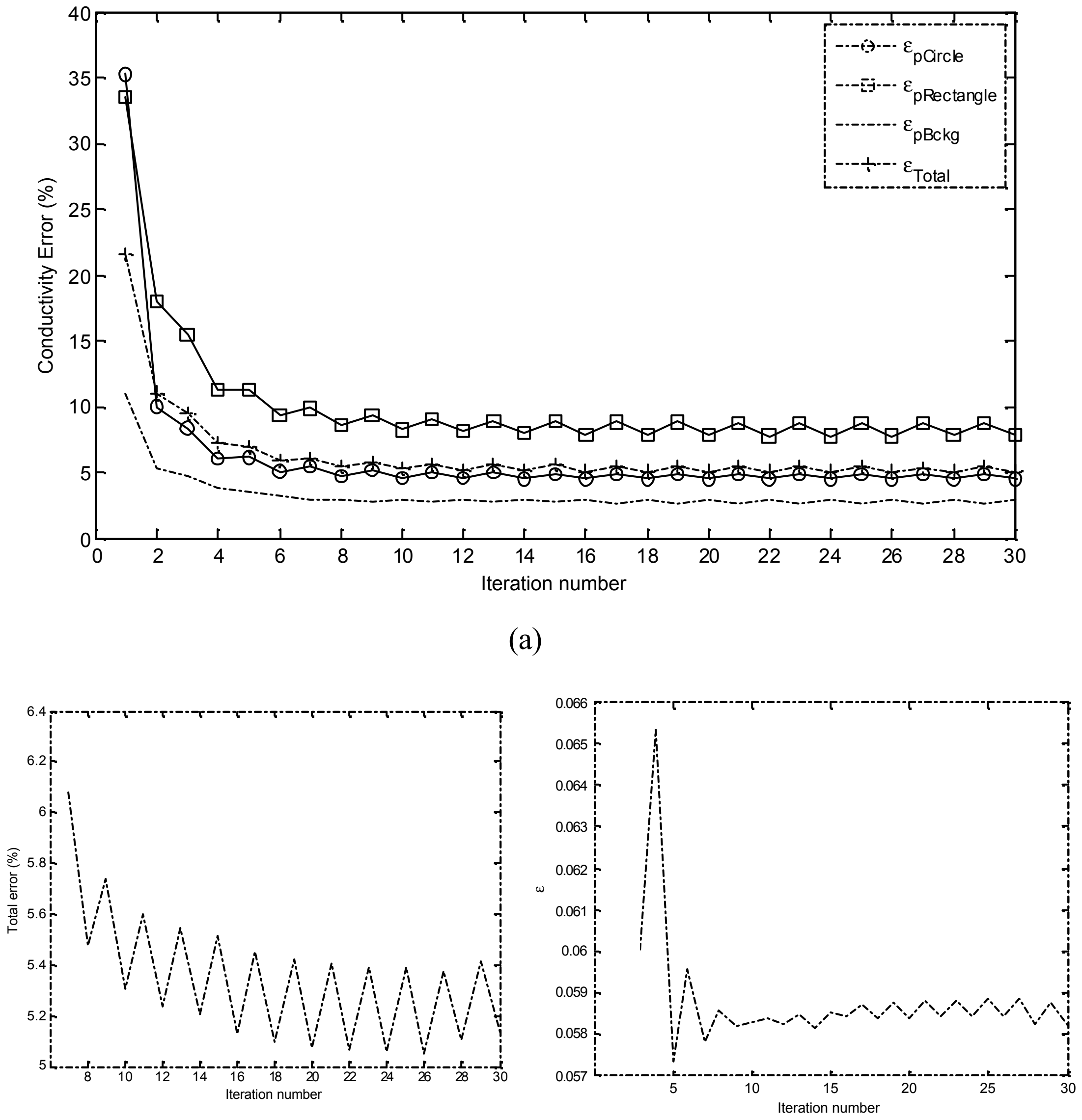

(a)

(b)

(c)

Figure 5.14: Convergence characteristic and conductivity errors for J-substitution algorithm for the noise-free case. (a) Convergence characteristics from first to thirtieth iteration. (b) Total error function for the whole image. (c) Difference in resistivity between two consecutive iterations.

Besides, the difference in conductivity between two consecutive iterations is shown in Figure 5.14(c), There is a minimum for the 5th iteration, so this threshold is taken to satisfy the first criterion. Only the conductivity image for the 26th iteration in noise-free case is shown in Figure 5.15(b), because the difference is practically imperceptible.

Moreover, different levels of noise in the simulated current density data are added, and their effects are studied. The resulting images are also displayed in Figure 5.15. The convergence curve, defined as the total error of the reconstructed image in each iteration, for all noise levels is shown in Figure 5.19(a). It is noticeable that the algorithm always converges, and reconstructs with only 8% of error when SNR is 20.

Since Kwon *et al* [20] use small electrodes in their study, this case is now considered. The electrode sizes are chosen as one third of the phantom edge width. The total conductivity distribution is shown in Figure 5.16, while the reconstructed images are given in Figure 5.18. The noise-free case presents a similar figure, but, when the noise increases and becomes considerable, the algorithm diverges, as shown in the convergence curve in Figure 5.19(b). In order to find the best result, there is a compromise between the total error, mainly due to the divergence of the background, and the errors corresponding to the objects which are wanted to be reconstructed. This can be seen in Figure 5.17.

The reconstruction errors are given in Table 5.10. As it can be seen, in some cases, the minimum total error may be preferred, while in other cases, a minimum error in reconstructing a particular conductivity region may be a priority. The main contributor to this large error in the background seems to be the corners, which become reconstructed badly and with higher values as the number of iterations increases. This is because the electrodes are small and centered. The current is not spread uniformly, and very low amount of current reaches the corners.

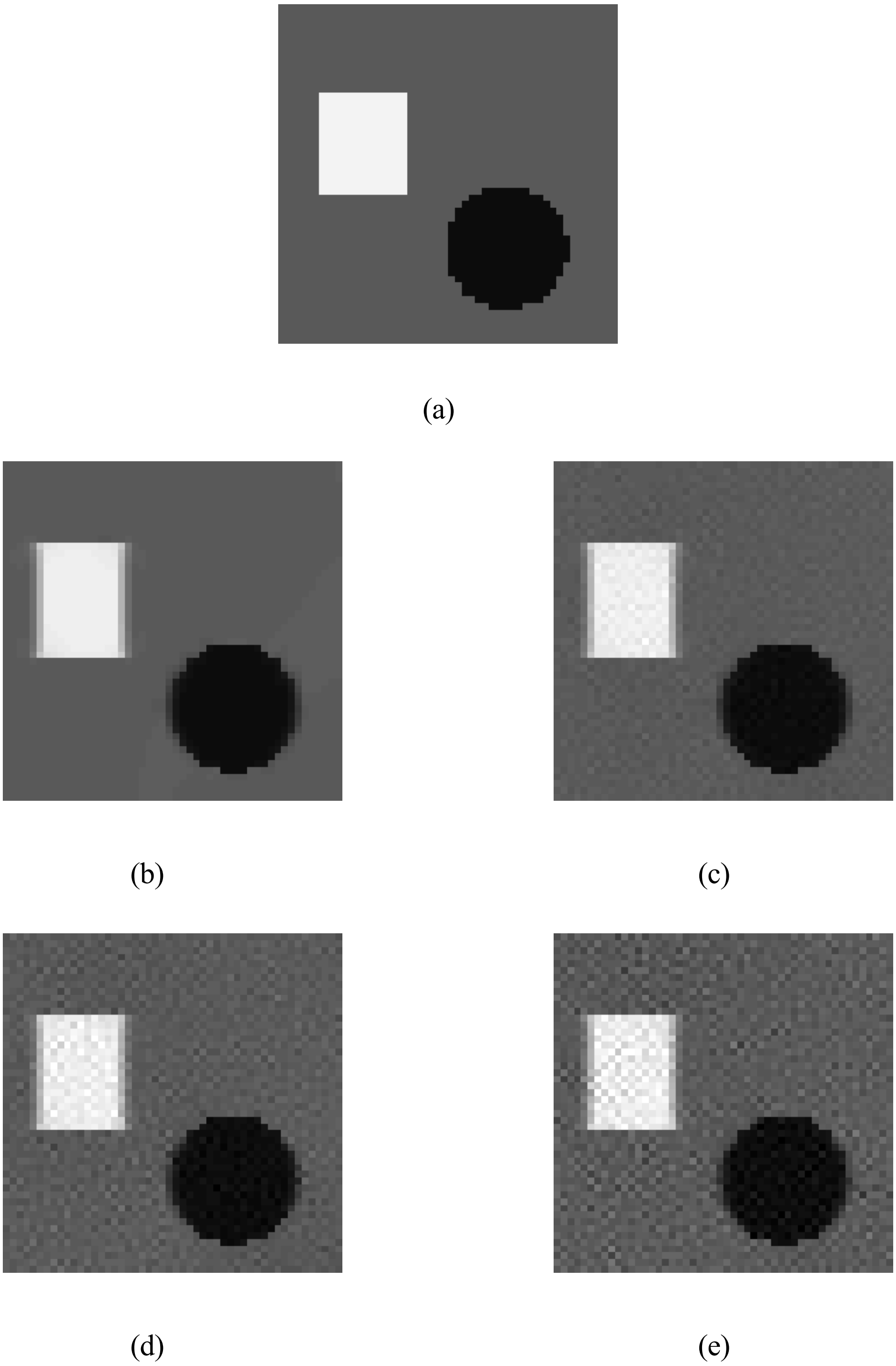

Figure 5.15: Reconstruction for J-substitution algorithm. Large electrodes. All figures have the same gray scale. (a) True distribution. (b) Noise-free case. Iteration 26. (c) SNR 60. Iteration 20. (d) SNR 30. Iteration 20. (f) SNR 20. Iteration 20.

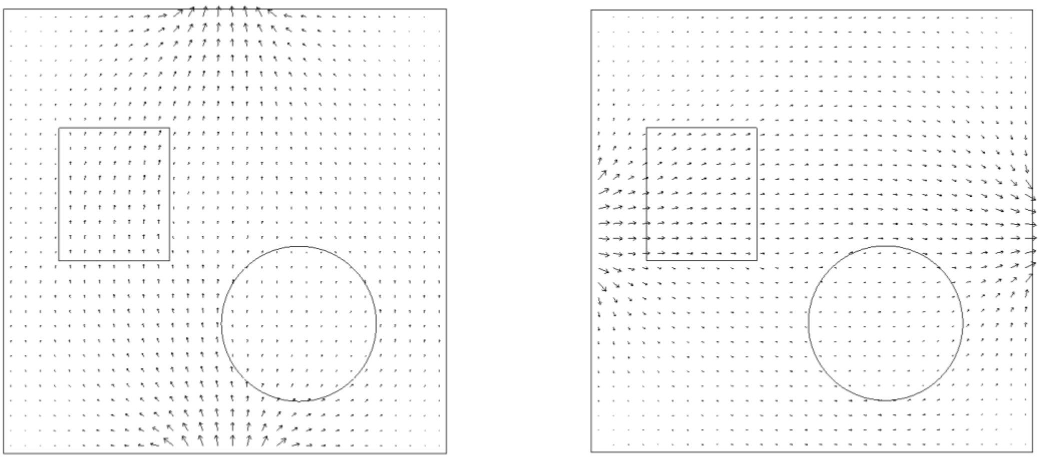

(a) (b)

Figure 5.16: Total current density distribution for small electrodes, for injection patterns 1 (a) and 2 (b)

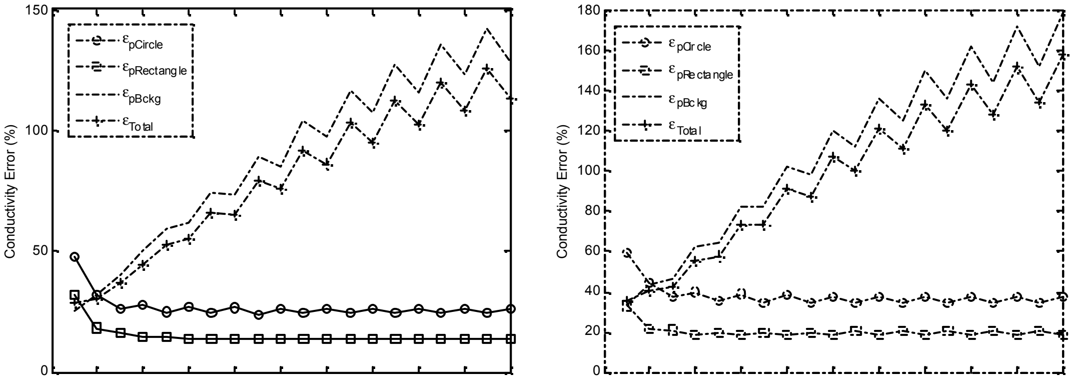

(a) (b)

Figure 5.17: Convergence characteristic of J-substitution algorithm for small electrodes. (a) SNR equal to 30. (b) SNR equal to 20.

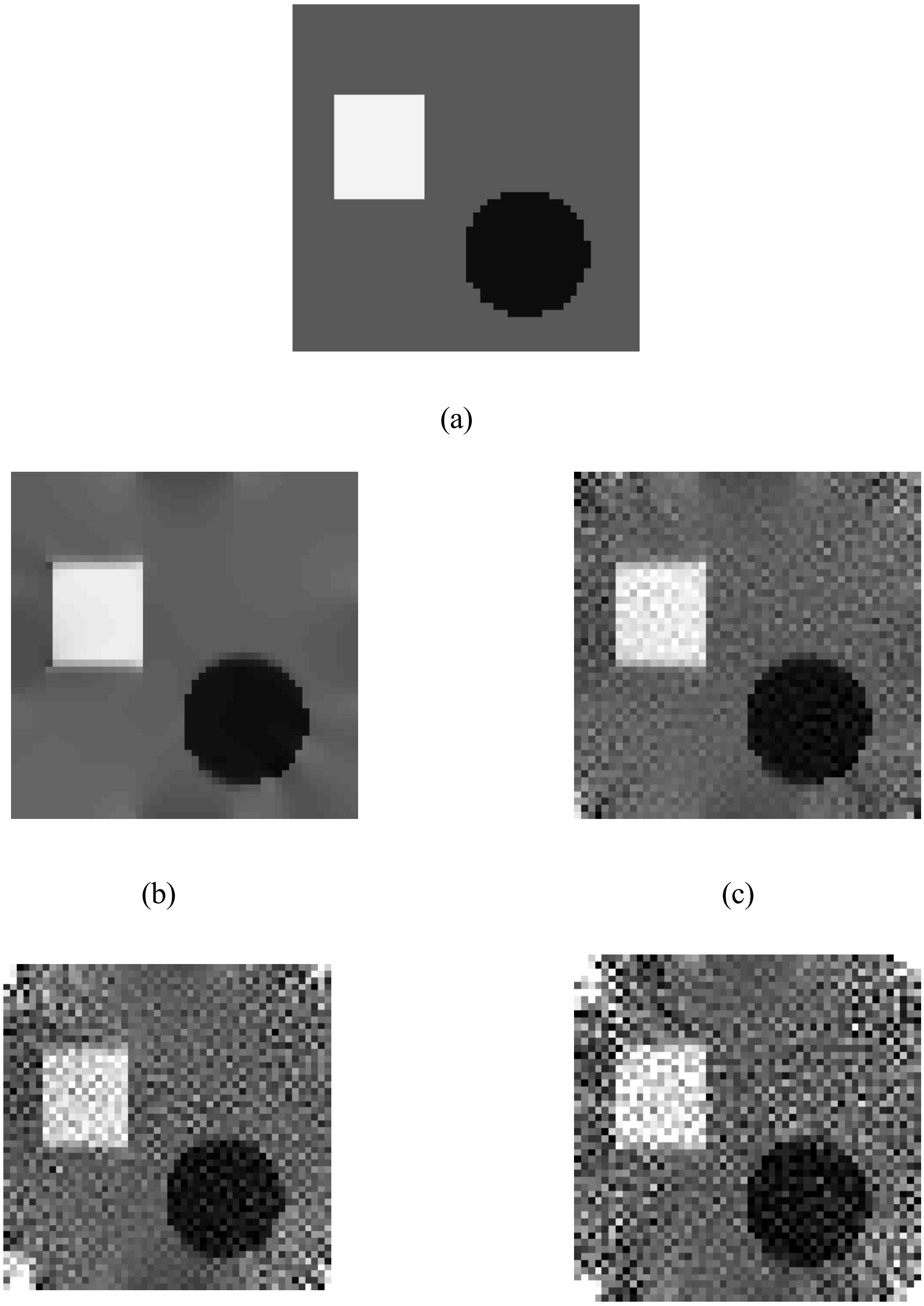

(a)

(b)

(c)

(d)

(e)

Figure 5.18: Reconstruction for J-substitution algorithm. Small electrodes. All figures have the same gray scale. (a) True distribution. (b) Noise-free case. Iteration 29. (c) SNR 60. Iteration 20. (d) SNR 30. Iteration 3. (f) SNR 20. Iteration 5.

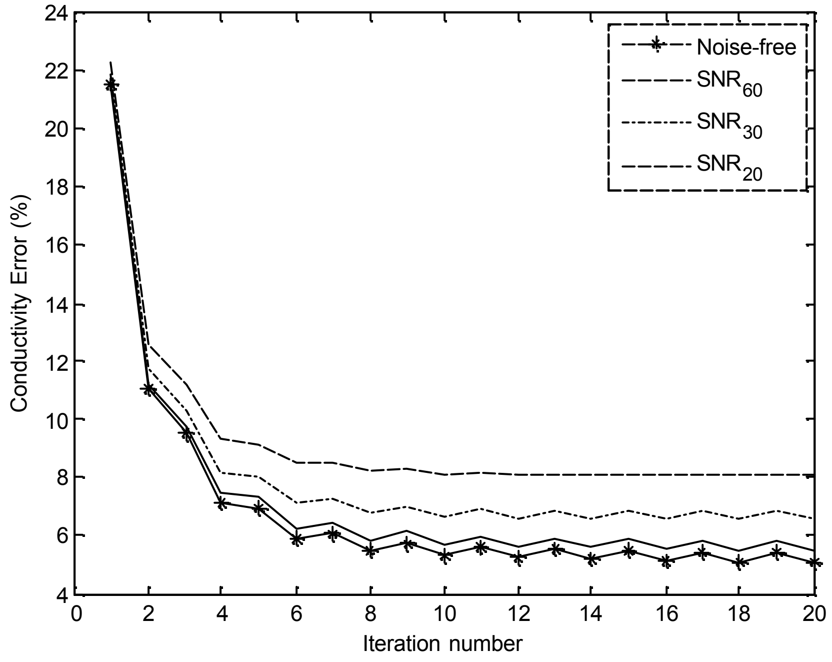

(a)

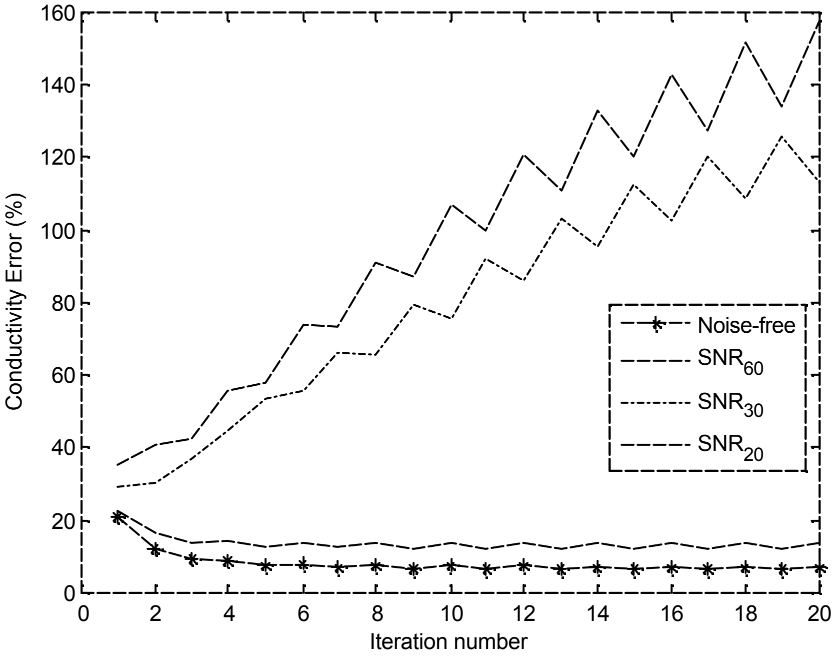

(b)

Figure 5.19: Convergence characteristic of J-substitution algorithm with different noise levels, with (a) large electrodes; (b) small electrodes.

Therefore, this iterative algorithm yields very low errors when the electrodes cover the whole sides, as the previous algorithms. An initial resistivity distribution is needed, but a reasonable guess is enough to make it converge. Another requirement is the measurement of the voltage between the electrodes in order to get a true conductivity image. One disadvantage is that, since it is iterative, it needs a lot of computation time and resources in order to solve the forward problem for each iteration. This depends on the level of noise and size of the image. For example, in an AMD64 3000+, 2 GB of RAM, Matlab R2006b on Windows XP x64 SP1, the 20 iterations for the noise-free case and large electrodes could take around three hours.

5.7 Simulation Results for Magnetic Flux Density Based Algorithms

In this section, the reconstructed conductivity images produced by the Harmonic B_z algorithm, described in chapter 4, are given and discussed. This algorithm has been tested for the simulated phantom described in 5.2.1, under different noise levels.

This iterative reconstruction algorithm begins assuming an initial uniform conductivity distribution $s_0 = 1$ for the whole image. Two orthogonal current profiles have been used, as defined previously in Figure 5.1. In each iteration, the forward problem defined in (4.11) is solved for each injection profile by cell-centered finite difference method. Then, a new conductivity distribution is calculated using (4.6), (4.9) and (4.10), and fed into the next iteration.

Figure 5.20 shows the reconstructed images for different noise levels after six iterations, where the tolerance $e = 0.05$ has been used as stopping criterion. In Table 5.11, the corresponding errors for each case are given. It is observed that the algorithm converges quickly and the errors remain low, due to the iterative characteristic of this method. Another observation is that even when the error grows as the SNR decreases, the appearance of the images remains quite acceptable. The main drawback of this method is the large computation time for each iteration. For example, for the same equipment as described above, each iteration could cost around 40 minutes.

Table 5.11: Errors in reconstruction using Harmonic B_z algorithm

Reconstructed Conductivity	**Circle ($e_{s\,Circ}$) (%)**	**Rectangle ($e_{s\,Rect}$) (%)**	**Background ($e_{s\,Bkcg}$) (%)**	**Total error (%)**	$e_{s,m}$
			Large electrodes		
Noise-free					
Iteration 6	8.51	4.50	5.08	5.37	0.049
SNR 60					
Iteration 6	8.72	12.41	10.96	12.09	0.049
SNR 30					
Iteration 6	12.84	13.61	12.97	14.03	0.050
SNR 20					
Iteration 6	16.62	17.23	16.27	17.11	0.050

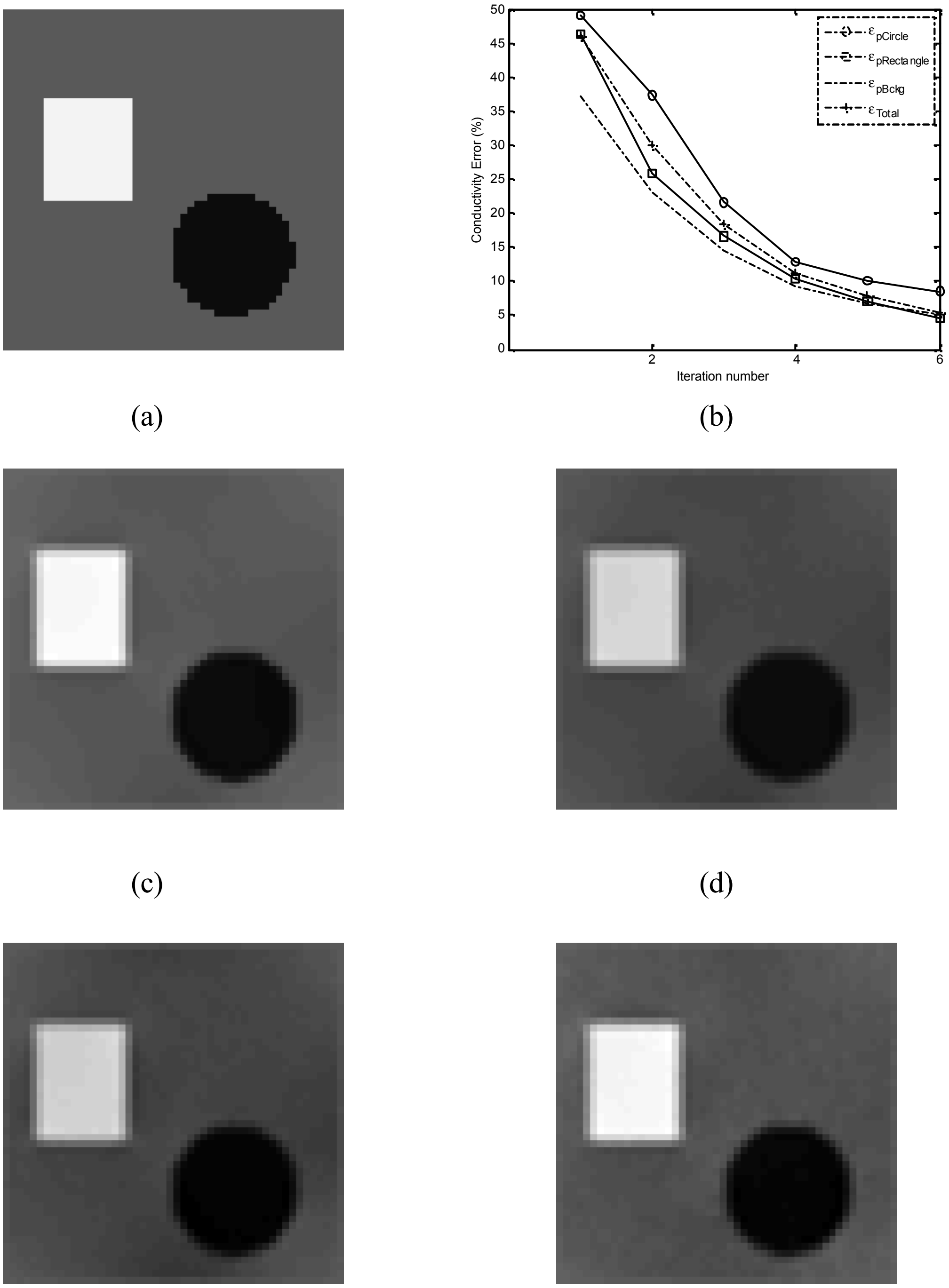

(a) (b)

(c) (d)

(e) (f)

Figure 5.20: Reconstruction for Harmonic B_z algorithm. Large electrodes. All figures have the same gray scale. (a) True distribution. Reconstructed images are given at 6th iteration. (b) Convergence characteristic for the noise-free case. (c) Noise-free case. (d) SNR 60. (e) SNR 30. (f) SNR 20.

5.8 Partial FOV/ROI reconstruction

These algorithms can also reconstruct a region of interest (ROI) within the image, instead of obtaining the full field of view (FOV). This feature can be applied in some practical applications, where optimum injection patterns for specific conductivity regions are used. Thus, a full FOV can be better reconstructed by combining different optimized ROI.

As an example, two different ROI's, defined in Figure 5.21(a), have been reconstructed using the equipotential-projection algorithm, with a single measurement point, for the noise-free case. As in the previous Section 5.6.4, the lack of equipotential lines provides unknown conductivity values, which are shown as the darkest areas in the reconstructed images in Figure 5.21. The borders of these areas, due to the gradient operator intrinsic to this algorithm, produce conductivity values with high error, which, consequently, raise heavily the error of the conductivity region at which they belong to.

Table 5.12: Errors in reconstructing different ROI

Reconstructed ROI	Circle ($e_{s\,Circ}$) (%)	Rectangle ($e_{s\,Rect}$) (%)	Background ($e_{s\,Bkcg}$) (%)	Total error (%)
ROI 1	N. A.	8.44	11.85	9.42
ROI 2	17.55	N. A.	23.15	24.56

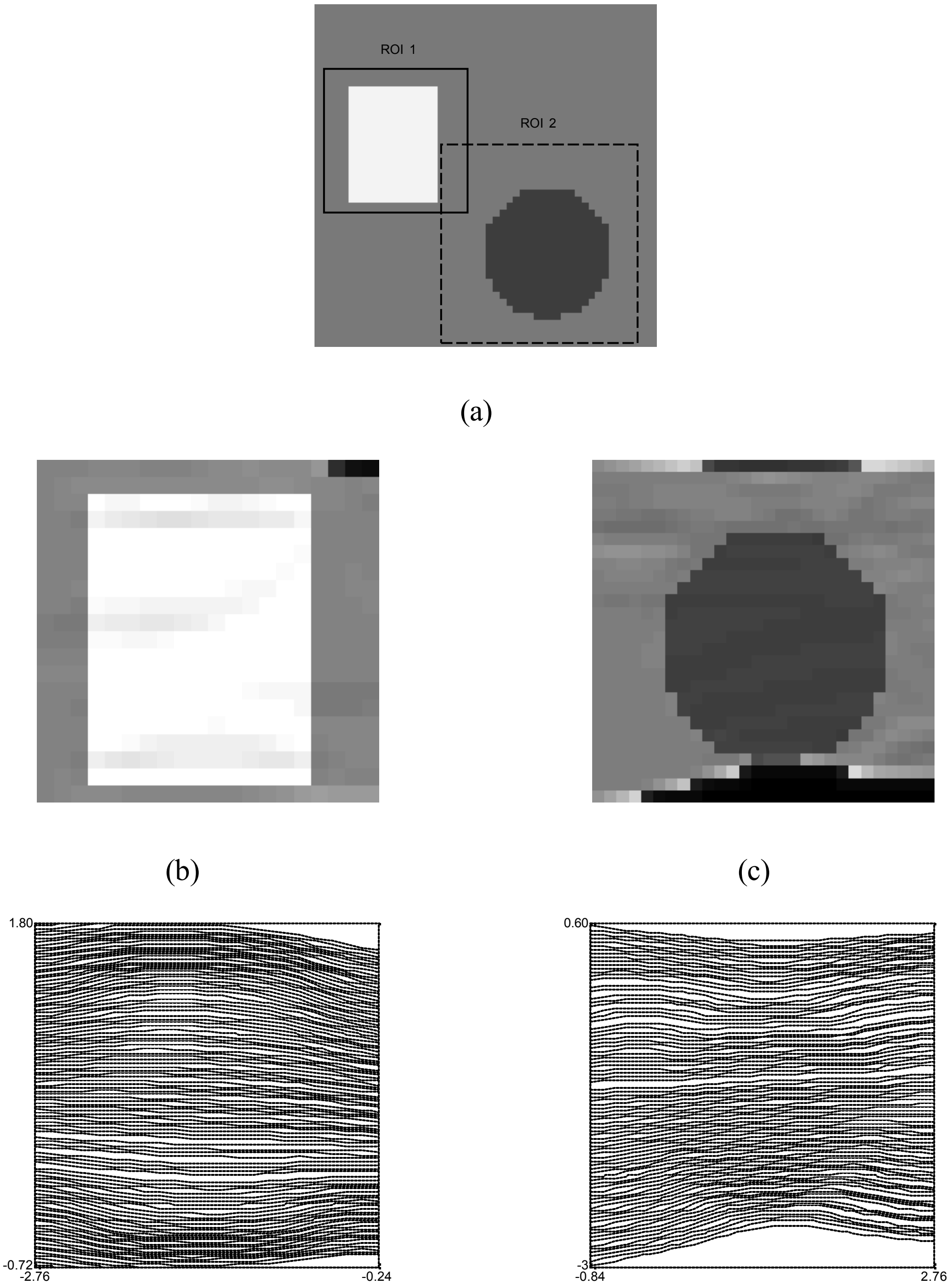

(a)

(b)

(c)

(d)

(e)

Figure 5.21: Reconstruction of two different ROI's with equipotential-projection algorithm. All figures have the same gray scale. (a) True distribution with the definition of ROI1 and ROI2. Reconstructed images for (b) ROI1 and (c) ROI2, with 10 equipotential lines starting from each pixel at left edge. Equipotential lines for (d) ROI1 and (e) ROI2. In order to distinguish them easily, in (d), only 4 equipotential lines have been started per each left-side pixel, while 3 equipotential lines have been used in (e).

5.9 Comparison between reconstruction algorithms

In this section, the previous reconstruction algorithms are compared under the same conditions for simulated and experimental data. The resulting images are taken as the direct output of the reconstruction algorithms, without applying any image processing.

5.9.1 Simulated data

The simulated data corresponds to the numerical phantom previously defined in Section 5.2.1 and shown in Figure 5.22. The reconstructed algorithms are compared for the noise-free case and different noise levels. Errors committed in the reconstruction and blurring effects are studied and quantified.

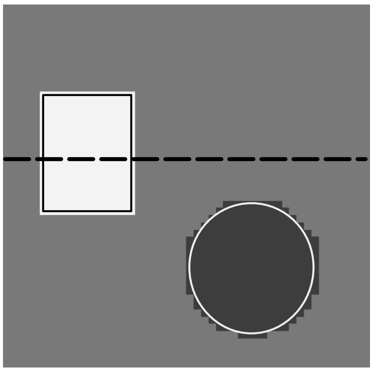

Figure 5.22: True conductivity distribution. Exact locations of the different conductivity regions are shown. The dashed line gives the definition for the profile image.

5.9.1.1 Noise-free case

For noise-free simulated data, the reconstruction algorithms are evaluated under the following set of conditions: large electrodes, ten equipotential lines per pixel, trapezoidal integration method and averaging between vertical and horizontal integration, if applicable. The reconstructed conductivity images for each algorithm are presented in Figure 5.23. The committed errors are given in Table 5.13. In Figure 5.24, the horizontal profiles for a line crossing an edge of the rectangle, as defined in Figure 5.22, are shown. Besides, in Figure 5.25, the Line Spread Functions for the conductivity profiles can be observed. Finally, the calculated LSF widths at FWHM are given in Table 5.14.

Considering only the committed errors, it can be seen that the methods which give the lowest overall one are the iterative algorithms: J-substitution and Harmonic B_z algorithms. This kind of methods corrects themselves iteration by iteration, and if they converge, as in these cases, the provided images are quite accurate. Moreover, the error committed at reconstructing the different conductivity regions is generally lower than in the non-iterative ones. Notice that the condition of large electrodes, in the J-substitution algorithm, provides lower error than small electrodes, due to the decrease of current, and therefore information, near the phantom edges. The main disadvantage of the iterative methods is their large computation time, usually some hours. The direct methods, however, are practically instantaneous. This correction effect could be used to improve the quality of the reconstruction by feeding one of these iterative methods with the solution of a direct one, as initial conductivity distribution.

Table 5.13: Comparison for the noise-free case

Reconstruction Algorithms	**Circle ($e_{s\,Circ}$) (%)**	**Rectangle ($e_{s\,Rect}$) (%)**	**Background ($e_{s\,Bkcg}$) (%)**	**Total error (%)**
Solution of Linear Equation System	10.69	13.84	4.32	8.67
Integration Along Cartesian Grid Lines	13.37	8.54	4.35	6.44
Integration Along Equipotential Lines	17.69	12.15	9.74	11.36
Equipotential – Projection	9.13	7.16	18.83	16.05
J-substitution (large electrodes)	4.47	7.79	2.90	5.05
J-substitution (small electrodes)	5.77	7.25	5.35	6.10
Harmonic B_z	8.51	4.50	5.08	5.37

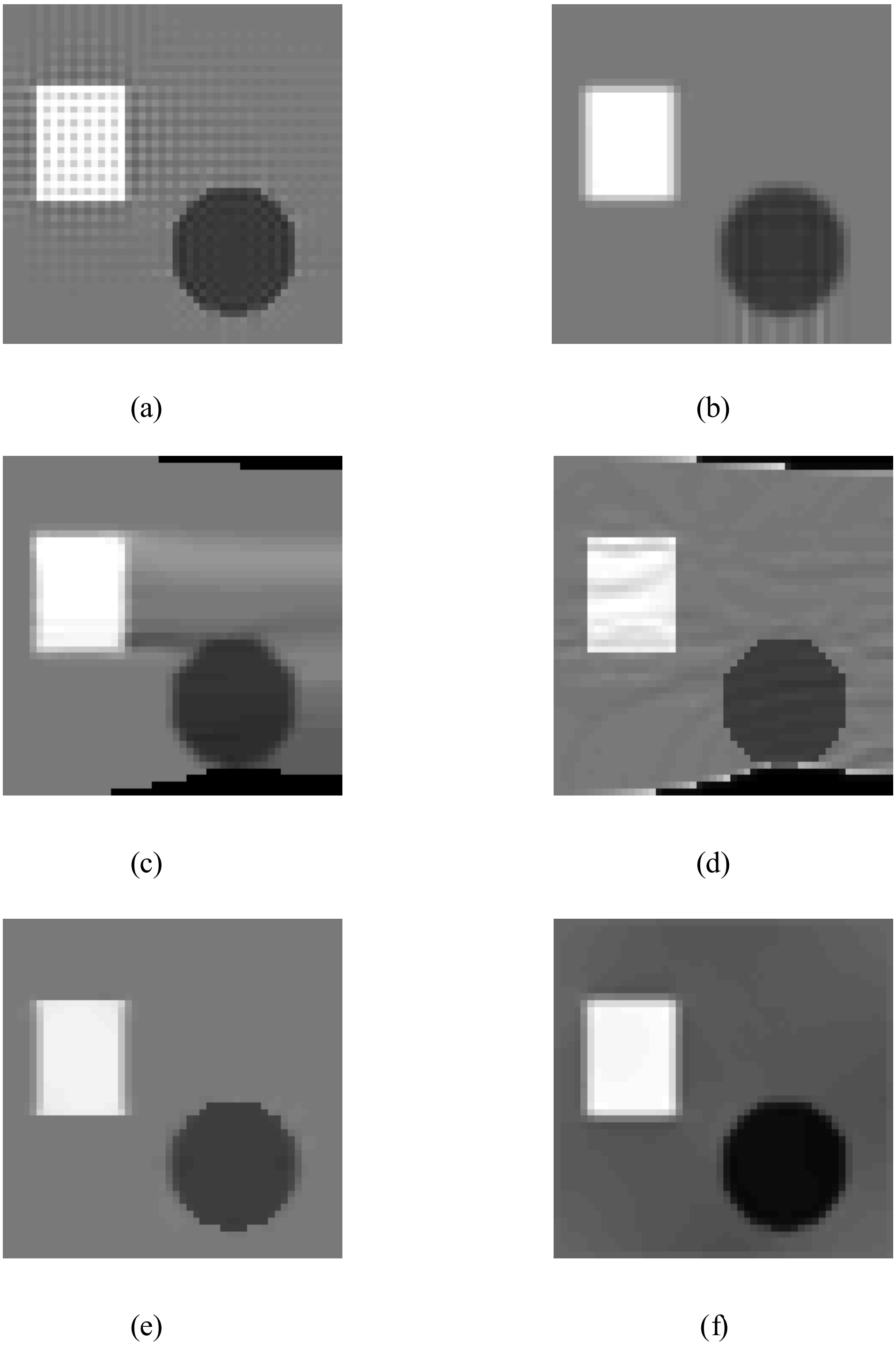

Figure 5.23: Comparison for the noise-free case. All figures have the same gray scale. (a) Reconstruction by solution of linear equation system by finite differences. (b) Trapezoidal integration along cartesian grid lines. Average of vertical and horizontal integration. (c) Trapezoidal integration along equipotential lines. 10 equipotential lines per pixel. (d) Reconstruction with equipotential – projection algorithm. 10 equipotential lines per pixel. (e) J-substitution algorithm with large electrodes. Iteration 26. (f) B_z algorithm. Iteration 6.

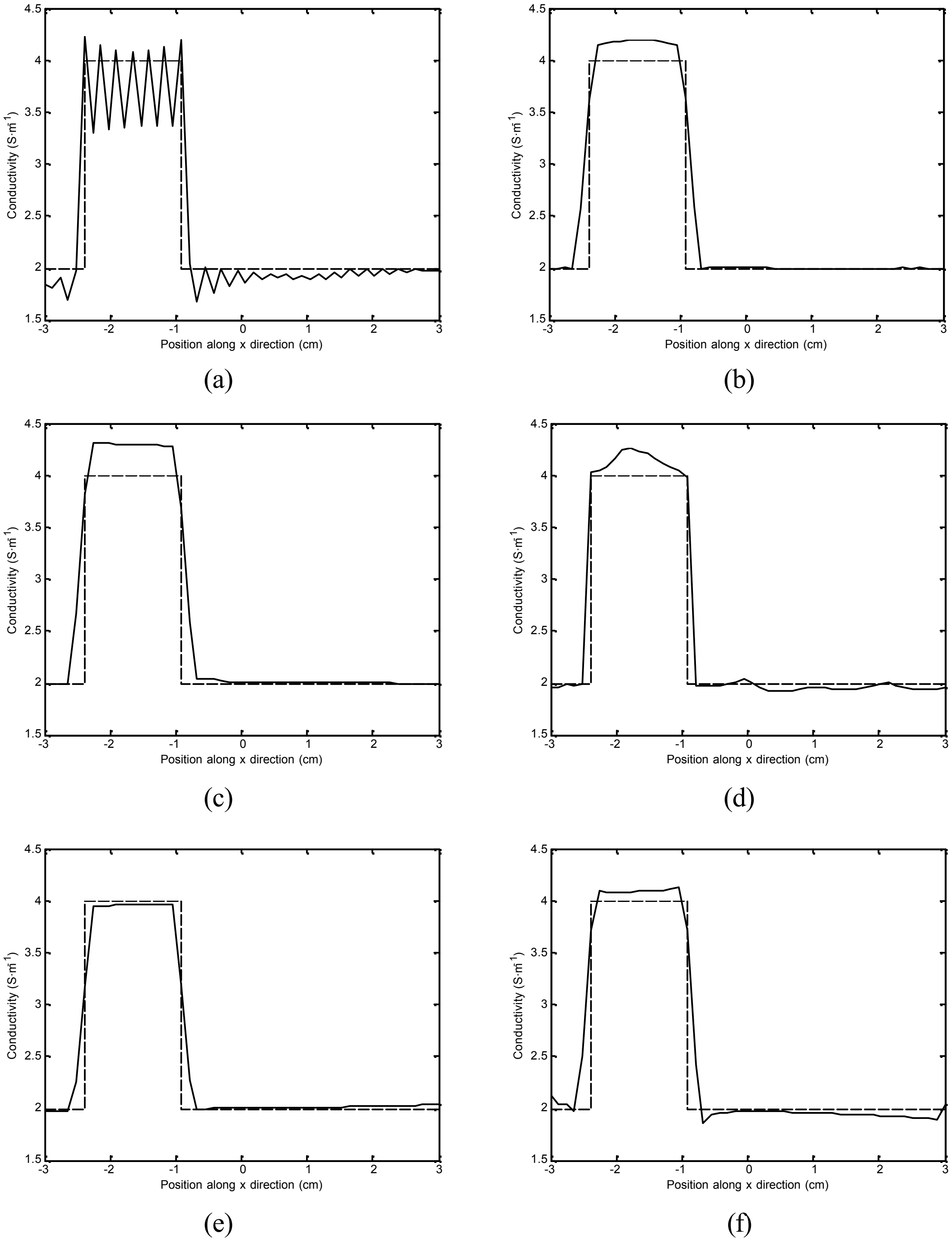

Figure 5.24: Profile images for the noise-free case. (a) Reconstruction by solution of linear equation system by finite differences. (b) Trapezoidal integration along cartesian grid lines. Average of vertical and horizontal integration. (c) Trapezoidal integration along equipotential lines. 10 equipotential lines per pixel. (d) Reconstruction with equipotential – projection algorithm. 10 equipotential lines per pixel. (e) J-substitution algorithm with large electrodes. Iteration 26. (f) B_z algorithm. Iteration 6.

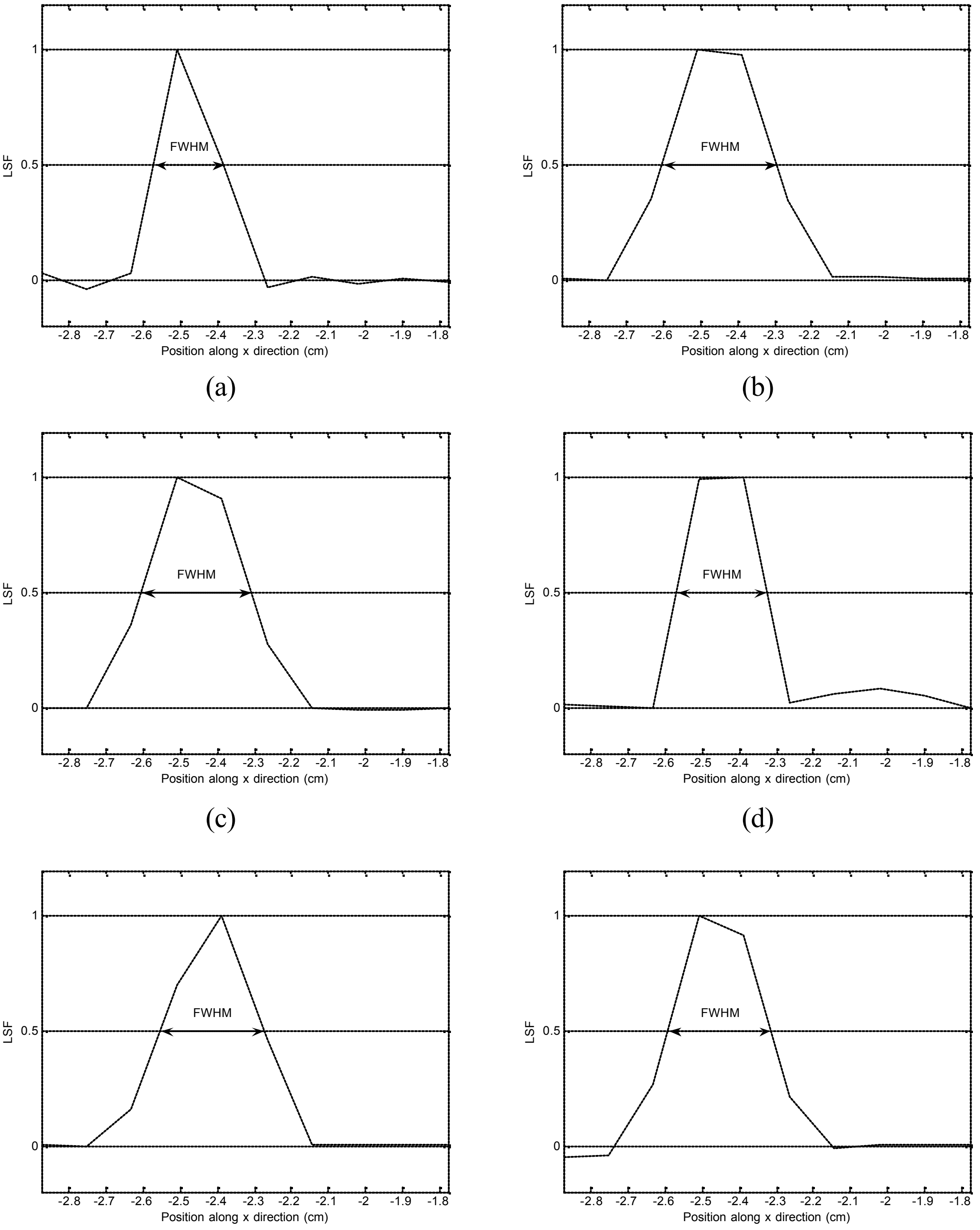

(a) (b) (c) (d) (e) (f)

Figure 5.25: LSF images for the noise-free case. (a) Reconstruction by solution of linear equation system by finite differences. (b) Trapezoidal integration along cartesian grid lines. Average of vertical and horizontal integration. (c) Trapezoidal integration along equipotential lines. 10 equipotential lines per pixel. (d) Reconstruction with equipotential – projection algorithm. 10 equipotential lines per pixel. (e) J-substitution algorithm with large electrodes. Iteration 26. (f) B_z algorithm. Iteration 6.

On the other hand, if the lowest blurring effect is considered, the reconstruction by solving a linear equation system provides the lowest LSF width and therefore, the sharpest image. The reconstruction with equipotential – projection algorithm gives the following sharpest conductivity image. The iterative algorithms, however, provide intermediate LSF widths. Finally, the two integration algorithms present the highest blurring effects. The main reason for this is the error accumulation that this technique suffers from, besides the integration method used: trapezoidal, instead of Taylor expansion.

Table 5.14: FWHM of LSF. Comparison for the noise-free case

Reconstruction Algorithms	**FWHM** (cm)
Solution of Linear Equation System	0.213
Integration Along Cartesian Grid Lines	0.309
Integration Along Equipotential Lines	0.297
Equipotential – Projection	0.246
J-substitution (large electrodes)	0.282
Harmonic B_z	0.278

Comparing now the method of integration along equipotential lines and along cartesian grid lines, it is seen how the latter gives less error. In part, it is due to the average performed between vertical and horizontal integration, but also since the calculated equipotential paths are an approximation to the real ones. The current vectors are assumed to be constant within a pixel, but if it is too big, this assumption cannot be valid. This may happen where the current lines accumulate, for example, at the interface between two regions with different conductivity. It also occurs where the current flow is very little, like at the corners, especially in the case where the electrodes are small compared with the size of the phantom. In the images, the bias effect of the integration along the equipotential paths can be seen in Figure 5.23(c), while in (b) this effect is counteracted, due to averaging.

The reconstruction by solving a linear equation system provides an intermediate solution. The error is not the largest, or the smallest, and the reconstructed image is the least blurred one. One disadvantage is that the image suffers from a grid effect due to the discretization of the finite difference method. This especially makes the rectangle be slightly more erroneous than in the rest of cases and a worse appearance.

The method which provides the largest overall error is the equipotential – projection algorithm, although it is one of the algorithms with sharpest and best defined object contours, especially in the circular object. The reason for the large error is that the regions which are not passed by any equipotential lines remain with unknown values, representing a big discontinuity. When the gradient of the potential is calculated during an intermediate step of the algorithm, these discontinuities provoke important errors in the pixels surrounding these unknown areas. In this case, they are located in the background, so the error at reconstructing the background becomes quite important, even considering that the dark pixels are actually not considered in the error calculation.

5.9.1.2 Noisy cases

In this section, the reconstruction algorithms are compared for a noise level of SNR equal 20. At this noise level, all algorithms can reconstruct images with tolerable errors. The same conditions as in the previous section hold for all the algorithms in order to evaluate them: large electrodes, ten equipotential lines per pixel, trapezoidal integration method and averaging between vertical and horizontal integration, if applicable. The reconstructed conductivity images for each algorithm are presented in Figure 5.26. The committed errors are given in Table 5.15. In Figure 5.27, the horizontal profiles for a line crossing an edge of the rectangle, as previously defined in Figure 5.22, are shown. Moreover, in Figure 5.28, the Line Spread Functions for the conductivity profiles can be observed. Finally, the calculated LSF widths at FWHM are given in Table 5.16.

Table 5.15: Comparison for noisy cases. SNR equal to 20

Reconstruction Algorithms	**Circle** ($e_{s\,Circ}$) **(%)**	**Rectangle** ($e_{s\,Rect}$) **(%)**	**Background** ($e_{s\,Bkcg}$) **(%)**	**Total error (%)**
Solution of Linear Equation System	13.25	13.41	8.15	10.61
Integration Along Cartesian Grid Lines	15.61	11.95	7.53	9.74
Integration Along Equipotential Lines	25.23	25.65	20.12	23.30
Equipotential – Projection	18.20	31.92	2×10^{15}	2×10^{15}
J-substitution (large electrodes)	10.36	9.31	6.65	8.04
Harmonic B_z	16.62	17.23	16.27	17.11

Considering only the overall error, the reconstruction algorithm which gives the lowest error is the J-substitution algorithm at its 20th iteration, as in the noise-free case. Moreover, the error committed at reconstructing the different conductivity regions are lower than in the rest of algorithms. The resulting image has very good quality, apart from an important salt-and-pepper noise, and being the one with most blurred edges. However, it is necessary to notice that this method can diverge when the noise is too high. Therefore, a careful study of its convergence must be carried out, in order to decide which iteration provides the minimum desired error: in total, in a particular area, a balance, etc. If the size of the electrodes is reduced, this algorithm becomes more sensitive to noise and can diverge easier (see Section 5.6.5), since the current flow is not spread uniformly throughout the whole field of view. The other iterative method, the Harmonic B_z algorithm, suffers from larger error, even though the image could be considered as the one with the best appearance.

If the blurring effect is considered as a criterion, the reconstruction by solving a linear equation system provides the lowest LSF width at FWHM, and the reconstruction by integration along Cartesian grid lines provides the largest, as in the noise-free case. The iterative algorithms produce intermediate blurred images. Although the image reconstructed by reconstruction along equipotential lines is quite blurred, the LSF width calculated at the defined profile row gives, by chance, a very good figure.

Table 5.16: FWHM of LSF. Comparison for noisy cases. SNR equal to 20

Reconstruction Algorithms	**FWHM** (cm)
Solution of Linear Equation System	0.192
Integration Along Cartesian Grid Lines	0.287
Integration Along Equipotential Lines	0.200
Equipotential – Projection	0.267
J-substitution (large electrodes)	0.319
Harmonic B_z	0.283

The integration along Cartesian grid lines and solution of linear system come to similar overall errors, although the reconstructed image of the latter has a better looking, since, in the former one, the integration technique spreads the errors along the direction of integration.

The method which provides largest error is the equipotential – projection algorithm. As the noise increases, less equipotential lines are valid, since the directions of current vectors become more random, and the calculated equipotential lines, orthogonal to these vectors, tend to cross each other. Those invalid equipotential paths are removed, as explained before. Thus, more unknown areas appear and, due to the gradient operator involved in the algorithm, the calculation of the conductivity at the surrounding pixels provide erroneous values, sometimes very huge, as shown in Table 5.15.

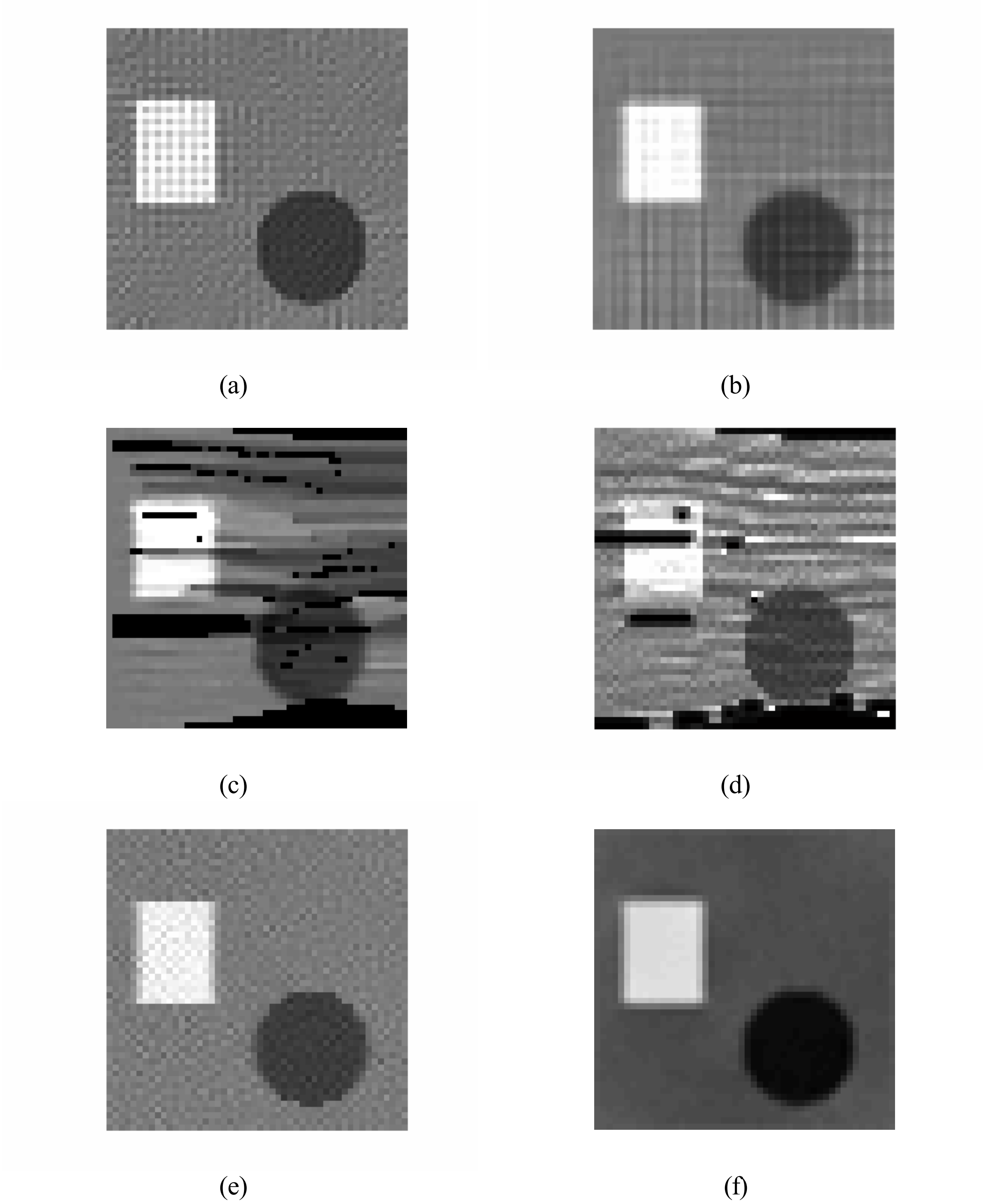

(a) (b)

(c) (d)

(e) (f)

Figure 5.26: Comparison for SNR equal to 20. All figures have the same gray scale. (a) Reconstruction by solution of linear equation system. (b) Trapezoidal integration along cartesian grid lines. Average of vertical and horizontal integration. (c) Trapezoidal integration along equipotential lines. 10 equipotential lines per pixel. (d) Reconstruction with equipotential – projection algorithm. 10 equipotential lines per pixel. (e) J-substitution algorithm with large electrodes. Iteration 20. (f) B_z algorithm. Iteration 6.

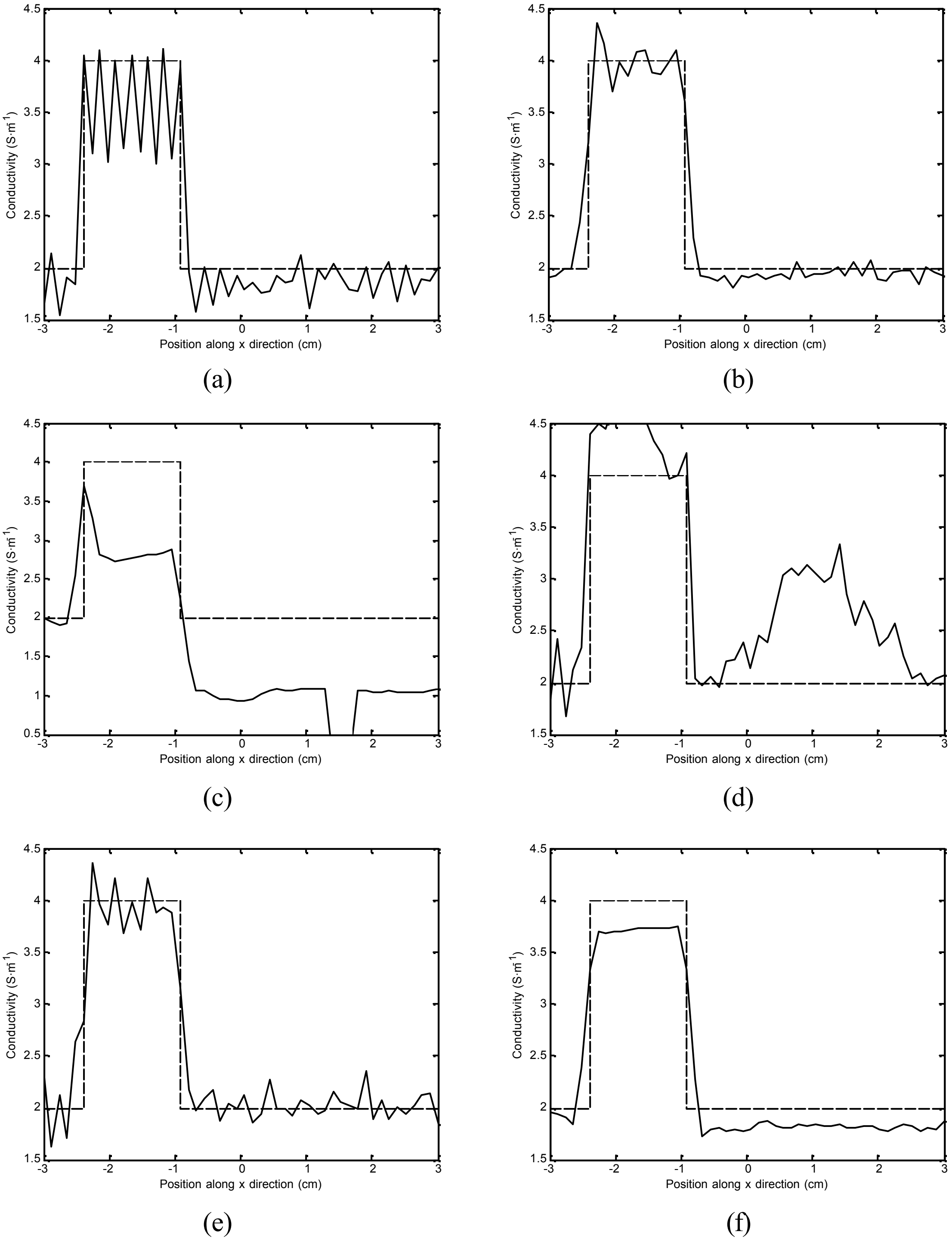

(a)

(b)

(c)

(d)

(e)

(f)

Figure 5.27: Profile images for SNR equal to 20. (a) Reconstruction by solution of linear equation system. (b) Trapezoidal integration along cartesian grid lines. Average of vertical and horizontal integration. (c) Trapezoidal integration along equipotential lines. 10 equipotential lines per pixel. (d) Reconstruction with equipotential – projection algorithm. 10 equipotential lines per pixel. (e) J-substitution algorithm with large electrodes. Iteration 20. (f) B_z algorithm. Iteration 6.

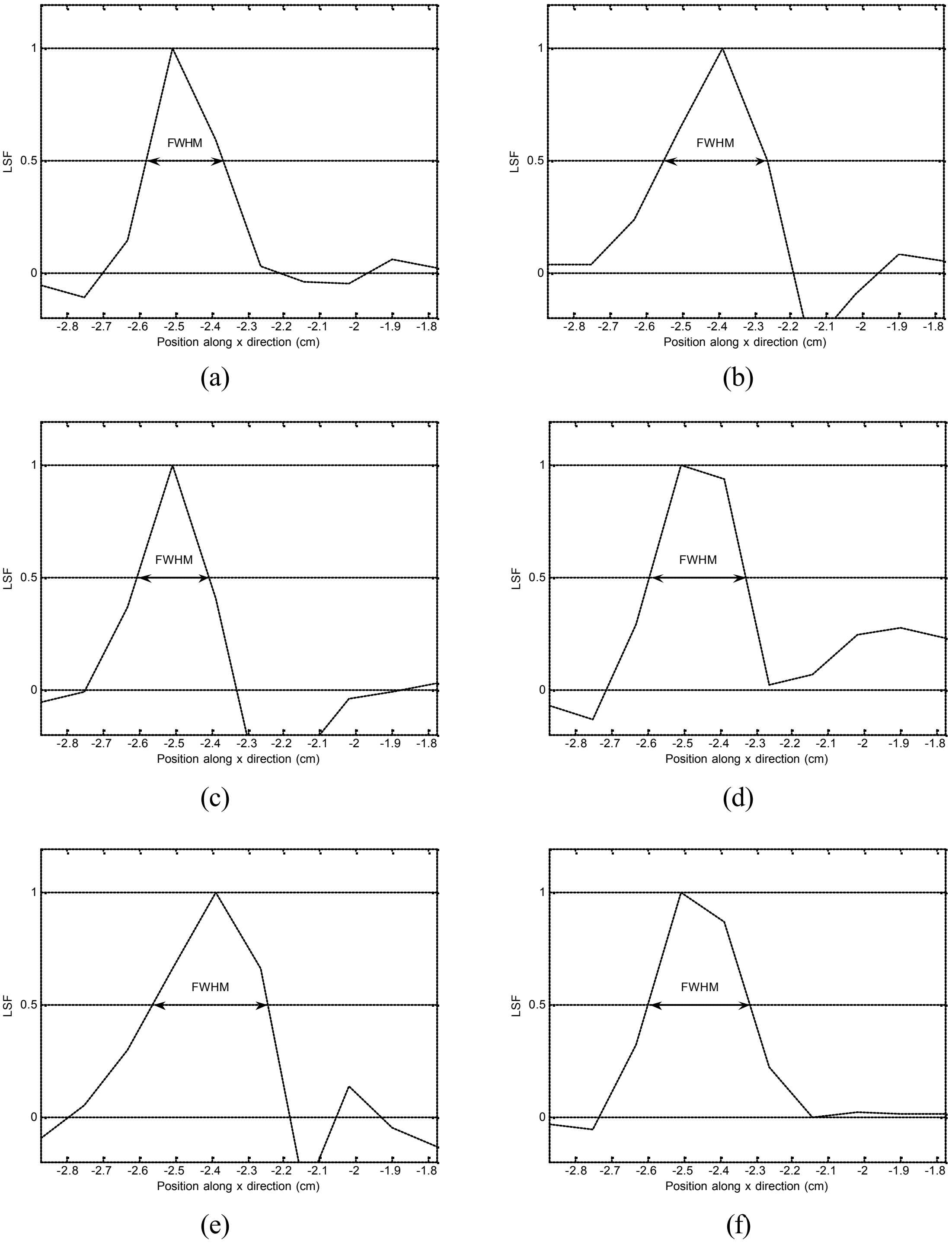

(a)

(b)

(c)

(d)

(e)

(f)

Figure 5.28: LSF images for SNR equal to 20. (a) Reconstruction by solution of linear equation system. (b) Trapezoidal integration along cartesian grid lines. Average of vertical and horizontal integration. (c) Trapezoidal integration along equipotential lines. 10 equipotential lines per pixel. (d) Reconstruction with equipotential – projection algorithm. 10 equipotential lines per pixel. (e) J-substitution algorithm with large electrodes. Iteration 20. (f) B_z algorithm. Iteration 6.

5.9.2 Experimental data

In this section, the reconstruction algorithms are fed with the real data measured by [24] and [2], using the experimental phantom defined in 5.2.2 into the 0.15 Tesla METU-EE MRI system. The reconstructed images can be seen in Figure 5.30. The errors committed in the reconstruction are given in Table 5.17.

Only measured current density distribution corresponding to the horizontal injection pattern is available [24]. This is shown in Figure 5.29(a) and (b). A great amount of noise present in the data is noticeable. Since the object is symmetric, the current density distribution for the vertical injection pattern is obtained by transposition of the measured data corresponding to the horizontal injection case.

The calculation of the equipotential lines using the procedure described in 3.2.1.1 provides extremely few valid equipotential lines. For example, for the vertical injection case, the equipotential lines are started from the left edge, and they travel orthogonal to the current streams at every pixel, until they reach the right edge. But, the amount of current decreases dramatically at the right and left sides, since the electrodes are very small and the conductor has a large conductivity. Due to this reason, these regions are very sensitive to noise. Consequently, the current vectors at the sides are very random and very few equipotential lines can arrive to the conductor at the center and reach the right edge of the image. This situation can be observed in Figure 5.31. As a result, under such noisy conditions, conductivity images can not be reconstructed well by equipotential line based algorithms.

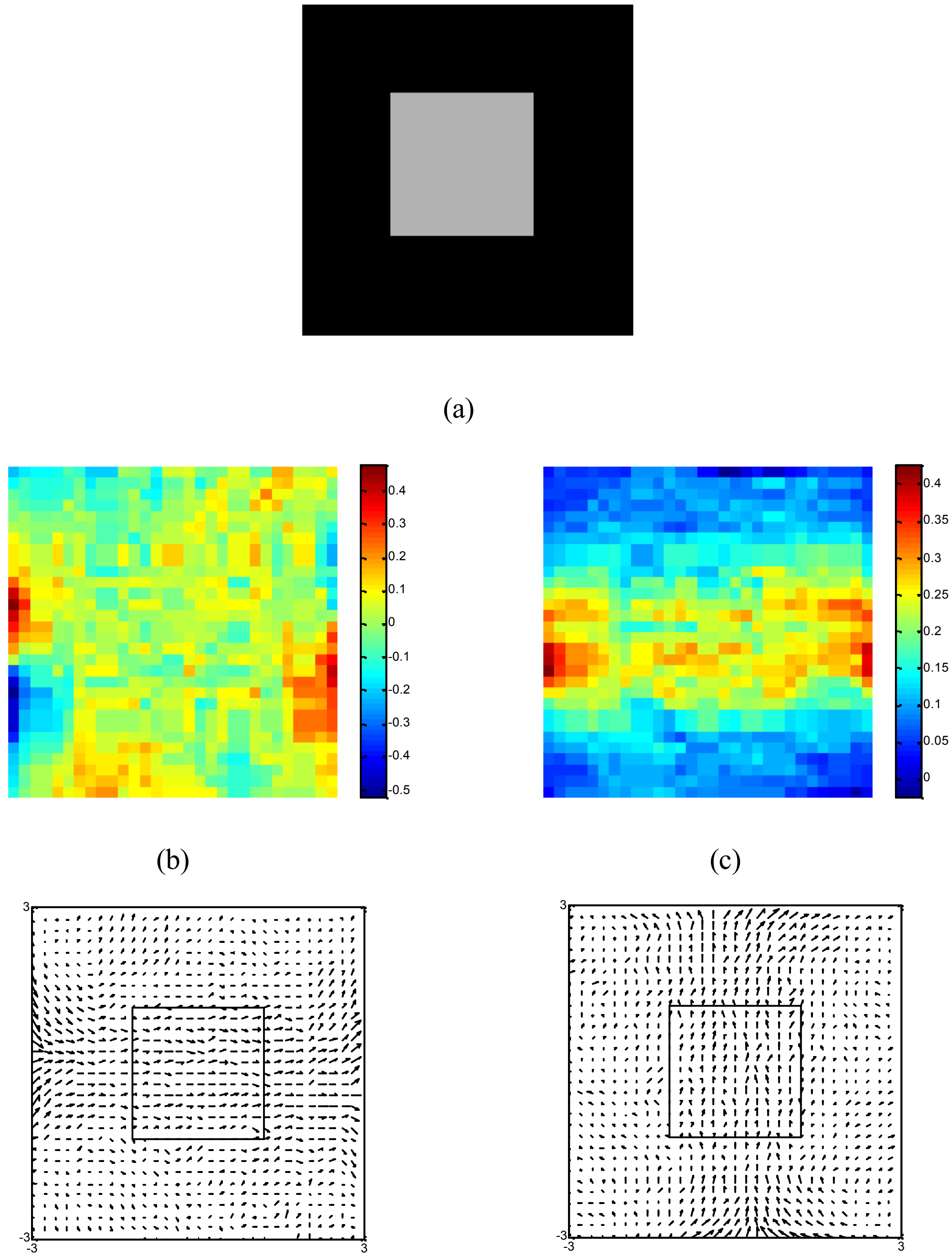
(a)

(b)

(c)

(d)

(e)

Figure 5.29: Measured current density distributions for the experimental data. (a) True conductivity distribution. (b) J_y for the horizontal injection case. (c) J_x for the horizontal injection case. (d) Current density distribution for the horizontal injection pattern. (e) Current density distribution for the vertical injection pattern.

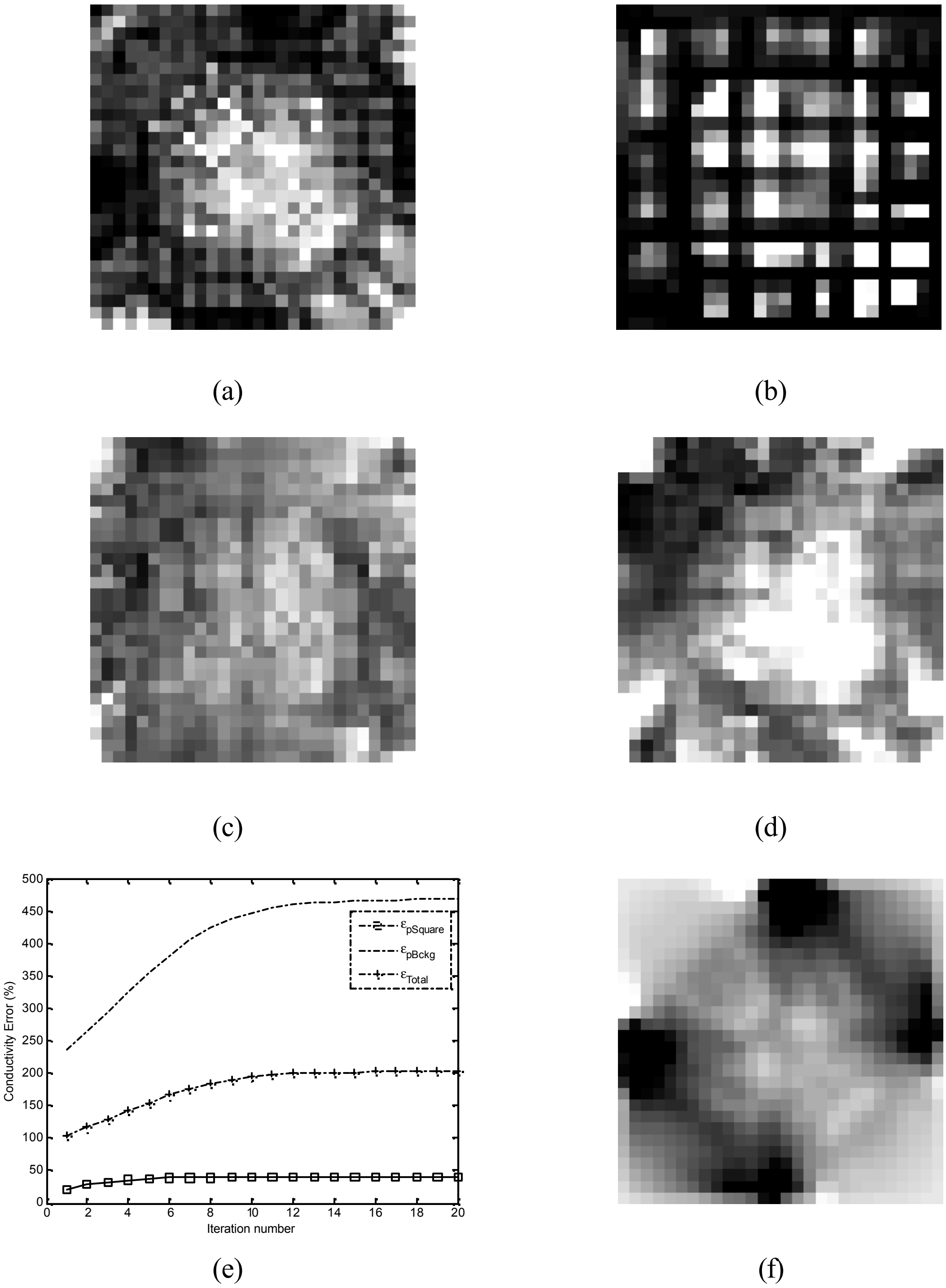

Figure 5.30: Comparison for experimental data. All figures have the same gray scale. (a) Reconstruction by solution of linear equation system. (b) Reconstruction by integration along Cartesian grid lines, averaging between vertical and horizontal integration. Reconstruction conductivity with J-substitution algorithm at iteration 1 (c) and iteration 20 (d). (e) Convergence characteristic of J-substitution algorithm. (f) B_z algorithm. Iteration 6.

Table 5.17: Comparison for experimental data

Reconstruction Algorithms	Rectangle ($e_{s\,Rect}$) (%)	Background ($e_{s\,Bkcg}$) (%)	Total error (%)
Solution of Linear Equation System	32.53	209.24	93.94
Integration Along Cartesian Grid Lines	107.07	2432	1059.2
J-substitution. Iteration 1	21.52	236.42	102.53
J-substitution. Iteration 20	39.56	468.57	202.68
Harmonic B_z. Iteration 6	47.06	310.84	121.24

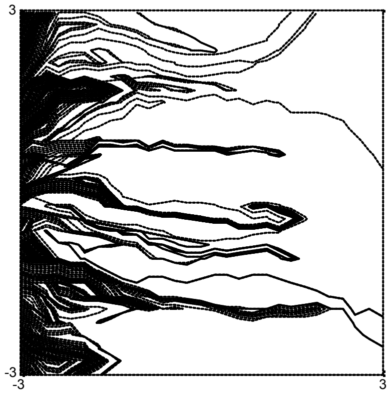

Figure 5.31: Equipotential lines for experimental data. 10 equipotential lines start from each pixel at the left side.

The rest of reconstruction algorithms can deal with this experimental data, although the resulting images have very important errors, especially in the background, due to the noise and small amount of current outside the conductor. The J-substitution algorithm provides the smallest error for the rectangle, while the reconstruction by solution of linear equation system gives the smallest total error and best appearance. The rectangle, in this case, can be more clearly inferred. The Harmonic B_z yields an intermediate solution. The reconstruction by integration along Cartesian grid lines suffers from accumulation of error due to the usage of integration, resulting in huge errors.

CHAPTER 6

CONCLUSIONS AND FUTURE WORK

6.1 Conclusions

In this study, a set of different reconstruction algorithms for MR-EIT, proposed by several research groups have been implemented and their reconstruction accuracies have been compared.

The MR-EIT reconstruction algorithms are classified into two groups: *Type*-I and *Type*-II, depending on the input data they require to reconstruct conductivity images. *Type*-I algorithms use current density distribution, calculated from magnetic flux density data. *Type*-II algorithms, on the other hand, use directly the magnetic flux density data. Both types use peripheral voltage measurements for the reconstruction of the true conductivity values.

Five *Type*-I algorithms, previously proposed, are studied in this thesis. They are the followings: reconstruction by integration along equipotential lines, reconstruction by integration along Cartesian grid lines, reconstruction by solution of a linear equation system by finite differences discretization, reconstruction with equipotential – projection algorithm without potential measurement, and J-substitution algorithm..

Currently, each study uses a different conductivity and noise model, injection profiles, injected current, noise levels, etc. Therefore, in order to compare them objectively, a set of conditions have been defined, so that all of them have been implemented and tested under the same circumstances. Moreover, the output images have been compared directly, without performing any image processing. Reconstruction errors and spatial resolution have been quantified and compared.

In the noise-free case, the iterative algorithms: J-substitution and harmonic B_z algorithm provide the lowest total error, 5.05% and 5.37%, respectively. For the reconstruction along equipotential lines and equipotential – projection algorithm, by using a single injection pattern, the equipotential lines can be traced throughout the image, being orthogonal at every pixel to the current vector. But, these equipotential lines may not cover the whole image, due to conductivity changes inside the phantom. Those non-covered areas remain with unknown conductivity, generating discontinuities and, indirectly, errors in the reconstruction. Thus, the equipotential – projection algorithm gives the highest total error, 16.05%, while the reconstruction along equipotential lines yields 11.36%. These figures may be reduced by obtaining the equipotential lines for two orthogonal injection patterns and combining adequately the resulting images. The integration along Cartesian grid lines and solution of a linear equation system algorithms yield to similar intermediate errors: 6.44% and 8.67%, respectively, although the latter one provides sharper contours. The methods which provide less blur images are the solution of a linear equation system and equipotential – projection algorithm. The methods which involve integrations give the most blurred images. Finally, both iterative algorithms produce intermediate blurring results.

In order to study the performance of the reconstruction algorithms in presence of noise, different noisy current densities, corresponding to SNR noise levels equal to 60, 30 and 20 are generated. When the SNR is smaller than 20, equipotential lines cannot be traced, so the integration along equipotential lines and equipotential – projection algorithms are very affected. In the latter one, few pixels accumulate exaggerated values in the background, although the rest of conductivity regions in the image have similar error values to the rest of algorithms. As it was previously said, this effect may be reduced by using two orthogonal injection patterns. The J-substitution algorithm, as in the noise-free case, gives the lowest overall error, although it may diverge if the noise level is below SNR equal 20, or if the electrode sizes become too small. The linear equation system algorithm, however, is very robust against noise. It can reconstruct with a noise level of SNR equal to 5 with a total error of 50%. Moreover, it presents the sharpest reconstructed images, as in the noise-free case. In the case of integration along Cartesian grid lines, although the overall errors are not especially high, the resulting images become very blurred, since the integration techniques tend to spread the errors along the direction of integration. Finally, the harmonic B_z algorithm provides acceptable images, but with intermediate reconstruction errors.

6.2 Future work

In this thesis, a set of different reconstruction algorithms have been implemented and compared. Some of the possible further work can be:

- Validate the simulated results with more measured data.
- Define and set up a complete test bed, in order to be able to compare rapidly and in an automatic way very different aspects of the incoming and previously proposed algorithms: spatial resolution, different injection profiles, size of electrodes, object placements, noise levels, etc.
- Apart from comparing the reconstructed images objectively, other perceptual methods could be used, additionally.

REFERENCES

[1] D. C. Barber and B. H. Brown, “Applied Potential Tomography (Review Article)”, *J. Phys. E. Sci.Instrum*, vol. 17, pp. 723 – 733, 1984.

[2] Ö. Birgül, “Development of reconstruction algorithms for magnetic resonance-electrical impedance tomography and experimental realization”, PhD thesis, Middle East Technical University, Ankara, Turkey, Dept. of EE, 2002.

[3] Ö. Birgül, B. M. Eyüboglu and Y. Z. Ider, “Current constrained voltage scaled reconstruction (CCVSR) algorithm for MR-EIT and its performance with different probing current patterns”, *Phys. Med. Biol.*, vol. 48, pp. 653-71, 2003.

[4] K. Boone, D. Barber, and B. Brown, “Imaging with electricity: Report of the European concerted action on impedance tomography”, *Journal of Medical Engineering and Technology*, vol. 21, no. 6, pp. 201-232, 1997.

[5] D. K. Cheng, “Field and Wave Electromagnetics”, Addison-Wesley Publishing Company, 1983.

[6] B. M. Eyüboglu, “Development an Application of Electrical Impedance Tomography for Thoracic Imaging”, PhD thesis, University of Sheffield, Dept. of Medical Physics and Clinical Engineering, Sheffield, UK, 1988.

[7] B. M. Eyüboglu, A. Köksal, and B. M. Demirbilek, “Distinguishability analysis of an induced current EIT system using discrete coils”, *Phys. Med. Biol.*, vol. 45, pp. 1997-2009, 2000.

[8] B. M. Eyüboglu, R. Reddy, and J. S. Leigh, ‘‘Magnetic Resonance – Electrical Impedance Tomography”, Patent No: U. S. 6,397,095 B1, Issued on: May 28, 2002.

[9] T. J. C. Faes, H. A. van der Meij, J. C. de Munck, and R. M. Heethaar, “The electric resistivity of human tissues (100 Hz-10 MHz): a meta-analysis of reviews studies”, *Physiol. Meas.*, vol. 20, pp. R1-R10, 1999.

[10] G. Folland, “Introduction to Partial Differential Equations”, Princeton, NJ: Princeton University Press, 1976.

[11] I. L. Freeston and R. C. Tozer, “Impedance imaging using induced currents”, Physiol. Meas., vol. 16, pp. A257-66, 1995.

[12] N. G. Gençer, Y. Z. Ider, and S. J. Williamson, “Electrical impedance tomography: Induced-current imaging achieved with a multiple coil system”, *IEEE Trans. Biomed. Eng.*, vol. 43, pp. 139-49, 1997.

[13] D. Gilbarg, and N. S. Trudinger, “Elliptic Partial Differential Equations of Second Order”. Berlin, Germany: Springer-Verlag, 1983.

[14] R. P. Henderson and J. G. Webster, “An impedance camera for spatially specific measurements of the thorax”, *IEEE Trans. Biomed. Eng.*, vol. 25, pp. 250-254, 1978.

[15] Y. Z. Ider, S. Onart, and W. R. B. Lionheart, “Uniqueness and reconstruction in magnetic resonance-electrical impedance tomography (MR-EIT)”, *Physiol. Meas.*, vol. 24, pp. 591-604, 2003.

[16] H. Kang, and J. K. Seo, “The layer potential technique for the inverse conductivity problem”, *Inverse Problems*, vol. 12, pp. 267-278, 1996.

[17] S. W. Kim, O. Kwon, J. K. Seo, and J. R. Yoon, “On a nonlinear partial differential equation arising in magnetic resonance electrical impedance tomography”, *SIAM J. Math. Anal.*, vol. 34, pp. 511-26, 2002.

[18] A. Köksal and B. M. Eyüboglu, “Determination of optimum injected current patterns in electrical impedance tomography”, *Clin. Phys. Physiol. Meas.*, vol. 16, suppl. A, pp. 99-109, 1995.

[19] D. Y. Kwak, “V-cycle multigrid for cell-centered finite differences,” *SIAM J. Sci. Comput.*, vol. 21, pp. 552–564, 1999.

[20] O. Kwon, E. J. Woo, J. R. Yoon, and J. K. Seo, “Magnetic resonance electrical impedance tomography (MREIT): simulation study of J-substitution algorithm”, *IEEE Trans. Biomed. Eng.*, vol. 49, pp. 160-7, 2002.

[21] A. A. Maudsley, H. E. Simon, and S. K. Hilal, “Magnetic field measurement by NMR imaging”, *J. Phys. E: Sci. Instrum.*, vol. 17, pp. 216-220, 1984.

[22] S. H. Oh, B. I. Lee, E. J. Woo, S. Y. Lee, M. H. Cho, O. Kwon, and J. K. Seo, “Conductivity and current density image reconstruction using harmonic B_z algorithm in magnetic resonance electrical impedance tomography”, *Phys. Med. Biol.*, vol. 48, pp. 3101-16, 2003.

[23] S. Onart, “Development of Image Reconstruction Algorithms for three dimensional Magnetic Resonance – Electrical Impedance Tomography”, Master’s thesis, Bilkent University, Ankara, Turkey, Dept. of EE, 2003.

[24] O. Özbek, “Imaging current density distribution using 0.15T magnetic resonance tomography”, Master’s thesis, Middle East Technical University, Ankara, Turkey, Dept. of EE, 2002.

[25] M. S. Özdemir, “Equipotential projection based magnetic resonance electrical impedance tomography (MR-EIT) for high resolution conductivity imaging”, Master’s thesis, Middle East Technical University, Ankara, Turkey, Dept. of EE, 2003.

[26] B. Rigaud and J. P. Morucci, “Bioelectrical impedance techniques in medicine: Part II. Impedance imaging, general concepts and hardware”, *Crit. Rev. Biomed. Eng.*, vol. 24, pp. 467-588, 1996.

[27] G. C. Scott, M. L. G. Joy, R. L. Armstrong, and R. M. Henkelman, “Measurement of non-uniform current density by magnetic resonance”, *IEEE Trans. Med. Imaging*, vol. 10, pp. 362-74, 1991.

[28] G. C. Scott, M. L. G. Joy, R. L. Armstrong, and R. M. Henkelman, “Sensitivity of magnetic resonance current-density imaging”, *J. of Magnetic Resonance*, vol. 97, pp. 235-254, 1992.

[29] A. D. Seagar, D. C. Barber, and B. H. Brown, “Theoretical limits to sensitivity and resolution in impedance tomography”, *Clin. Phys. Physiol. Meas.*, vol. 8, suppl. A, pp. 13-31, 1987.

[30] J. K. Seo, J. R. Yoon, E. J. Woo, and O. Kwon, “Reconstruction of conductivity and current density images using only one component of

magnetic field measurements", *IEEE Trans. Biomed. Eng.*, vol. 50, pp. 1121-4, 2003.

[31] S. W. Smith, "The Scientist and Engineer's Guide to Digital Signal Processing", California Technical Publishing, 1997. Online: http://www.dspguide.com/

[32] M. E. Valentinuzzi, "Biomedical impedance techniques in medicine, part I: Bioimpedance measurement", *Critical Reviews in Biomedical Engineering*, vol. 24, no. 4-6, pp. 223-255, 1996.

[33] Wikipedia, "Finite Difference", http://en.wikipedia.org/wiki/Finite_differences, 22.01.2007.

[34] Wikipedia, "Trapezoidal rule", http://en.wikipedia.org/wiki/Trapezoidal_rule, 23.01.2007.

[35] N. Zhang, "Electrical impedance tomography based on current density imaging", Master's thesis, University of Toronto, Dept. of Electrical and Electronics Eng. Toronto, Canada, 1992.

APPENDIX A

SIMULATION OF MEASUREMENT NOISE

In order to understand the behavior of the algorithms in presence of measurement noise, simulated measurement noise is added to the current density data.

In real experiments, the current density data, $\vec{J}_{MR}$ is, in fact, calculated from the magnetic flux density measurements $\vec{B}_{MR}$. Therefore, the simulated additive noise should be firstly included into the $\vec{B}_{MR}$ terms and, from there, the noisy current density obtained.

Scott *et al* [28] in 1992 performed a very detailed experimental study regarding the noise in MRI phase images, providing means of achieving a desired sensitivity.

Scott *et al* state that the resistance of the RF receiver coil and magnetic losses caused by the sample conductivity are the dominant sources of noise in a well-tuned MRI system. They create a wide-band additive Gaussian white noise at the receiver that generates a zero-mean-independent-identically-distributed Gaussian noise, $n_c + jn_s$ in each image pixel. The complex standard deviation is defined as $s = \sqrt{\langle n_c^2 \rangle + \langle n_s^2 \rangle}$. It is measured as the *rms* noise in the magnitude image background. In their work, the signal to noise ratio (SNR_{MR}) is defined as:

$$SNR_{MR} = \frac{A}{s} = \Psi_s \, \Delta x \, \Delta y \Delta z \sqrt{N \cdot T_S} M(x, y), \tag{A.1}$$

where A is the magnitude of the noise-free pixel value of the corresponding MR image, Ψ_s is a system SNR, $\Delta x \Delta y \Delta z$ is the voxel volume, N is the total number of excitations (averages times phase encodes), T_S is the readout sampling time for one echo, and $M(x,y)$ is the magnetization.

The phase error probability density function is given by:

$$f_\Phi(f) = \frac{1}{2}\exp\left(\frac{-a^2}{2}\right) + \frac{a\cos(f)}{2\sqrt{2p}}\exp\left(\frac{-a^2\sin^2(f)}{2}\right) erfc\left(\frac{-a\cos(f)}{\sqrt{2}}\right), \quad \text{(A.2)}$$

where $a = \sqrt{2}SNR$, and Φ represents the phase error.

Now, the random noise must be generated with this probability density function. Afterwards, the noise magnetic flux density is obtained from the noisy phase and, finally, the noisy current density can be calculated from the corresponding noisy magnetic flux density.

A.1. Generation of random noise with a given Probability Density Function

In order to generate numerically the random noise with the probability density function $f_\Phi(f)$ described in Equation (A.2), the range of possible values for MR phases f is divided into N bins [1]. In the implementation of this algorithm, f goes from $-p$ to p, while the number of bins is 720. Firstly, a very large sequence of L samples (e.g. from 1 to 10^6 in this study) is uniformly placed into the bins. The number of samples contained in each bin is proportional to the probability density function at the center point of the corresponding bin interval. Then, if M noise values are needed, for each of them the following independent experiment is done. Firstly, a random number between 1 and L is generated. Then, the bin where this number is contained is searched. Finally, the noisy f value is assigned as the phase value of that bin.

A.2. Obtaining the noisy magnetic flux density distribution

The noise to be added to the magnetic flux density distribution can be extracted from the phase noises f calculated above, remembering the Equation (2.50):

$$B_{n,z}(x,y)=\frac{f(x,y)}{gT_C}. \tag{A.3}$$

Repeating three times the experiment described in the previous section independently, noise for the three components of $\vec{B}_{MR}$ can be obtained. This noise is denoted by $\vec{B}_n$. Then, the noisy $\vec{B}_{nMR}$ can be calculated by adding the noise $\vec{B}_n$ to the noise-free values of $\vec{B}_{MR}$ distribution.

But, in this thesis, the FEM solver provides directly current density data and not magnetic flux density. Therefore, the noise-free $\vec{B}_{MR}$ must be calculated from the noise-free current density data $\vec{J}_{MR}$. As explained in Section 2.2.4, the relation between both of them is given by Biot-Savart law. This can be numerically discretized as:

$$\begin{bmatrix} \mathbf{b}_x \\ \hline \mathbf{b}_y \\ \hline \mathbf{b}_z \end{bmatrix} = \begin{bmatrix} \mathbf{0} & \mathbf{D_z} \\ \hline -\mathbf{D_z} & \mathbf{0} \\ \hline \mathbf{D_y} & -\mathbf{D_x} \end{bmatrix} \begin{bmatrix} \mathbf{j}_x \\ \hline \mathbf{j}_y \end{bmatrix}, \tag{A.4}$$

where $\mathbf{j}_x$ and $\mathbf{j}_y$ are the column vectors of J_x, J_y values for the elements in the subject, respectively, and $\mathbf{b}_x$, $\mathbf{b}_y$ and $\mathbf{b}_z$ are the column vectors of B_x, B_y and B_z at the field points, respectively. The Equation (A.4) can be expressed in close form as:

$$\overline{\mathbf{B}} = \overline{\overline{\mathbf{D}}}\cdot\overline{\mathbf{J}} \tag{A.5}$$

Let an additional plane be placed at $z=5$ mm above the slice to be imaged. Using the Biot-Savart law, each element of $\vec{J}_{MR}$ is generating a magnetic flux density $\vec{B}_{MR}$ at $z=5$ mm. Then, the matrices $\mathbf{D_x}$, $\mathbf{D_y}$ and $\mathbf{D_z}$ in (A.4) only depend on the distance between the elements on the slice and the ones on the additional plane, and the direction of the vector which connects them.

Consequently, the noise-free $\vec{B}_{MR}$ values can be obtained from the noise-free $\vec{J}_{MR}$ solving the Equation (A.5).

Now, the noisy magnetic flux density $\vec{B}_{n,MR}$ can be calculated by adding the noise $\vec{B}_n$ values to the noise-free $\vec{B}_{MR}$ distribution as follows:

$$\vec{B}_{n,MR} = \vec{B}_{MR} + \vec{B}_n \tag{A.6}$$

A.3. Obtaining the noisy current density distribution

Finally, once the noisy $\vec{B}_{n,MR}$ has been calculated, the noise current density, $\vec{J}_{n,MR}$, can be obtained using the inverse of $\overline{\overline{\mathbf{D}}}$ matrix, as follows:

$$\overline{\mathbf{J}}_{\mathbf{n,MR}} = \overline{\overline{\mathbf{D}}}^{-1} \cdot \overline{\mathbf{B}}_{\mathbf{n,MR}} \tag{A.7}$$

It is noticeable that, in the noise model of Scott *et al*, the phase error and the noise in $\vec{B}_{n,MR}$ is independent of the noise-free $\vec{B}_{MR}$ values. This means that, for an increased amount of current density, since $\vec{B}_{MR}$ is also increased, the proportional noise in the $\vec{B}_{n,MR}$ values is reduced. Similarly, in such a case, the proportional noise in $\vec{J}_{n,MR}$ is also reduced.

Consequently, this model permits the comparison of different current injection strategies under the same noise conditions. This provides a more realistic and experimentally verified noise probability density function into the simulations, as opposed to, for example, making the noise just proportional to the current magnitude of $\vec{J}_{MR}$.